COLCINS



A Metamorphic, Geochronological and Structural framework for the evolution of the Leeuwin Complex, south west Western Australia

Rupert Verco

Supervisors: Martin Hand & Alan Collins

Continental Evolution Research Group

Department of Geology and Geophysics

School of Earth and Environmental Sciences

University of Adelaide, South Australia

Submitted 24th October 2008

Contents

1 Abstract

The Leeuwin Complex of southwestern Western Australia forms the best exposed component of the Pinjarra Orogen, where early Cambrian deformation and metamorphism represents one of the final events in Gondwana amalgamation. Three structurally different domains within the Leeuwin Complex are identified and a structural model for pure shear (coaxial strain) is preferred for the subhorizontal structures of the central structural domain. This is based on the identification of four phases of progressive deformation within the central structural domain that are interpreted to have occurred during or after peak metamorphism. Subvertical compression accounts for D1 and D2 deformation and D3 represents a transition from subvertical compression to pure shear east-west shortening. D4 structures are interpreted as post peak metamorphism east-west extension.

U-Pb SHRIMP and LA-ICPMS analysis of zircon and monazite constrain peak metamorphism to *c* 522 Ma. Thermobarometric calculations for peak metamorphic mineral assemblages yield average *P-T* estimations of 7.24 ± 0.61 kbar and 687 ± 28°C for the Leeuwin Complex. *P-T* calculations based on mineral rim compositions reflect retrograde conditions ~0.5 – 1 kbar less and ~50 - 100°C cooler than peak metamorphic conditions, implying that the Leeuwin Complex remained at mid-crustal levels after peak metamorphism. Analysis of chemical zoning in garnet suggests that after a prolonged period at mid-crustal depths, the Leeuwin Complex was exhumed rapidly.

Sm – Nd isotopic data are presented for selected samples that reflect the two apparent protoliths of the felsic orthogneisses. εNd values are comparable to Sm – Nd isotope data from eastern Antarctica. Evolved εNd are interpreted to indicate that the petrogenesis of the Leeuwin Complex protoliths involved partial melting of an enriched crustal source, which is interpreted to be the Mesoproterozoic Naturaliste Plateau which is considered a western continuation of the Albany-Fraser crust.

Keywords: early Cambrian, geochronology, Gondwana, Leeuwin Complex, structure, thermobarometry

2 Introduction

The Leeuwin Complex of southwestern Australia forms one of three inliers of the Pinjarra Orogen (Myers, 1990; Wilde & Murphy, 1990; Wilde 1999; Janssen *et al.* 2003; Collins, 2003) that are exposed along the margin of Western Australia. The tectonic evolution of the complex is poorly understood, which is surprising due to its importance in previously proposed reconstructions of Neoproterozoic to Early Cambrian Gondwana (i.e. Harris & Beeson, 1993; Wilde, 1999; Fitzsimons, 2003). The complex is composed of orthogneisses that are thought to have formed in a chemically differentiated suite within a Mesoproterozoic ensialic rift environment (Wilde & Murphy, 1990; Wilde, 1999). Geochemical and isotopic data from the southern Leeuwin Complex presented by Wilde & Murphy (1990) and Wilde (1999) suggest high temperature, intra-continental melting of a tonalite/ granodiorite source as the likely protolith of the A-type granotoids of the Leeuwin Complex. However, geochronological data (Nelson 1996; 1999; 2002; Collins, 2003 & this study) indicate that the protolith of the Leeuwin Complex did not form from a single contemporaneous suite, but episodic magmatic intrusions that occurred over *c* 600 Ma (Collins, 2003). Recent SHRIMP U-Pb dating has constrained peak metamorphism at ~*ca.* 522Ma in the northern Leeuwin Complex (Collins, 2003), which has significant ramifications to previous theories on the timing and processes of amalgamation of Palaeozoic Gondwana. Early reconstructions of Neoproterozoic Gondwana suggest that Late Neoproterozoic – Early Cambrian deformation within the Pinjarra Orogen was attributed to intercontinental shear zone deformation within a combined East Gondwana Plate (Harris, 1994). However, palaeomagnetic data is interpreted to show that Australia and India were separated by over 30° of latitude at *c* 810 Ma (Torsvillk *et al.* 2001; Pisarevsky *et al.* 2003; Collins, 2003), but were neighbouring one another by 522 ± 13 Ma in Gondwana (Powell *et al.* 1993). Geochronological data constraining the timing of metamorphism within in the Leeuwin Complex to *ca* 522 ± 5 Ma (Collins, 2003) indicate that collision between Australia and India is likely to have occurred in the Early Cambrian (Fitzsimons, 2003; Janssen *et al.* 2003; Collins, 2003). This is some 100 Ma later than previously suggested (Pisarevsky, 2002).

Metamorphic rocks within the Leeuwin Complex preserve upper amphibolite – granulite assemblages. Wilde & Murphy (1990) obtained temperatures of ~690°C based

on two-pyroxene geothermometry from samples derived from Cape Naturaliste in the northern Leeuwin Complex. These calculations were based on the assumption that metamorphism took place at low pressure, although the presence of garnet within mafic lithologies at numerous locations (Janssen *et al.* 2003; this study) implies that at least moderate pressures were experienced during metamorphism. Different views have been expressed as to whether the whole complex experienced granulite facies metamorphism and was partially retrogressed to amphibolite facies during the *ca* 540 Ma disturbance event (Myers, 1994), or whether the preserved metamorphism reflect the near peak assemblages of one metamorphic event with higher grades exhumed in the north of the complex (Wilde & Murphy, 1990). The latter was dismissed by Collins (2003), who deemed the geochronological evidence for peak metamorphism at *ca* 615 Ma (Nelson, 1996) inconclusive, and argued that the 550-500 Ma episode of magmatism was not disturbance events as previously suggested. Rather Collins (2003) was suggestive that this metamorphism was the peak event, which is geochronologically well constrained to 522 ± 5 Ma using U-Pb, SHRIMP (Special high resolution ion microprobe) age dating of metamorphic zircons (Collins, 2003) in the northern Leeuwin Complex. Placing age constraints on metamorphic events and determining the associated structural characteristics of the Leeuwin Complex provide an important piece in determining the breakup of the super continent Rodinia and the amalgamation of Gondwana (Figure 1).

Despite the various views that have been expressed about the timing of metamorphism, and the significance of the Leeuwin Complex in tectonic reconstructions of Late Neoproterozic – Early Cambrian Gondwana, there has been surprisingly little work done to understand the physical conditions of metamorphism within the Leeuwin Complex.

This paper presents average P-T calculations from a range of samples that span the entity of the outcropping Leeuwin Complex, using the internally consistent THERMOCALC 3.21 software of Holland and Powell (1988). *P-T* calculations are based on core mineral assemblages that are likely to reflect peak metamorphism, and rim analysis have been undertaken in order to determine retrograde conditions. The calculations indicate high temperature and moderate pressure granulite facies conditions throughout the Leeuwin Complex. Temporal constraints on peak metamorphism are constrained by geochronological analyses of metamorphic zircon

using SHRIMP II (sensitive-high resolution ion microprobe) and monazite analyses using LA-ICPMS (laser ablation – inductively coupled mass spectrometry). Whole rock Nd-Sm isotopic data is presented and compared to other regions in the Gondwana amalgamation to better understand the regional correlations involving the Leeuwin Complex. In association with structural data, the timing and conditions of metamorphism are discussed with respect to previously published data.

3 Geological Setting

The Mesoproterozoic – Early Cambrian Leeuwin Complex lies 200km southwest of Perth as a narrow coastal ridge that extends for 96km between Cape Naturaliste in the north and Cape Leeuwin in the south (Peers, 1975, Figure 2). The complex is dominated by felsic gneiss derived from granitic protoliths. Outcrop of the orthogneisses are limited to the coastline and river beds as the majority of the complex is overlain by sand, Tertiary laterite, Quaternary Tamala Limestone and also obscured by the heavy vegetation of the Boranup Forest. To the west, the Leeuwin Complex is separated from the submarine Naturaliste Plateau by the Mentelle Basin (Halpin *et al.* 2008). To the east the complex is bound to the Dunsborough Fault (Figure 2) which separates the complex from the Phanerozoic Perth Basin. There is no geochronological evidence that associates the Leeuwin Complex with the Archaean Yilgarn Craton that lies some 50km to the east.

Geochronological data from Wilde & Murphy (1990), Nelson (1996; 1997; 1999; 2002) and Collins (2003) has revealed a complex magmatic history. Precursors of the granite gneiss at Redgate Beach were emplaced at ~1180-1090 Ma (Nelson, 1999). Significant differences in trace element composition between the orthogneiss protoliths of Redgate Beach and the *ca* 750 Ma protoliths of Sugarloaf (Collins, 2003) and Cosy Corner (Nelson, 1996) reflect two completely different tectonic environments. Collins and Fitzsimons (2001), Fitzsimons (2003) and Janssen *et al.* (2003) established that the 1090 Ma protolith has trace-element compositions consistent with a syncollisional origin, whereas the younger protoliths have trace-element compositions that reflect anorogenic, A-type magmatism, generated by intracrustal melting in a rift environment (Wilde, 1999). Based on the available age data it is likely that this magmatism was

associated with the breakup of the super continent Rodinia. Emplacement of the 1090 Ma protoliths was suggested to be spatially and genetically related to the 1080 Ma metamorphism within the (Northampton and Mullingarra Complexes) Pinjarra Orogen, to the north of the Leeuwin Complex (Figure 1) (Fitzsimons, 2003), where burial of sediments reached depths of ~ 20km (Janssen *et al.* 2003). Recent geochronological evidence from dredge samples from the submarine Naturaliste Plateau (Haplin et al. 2008) reveals Mesoproterozoic plutonic ages of 1230 to 1190 Ma. This data suggests that the Naturaliste Plateau protoliths are not genetically related to the Leeuwin Complex prior to the emplacement of the 1180 – 1090 Ma protoliths of Redgate Beach. However, limited exposure of the Leeuwin Complex may conceal older, Mesoproterozoic age rocks.

Wilde & Murphy (1990) suggested that the termination of mobile belt activity and a change from a compressional to an extensional regime occurred by *c* 570 Ma. This reasoning was largely based on questionable U-Pb zircon data that yielded ages from 550 – 570 Ma which was interpreted to date the igneous emplacement of anorogenic, A-type granitoids. Harris (1994) proposed that the emplacement of alkali granites, anorthosite and mafic intrusives of the Leeuwin Complex occurred within a dilational jog along a N- to NNW-striking sinistral shear zone of the Darling mobile belt. This was based upon reported observation of north-south sinistral shear zones from the Leeuwin Complex. However, regional scale mapping by Collins (2003) and this study found no evidence for ductile strike slip deformation. The sinistral component of tectonic transport is considered to be a result of the oblique collision with India which occurred along the Pinjarra Orogen around 550-500 Ma (Janssen *et al.* 2003; Powell & Pisarevsky, 2002; Collins & Pisarevsky, 2005).

The youngest zircon ages of 550-500 Ma were previously interpreted to be disturbance events by Nelson (1996, 1999 & 2002) who argued that peak granulite facies metamorphism occurred at *ca* 615 Ma, and that later events (540-524 Ma) were associated with retrograde amphibolite facies metamorphism. Collins (2003) argued that the *ca* 615 Ma age was far from conclusive. Geochronological evidence presented by Collins (2003) from the Sugarloaf antiform in the northern structural domain of the Leeuwin Complex, and geochronological data from this study constrain peak metamorphism to 530-520 Ma. Metamorphism throughout the Pinjarra Orogen and its

Antarctic counterpart at 550-500 Ma indicate oblique collision between India and Western Australia in the final amalgamation of Gondwana occurred during the Early Cambrian (Fitzsimons, 2003; Collins, 2003; Kelsey *et al.* 2008). This is some 100 Ma later than the time frame (680-610 Ma) suggested by Powell and Pisarevsky (2002).

4 Structure of the Leeuwin Complex

The structural evolution of the Leeuwin Complex is still relatively unknown and due to the limited outcrop of the granitic gneisses, and it is difficult to generate a constructive structural model for the whole complex. From field observations it is apparent that there are three dissimilar structural 'domains' within the Leeuwin Complex (Figure 2). The northern Leeuwin Complex has previously been mapped by Kay (1958), Myers (1994) and Collins (2003). A detailed structural transect along with the deformation history was presented by Collins (2003) who identified four phases of deformation (summarised in Table 1) that produce, upright ~N-S trending structures. Similar episodes of deformation have been identified within the southern domain of the Leeuwin Complex by Myers (1994) and Janssen *et al* (2003) and are summarised in Table 1. The structural features of the southern domain are similar to the northern domain (Myers, 1994; Janssen *et al.* 2003) however, the central domain consists of largely sub-horizontal gneissic structures. Little work has been done within the central Leeuwin Complex to identify the structural relationship between the flat-lying structures of the central domain and the upright folding identified in both the northern and southern domains.

Regional scale mapping of the central Leeuwin Complex has largely been restricted to Myers (1994) who identified three periods of deformation, D1 was interpreted as the original emplacement of the anorogenic, A-type granitoids (referred to as the Cowaramup gneiss). D2 was interpreted as the deformation and high grade metamorphism associated with the intrusion of the Hamelin granite and mafic dykes (interpreted as late Proterozoic). Folding of the foliation (D2) and amphibolite layers is interpreted as a product of D3 deformation, which coincided with granulite facies metamorphism. Myers (1994) interpreted the granite migmatite gneisses of Redgate Beach and Cape Freycinet as highly deformed Hamelin granite that intruded the older

Cowaramup gneiss. Zircon dating by Nelson (2002) has revealed that this part of the central Leeuwin does not contain the crystallisation ages of the northern and southern domains but is formed from a 1090 Ma protolith. Therefore, unless the central Leeuwin Complex contains a much older metamorphic history, the interpretation of Myers (1994) is questionable.

5 Structure of the Central Leeuwin Domain

From field observation, regional and outcrop scale mapping of the central Leeuwin domain, four phases of deformation have been identified and are summarised below. Regional scale maps of selected locations within the central domain (Figure 3) reveal a relatively consistent shallowly dipping E to ESE foliation with a down-dip to slightly oblique (to the NE) mineral elongation lineation. The foliation and lineation vary slightly between each location but are relatively homogeneous over the whole central domain. Isoclinal folds within amphibolites have fold hinges parallel to the mineral lineation. No obvious indicators of the upright, regional scale folding evident within the southern and central domains can be seen within the central domain.

5.1 *D1 structures*

Initial deformation is attributed to crustal compression at mid crustal depths. Evidence preserved within D2 isoclinal folds (Figure 4) reveal preserved traces of a preliminary S1 foliation. The S1 foliation has been folded by D2 deformation, where centimetre-scale folds of the S1 foliation are present within the fold hinge of the D2 folded amphibolite layer. Folding of the S1 foliation is parallel to the fold hinge of the amphibolite layer and likely to be axial planar to the S2 foliation.

5.2 *D2 structures*

The second deformation is considered to be a continuation of D1, as the orientation of D2 structures suggests that D2 strain was coaxial with D1. Deformation is defined by the dominant shallow, east-dipping S2 foliation, and associated down-dip to slightly oblique (NE-SW) mineral elongation lineation that is commonly defined by plagioclase

hornblende and biotite. The temporal and overprinting structural relationship between the S1 and S2 foliation fabrics is presented by the schematic diagram within Figure 4 which demonstrates the formation and preservation of two tectonic fabrics. D2 is responsible for the meter-scale isoclinal folding of amphibolite layers (Figure 4), formed by subhorizontal shortening. Small, 'stringer' like garnet-absent amphibolite layers preserve isoclinal-tight recumbent folding that is axial planar to the S2 foliation and are parallel to the local mineral elongation lineation. Large 10-90mm garnet porphyroblasts are present within the fold hinges of D2 folded amphibolite layers (figure 5).

5.3 *D3 Structures*

Foliation parallel leucosomes exhibit 'kink' fold structures that suggest a compressional regime. Structural data taken from 'kink' folds (Figure 6) reveal conjugate sets of kink folds (Figure 6; c & d) and are interpreted as box folds that reflect the bulk shortening orientation to be WSW-ENE. Diffuse, nebulitic pegmatites crosscut these structures, indicating that D3 deformation occurred at temperatures greater than the solidus for the host garnet-bearing, leucocratic gneiss.

D3 folding occurs within locally derived low strain zones where folding of the S2 foliation occurs in centimetre-scale lenses that encase S-type folds (Figure 5b). The fold hinges are parallel to slightly oblique to the local mineral lineation (refer to stereonets presented with Figures 3; a, b, c, d & e). Isoclinal folding of leucosomes that are parallel to the S2 foliation is attributed D3 deformation. Fold hinges are parallel to the down dip mineral lineation (Figure 5c; 7). Folding and boudinage of leucosomes occurs within regions of localised low strain which are also sites of pegmatitic partial melt accumulation. Crosscutting pegmatites (D3) migrated away from high strain zones and form within boudin necks and fold hinges of leucosomes within the lower strain regions of the garnet bearing leucocratic gneiss (Figure 7). The presence of garnet porphyroblasts within the deformed leucosomes suggests that D3 occurred close to, or just after peak metamorphism.

5.4 *D4 Structures*

Large, pegmatites containing biotite-plagioclase-K-feldspar and quartz crosscut all prior structures (Figure 7). Conjugate pegmatite veins are observed at Redgate Beach, Cape Freycinet and Honeycombs, the orientation of the vein sets are consistent with late E-W to NE-SW extension. A pyroxene-hornblende-biotite mafic dyke (Figure 5f) north of Cowaramup Bay crosscuts the dominant foliation. Its easterly dipping orientation suggests post-peak metamorphic E-W extension.

6 Metamorphic Petrology

Mineral assemblages within the gneissic lithologies reflect upper amphibolite to granulite facies metamorphism. Prior petrographic data presented by Wilde and Murphy (1990) and Wilde (1999) suggest that the felsic gneisses are derived from granitoids that range in composition from sodic granodiorites to alkali granites. The classification scheme of Wilde and Murphy (1990) identifies six subdivisions of felsic gneisses. Samples presented in this study are identified with respect to this classification scheme, however, distinctions have been made largely on the presence or the absence of key metamorphic minerals such as garnet, hornblende, orthopyroxene and clinopyroxene. The localities of samples presented in this study are presented in Figure 2 and mineral assemblages are summarised in Table 3. Photomicrographs illustrate key petrological relationships in Figure 8.

6.1 *Alkali Feldspar granitic gneiss – Cape Naturaliste* (Figure 2)

Previously deemed the Hamelin granite (Myers, 1994) and mapped as the 'Pink granite gneiss' by Collins (2003). This lithology is dominated by crystalline alkali feldspars, plagioclase and quartz. Composition varies locally, with the presence or absence of hornblende. Detailed mapping of the northern Leeuwin Complex by Collins (2003) identified an additional, compositionally different component, the grey granodiorite gneiss, interlayered within the pink granite gneiss. The existence of rare garnet within this rock had not previously been identified. However, samples RVLC080 (Canal

Rocks) and RVLC084 (Sugarloaf) contain 5-10mm garnet porphyroblasts within granoblastic assemblages of quartz, K-feldspar, plagioclase and biotite. Garnet is commonly enveloped by minor biotite and contains inclusions of magnetite (Figure 8f).

6.2 *Garnet-bearing leucocratic granite gneiss – Honeycombs* (Figure 3a)

Classified by Wilde and Murphy (1990) as Type 1 felsic gneiss, the granite gneiss at Honeycombs (Figure 2) contains abundant leucosomes that are parallel to the D2 foliation and contain 5 – 20mm garnet porphyroblasts. The presence of garnet within the leucosomes suggests that they are a product of biotite dehydration reactions, associated with partial melting (Brown & Pressley, 1999). Quartz, plagioclase and K-feldspar makeup the dominant leucosome assemblage, while elongate biotite grains form selvages on leucosome boundaries (Figure 6). Small (<2mm) relict garnet prophyroclasts are enveloped within the foliation which is defined by plagioclase and biotite. Accessory magnetite and ilmenite often accompanies mafic minerals throughout the Leeuwin Complex. The localised existence of garnet at this location is an example of the compositional variation between various locations within rock units.

6.3 *Orange, felsic leucocratic granite gneiss – Willyabrup Cliffs* (Figure 3b)

This rock is compositionally different to the garnet-bearing leucocratic granitic gneiss in the obvious lack of garnet. It comprises foliation parallel leucosomes of quartz, K-feldspar and plagioclase that are commonly boudinaged in which K-feldspar pegmatites have accumulated during deformation. The pervasive foliation is defined by elongate biotite, plagioclase and minor hornblende minerals that also reflect the down-dipping mineral-stretching lineation. Globular intergrowth of hornblende and plagioclase up to 1cm in diameter are likely to be resultant from garnet grains that have been completely retrogressed.

6.4 *Massive granitic gneiss – Cowaramup Point* (Figure 3c)

Classified by Wilde and Murphy (1990) as Type 5 felsic gneiss, the unit is predominantly composed of a granitic assemblage of quartz, K-feldspar and

plagioclase. Local compositional variations include ortho and clinopyroxene and minor biotite (Figure 3c). The granitic gneiss contains a weak foliation, defined by plagioclase and quartz mineral alignment.

6.5 *Garnet bearing granite migmatite gneiss Redgate Beach to Cape Freycinet* (Figure d & e)

Referred to as the type 1 felsic gneiss (Wilde and Murphy, 1990), this unit is much more intensely deformed than the Type 1 felsic gneisses to the north. Janssen *et al* (2003) imply that the presence of feldspar augen indicates that the fabric is locally mylonitic. Hornblende, biotite and plagioclase define the strong, easterly dipping foliation and down-dip lineation. 1-10mm garnet porphyroblasts occur throughout the rock. Small <2mm garnets grains accumulate within elongate lenses parallel to the foliation. Hornblende contains oxide inclusions and is commonly enveloped by aligned biotite grains.

6.6 *Garnet, clinopyroxene, hornblende anorthosite gneiss – Sarge Bay* (Figure 2)

Garnet bearing, hornblende-plagioclase gneiss that was considered by Myers (1990b) to be part of the dismembered Proterozoic age Augusta Complex (classified as anorthosite by Wilde and Murphy (1990). It contains garnet porphyroblasts that range from 2-10mm in size. Many garnet grains contain plagioclase-hornblende coronae and contain plagioclase inclusions. Accessory titanite occurs with hornblende porphyroblasts that have minor biotite envelopes (Figure 8b). Quartz, plagioclase and K-feldspar isolate clinopyroxene from other minerals. Ilmenite and magnetite occur in proximity to hornblende grains.

6.7 *Amphibolites*

6.7.1 Hornblende-biotite ± garnet amphibolites

Amphibolite layers occur throughout all lithologies, often preserving folded remnants of the initial S1 fabric. Amphiboles are composed of hornblende-biotite-plagioclase-quartz ± garnet, orthopyroxene and clinopyroxene. The alignment of elongate biotite,

hornblende and plagioclase minerals defines the foliation and accompanying downdip mineral lineation. Biotite minerals often envelope sparse, skeletal orthopyroxene grains (Figure 8d). The most notable mineralogical change within amphibolites is the presence of garnet in these layers throughout the central domain. Garnets occur as porphyroblasts that vary in size (5– 100mm) depending on the locality. Decompression textures of hornblende, biotite and plagioclase form coronae around garnets garnet (Figure 8e) and in some cases completely replace. The occurrence of theses decompression textures at Willyabrup and Honeycombs are likely to result from rapid cooling during exhumation.

Relic grains of ortho and clinopyroxene occur within an amphibolite layer at Willyabrup Cliffs (Figure 3b). Orthopyroxene is overgrown by aligned biotite and hornblende minerals, whilst minor clinopyroxene is enveloped by plagioclase corone. The occurrence of these minerals suggest that these amphibolites were emplaced before peak metamorphism and may correspond to the crystallisation age of 540 ± 5 Ma of a monzogranite dyke at Cowaramup Bay, to the south (Nelson, 1996).

Small 'stringer' like amphibolites are composed of hornblende-biotite-plagioclase and quartz. These layers often contain recumberant and pygmatitic folds that are axial planar to the local mineral lineation. Larger layers are isoclinally folded with large garnet porphyroblasts (20-100mm) forming within fold hinges and along the boundaries of amphibolites.

6.7.2 Pyroxene-hornblende-biotite mafic dyke

Pyroxene-hornblende-biotite bearing mafic dykes located at Willyabrup and north of Cowaramup Bay. The Cowaramup bay dyke dips ~35/090, is structurally and mineralogically different to other amphibolites within the Leeuwin Complex. Nelson (1995) constrained the emplacement such dykes to 524 ± 12 Ma and suggested that metamorphic grade was low at this time. This crystallisation age is significantly younger than other previously reported ages presented by Nelson (1995; 1996; 1999). The presence of ortho and clinopyroxene suggests that the dyke may not have experienced peak metamorphism and the preserved mineral assemblages reflect igneous

crystallisation. The orientation of the easterly dipping mafic dyke is consistent with late E-W extension.

7 Mineral chemistry

In order to constrain the thermobarometric evolution of the Leeuwin Complex, mineral compositions of selected rock samples (shown in Figure 2 and mineral assemblages are summarised in Table 2) were measured using Electron Microprobe Analysis (refer to 8.1 *P-T analytical procedures*). Mineral Analyses for all samples are presented in Appendix 5(on disc), where Fe^{3+} has been calculated using the software AX (a product of Holland and Powell, 1998). A summary of mineral chemistry for each petrological group is presented in Table 3.

7.1 *Garnet*

Garnet composition is relatively homogeneous throughout the felsic gneisses of the Leeuwin Complex, where almandine-grossular dominates the solid solution, with X_{Fe} ($X_{Fe} = Fe^{2+}/Fe^{2+}+Mg+Mn+Ca$) generally varying between 0.58 – 0.72 and X_{Ca} ($X_{Ca} = Ca/Fe^{2+}+Mg+Mn+Ca$) falling within the range of 0.1 to 0.2. A notable difference in garnet composition is observed between the garnets within the felsic gneisses and within the amphibolites, where the presence of andradite increases the grossular content X_{Ca} to 0.2 – 0.35. A similar effect is seen within the garnets of the anorthosite samples from Sarge Bay where X_{Ca} = 0.29 – 0.39. This is not the case for sample *RVLC045* where a transect line (Figure 8c) reveals that pyrope is significantly higher with X_{Mg} ($X_{Mg} = Mg/ Fe^{2+}+Mg+Mn+Ca$) ranging from 0.23 – 0.26 within the garnet core and X_{Mg} = (0.14 – 0.24) across the garnet rims. The garnet transect is shown in Figure 9, and reveals subtle compositional variations from the core to the rim of the garnet. The core is relatively homogeneous in composition, whilst a ~300μm rim has an evident decrease in X_{Mg} from 0.24 (outer core) to 0.14 at the outer most rim. This is accompanied by an increase in X_{Fe} from 0.67 to 0.75. This chemical zoning is interpreted as a product of the rock's cooling history (i.e. O'Brien, 1997).

7.2 *Hornblende*

A majority of analysed hornblendes are classified within the calcic amphibole group (Leake *et al.* 1997) as hornblende are generally composed of ferroactinolite-pargasite and have Ca_{β} = 1.6-1.8, Na_{β} = 0.4-0.5, $(Ca+Na)_{\beta}$ = 0.6-0.8 and the X_{Fe} (X_{Fe} = Fe2+/Fe^{2+}+Mg) value of 0.5-0.8 and X_{Mg} (X_{Mg} = Mg/Fe^{2+}+Mg) 0.2-0.4. Hornblende within the Sarge Bay anorthosite gneiss are compositionally similar to the Bunker Bay felsic gneiss, where Ca_{β} >1.9, Na_{β} is 0.3-0.4 and X_{Fe} ranges from 0.82-0.83 and X_{Mg} is 0.21-0.29. Hornblendes within the Willyabrub amphibolites are comparatively magnesian, with X_{Mg} 0.58-0.63.

7.3 *Biotite*

Biotite is Ti-rich throughout all petrological samples, with X_{Ti} (X_{Ti} = Ti/Fe+Mg+Al+Ti) ranging between 0.04 – 0.07 based on eleven oxygen atoms. Felsic gneiss samples are typically annite-phlogopite in composition, with X_{Fe} (X_{Fe} = Fe/Fe+Mg+Al+Ti) ranging 0.25-0.45 and X_{Mg} (X_{Mg} = Mg/Fe+Mg+Al+Ti) having a similar compositional variation of 0.2-0.45. Biotite analyses from samples *RVLC051/052* are typically sodic with X_{Na} (Na/Na+K) ranging from 0.07-0.11, which is significantly higher than the X_{Na} 0.007-0.05 range expressed in felsic samples. These samples are also more magnesic with X_{Mg} 0.58-0.62.

7.4 *Clinopyroxene*

The only analysed petrological samples to contain clinopyroxene are *RVLC008/009* of the Sarge Bay anorthosite gneiss. All clinopyroxene analyses plot within the Ca-Mg-Fe quadrilateral, as Ca+Mg+Fe^{2+} values consistently range between 1.7-1.9 and Na_{β} values being <0.03. Analyses are typically calcic, with diopside being the dominant end-member, where X_{Ca} = 0.44-0.48 (X_{Ca} = Ca/Ca+Mg+Fe^{2+}+Fe^{3+}+Mn) and ferrosilite-enstatite making up the composition with X_{Fe} = 0.2-0.4 and X_{Mg} = 0.25-0.35.

7.5 *Orthopyroxene*

Analyses of orthopyroxene are limited to samples *RVLC051 & 052*, from a garnet-bearing amphibolite at Willyabrup Cliffs. Analyses are within the ferrosilite-enstatite field, with X_{Fe} = 0.35-0.45 and X_{Mg} (X_{Mg} = Mg/ Ca+Mg+Fe^{2+}+Fe^{3+}+Mn) ranging between 0.55-0.62, which is enhanced by the presence of Mg-Tschermak pyroxene.

7.6 *Feldspar*

Plagioclase is compositionally variable throughout samples, with a majority of samples being sodic, within the albite field, where X_{Ab} (X_{Ab} = Na/Na+Ca) = 0.5-0.7, while the samples of the anorthosite gneiss are typically lower, as X_{Ab} ranges between 0.38-0.51. Anorthite content is relatively consistent as X_{Ca} (X_{Ca} = Ca/Ca+Na+K) ranges between 0.38-0.50. K-feldspar analyses are sanidine enriched with K_β >0.85 and $(K+Al)_\beta$ = ≥2.0. In contrast albite content is typically low with X_{Na} (X_{Na} = Na/ Na+K) ranging between 0.09-0.20.

7.7 *Iron Oxides*

Ilmenite is present within a majority of samples and is generally composed of a ilmenite-hematite solid solution, with X_{Ilm} (X_{Ilm} = Ti/Ti + $^1/_2Fe^{3+}$) ranging between 0.85-0.95. Titanomagnetite is compositionally consistent with X_{Ti} (Ti/Fe+Ti) *ca* 0.51. Magnetite is compositionally uniform with X_{Fe3+} (Fe^{3+}/Fe^{3+}+Fe^{2+}+Al) ranging between 0.60-0.65. Minor spinel is present with $(Mg+Al)_\beta$ = 0.35-0.45.

8 Metamorphic *P-T* estimates and age constraints for the Leeuwin Complex

Average P-T estimations are presented from fourteen samples from the Leeuwin Complex (Figure 2.) and are presented in Table 4. All Microprobe analyses used for THERMOCALC analyses are presented in Appendix 1.

8.1 *P-T Calculations – analytical procedure*

Pressure and temperature (P-T) calculations were conducted using mineral analyses obtained from the electron microprobe. Microprobe spot analyses were performed on the Cameca SX51 Electron Microprobe with SAMAX software, at Adelaide

Microscopy, Adelaide University. Analyses were carried out under standard operating conditions, with an accelerating voltage of 15kV and a beam current of 20nA. Ten elements: Fe-Mn-Cr-Ti-Ca-K-Si-Al-Mg-Na were measured using wavelength dispersive spectrometers to determine the relative oxide wt (%) for each mineral analysis. Samples selected for Microprobe analyses had peak mineral assemblages containing garnet, plagioclase ± biotite, hornblende, orthopyroxene, clinopyroxene and accessory oxides; ilmenite, spinel and magnetite. Analyses were preformed on the cores and rims of minerals to best determine mineral compositions at i) peak metamorphic conditions and ii) retrograde conditions.

The mineral assemblages obtained by microprobe analysis were converted to mineral activities using the software AX (Holland & Powell, 1998). Average P-T estimates were calculated using THERMOCALC 3.21 and based upon the mineral activities generated by AX (and the internally consistent dataset of Holland and Powell (1998)). THERMOCALC calculates the optimal metamorphic conditions from the thermodynamics of an independent set of reactions between mineral endmembers (Holland & Powell, 1998). Calculations were made utilising the average temperature, average pressure and average P-T approach (Powell & Holland, 1994) in which a P-T intersection is statistically constrained by a X^2 test, to best reflect the metamorphic conditions at which mineral equilibrium was achieved. Fe – Mg exchange-thermometry calculations using garnet-biotite, garnet-hornblende, garnet-orthopyroxene and garnet-clinopyroxene thermometers were also performed to provide a comparative value to which the susceptibility of each sample to varied water activities could be compared.

In order to improve the accuracy of P-T estimations, end-members that failed the X^2 test, or that did not conform with the remaining data set were removed and P-T estimates recalculated. Reasons to omit an endmember from calculations include; poor mineral analyses, problems with retrograde equilibrium, or insufficiently constrained activity-composition models. Endmembers such as hematite, pargasite and spinel were common outliers and retrograde mineral end-members such as sanidine were common outliers that were removed from calculations so an independent set of reactions were able to pass the X^2 test at the 95% confidence level. A THERMOCALC output file representing the method utilised in calculating average T, average P and average P-T is presented in Appendix 2.

8.2 *Effect of water activities on P-T calculations*

The relative hydration at the time of metamorphism is a poorly known factor. Therefore, in order to reduce the window for experimental error, low water activities were used and where possible water was omitted from calculations. Given the presence of ubiquitous partial melt in the terrain, it seems reasonable to assume that H_2O was not in excess. Activities of H_2O were chosen to provide the best fit between aH_2O independent temperature estimates and aH_2O dependant estimates. By comparing values to temperature estimates generated using the Fe-Mg exchange equilibria, which operate independently of water activity models the accuracy of estimates can be evaluated. Calculations presented in Table 4 assume best fit water activities, yielding data that pass the X^2 test (95% confidence level) and where possible, have the lowest standard error. Where water activities do not have a significant effect on calculations, H_2O has been excluded.

8.3 *P-T estimates*

A summary of P-T estimates is presented in Table 4. Sample locations and their calculated peak and retrograde P-T conditions are shown in Figure 10. Peak metamorphic calculations based on mineral core analyses indicate that peak *P-T* conditions of 650 - 750°C and 6 - 8 kbar were attained throughout the Leeuwin Complex. Retrograde conditions were estimated from rim compositions and yielded temperatures 50 - 100°C cooler and pressures 0.5 – 1 kbar less than peak metamorphic conditions. Weighted means for selected average *P-T* estimates (highlighted in Table 4) have been calculated to reflect the *P-T* conditions for each of the structural domains (Figure 10). A weighted mean of average *T* and average *P* give peak metamorphic conditions of *c* 681 ± 58°C (MSWD = 0.04) and 7.8 ± 1.0 kbar (MSWD = 0.04) from three analyses within the southern domain. A weighted mean of seven analyses from the central domain give a weighted mean average *T* of 694 ± 36°C (MSWD = 1.0) and a weighted mean average *P* of 6.94 ± 0.79 (MSWD = 0.32). A weighted mean of two mineral core analyses form the northern domain give a weighted mean peak average *T* of 671 ± 130°C (MSWD = 0.60) and a weighted mean average P of 6.5 ± 1.9 kbar (MSWD = 0.54). This suggests that peak metamorphic temperatures were 680 ± 15°C

throughout the Leeuwin Complex. However, peak weighted mean pressures reveals a moderate decrease from 7.8 kbar in the southern domain, to 6.94 in the central domain and to 6.5 kbar in the northern domain. This suggests that pressures decreased northward by 1.3 kbar during peak metamorphism.

Similarly, this trend is seen within mineral rim retrograde average T and average P calculations, where a weighted mean for the southern domain (n=3) gives retrograde conditions of 657 ± 58°C (MSWD = 0.07) and 6.7 ± 1.0 kbar (MSWD = 0.04). The weighted mean for retrograde conditions within the central domain (n=7) gives retrograde conditions of 638 ± 22°C (MSWD = 1.04) and 6.25 ± 0.76 kbar (MSWD = 0.14), and a weighted mean of retrograde conditions in the northern domain (n=2) of 621 ± 120°C (MSWD = 0.012) and 5.5 ± 1.7 kbar (MSWD = 0.88). The weighted mean calculations suggest a progressive decrease in retrograde pressures from ~6.7 kbar in the southern domain to 5.5 kbar in the northern domain. This suggests that pressures decreased northward across the Leeuwin Complex by 1.3 kbar at near isothermic conditions during retrograde metamorphism.

9 LA-ICPMS and SHRIMP U-Pb Geochronology

A total of six monazite and four zircon samples have been analysed in this study to constrain the age of peak metamorphism. Zircons and monazites were extracted from selected whole rock samples (Figure 2 and summarised in Table 5). Samples were separated from crushed rock by heavy liquid (methyl iodide) and magnetic separation. Individual grains were randomly handpicked and mounted in epoxy resin and then polished. Zircons for SHRIMP analysis were coated in a thin coat of gold and monazites coated with carbon to ensure consistent resistivity across the mount during imaging. The mounts were then imaged using the Philips SEM XL20 at Adelaide Microscopy, University of Adelaide. Monazites were scanned at operating conditions of 15 kV to produce backscatter electron (BSE) images and zircons were imaged using the cathodoluminescence technique to reveal distortions in the crystal lattice (Stevens *et al.* 2000; Collins, 2003).

9.1 *LA-ICPMS – analytical procedure*

Monazites were analysed using the Laser Ablation Inductively Coupled Plasma Mass Spectrometer (LAICPMS) at Adelaide Microscopy, Adelaide University. The methods and procedure of Reid *et al.* (2006) were followed. Th – U – Pb isotopes were analysed under standard operating conditions using a laser spot size of 15μm, a firing rate of 5 Hz and an output reading of 65%. Helium gas was introduced in to the chamber between samples for the removal of matrix interferences between analyses. The chamber was analysed for 30 seconds prior to firing (40 seconds for zircon) and the laser was fired for a period of 10 seconds prior to analysis which ran for a period of 40 seconds to ensure ample measurement of isotopic ratios.

The Pb/U isotropic ratios were corrected for instrument induced differential mass fractionation of Pb and U by repeat analysis of the in house standard MADEL prior to and after analysis of the unknown sample. The program GLITTER was used to determine the fractionation trends between U and Pb during each standard analysis. Monazite ages were calculated using the MADEL monazite standard to correct for U-Pb fractionation (TIMS normalisation data: $^{206}Pb/^{238}U$ = 514.8 Ma, $^{207}Pb/^{235}U$ = 510.4 Ma: Payne *et al.* 2008; Wade *et al.* 2008) Over the duration of this study the weighted mean ages for MADEL analyses are $^{206}Pb/^{238}U$ = 512.6 ± 1.2 Ma (MSWD = 2.1) and $^{207}Pb/^{235}U$ = 511.0 ± 1.1 Ma (MSWD = 2.2), and were obtained from 86 analysis of the MADEL standard. Accuracy was monitored by repeat analyses of the in-house internal monazite standard (94-222/ Bruna-NW: $^{206}Pb/^{238}U$ = 447 Ma: Payne *et al.* 2008; Wade *et al.* 2008) the reported $^{206}Pb/^{238}U$ weighted mean age for the internal standard was 447 ± 4 Ma (MSWD = 3.6) (n=16).

9.2 *Monazite morphology*

Monazites from selected samples are pale yellow, contain rounded terminations and vary from 100 x 50μm to 300 x 200μm in size. Backscatter electron images reveal bright and dark monazites which generally reflect high and low thorium contents, respectively (Zhu and O'Nions, 1999). A majority of monazites contain no distinguishable zoning, however, many have minor mineral inclusions. A small majority of monazites from Cosy Corner and Honeycomb Cliffs contain minor oscillary

zoning with bright centres and dim rims. As thorium has a high atomic mass and can vary significantly in concentration in monazite, it has a significant impact on BSE imagery and therefore compositional zoning. Therefore BSE zoning may only indicate thorium concentrations and may not reflect age zoning (Zhu and O'Nions, 1999; Swain *et al.* 2005). Backscatter images of monazite grains are presented in Appendix 2, where spot analyses are quoted with corresponding $^{206}Pb/^{238}U$ ages.

9.3 *LA-ICPMS monazite age data*

All LA-ICPMS monazite data are graphically presented using concordia and weighted mean plots in Figures 13-18, and analytical data are presented in Table 6. Sample localities are shown in Figure 12, along with their associated age estimates from this study and previously published data. All ages quoted are $^{206}Pb/^{238}U$ ages unless specified otherwise.

9.3.1 RVLC003 – Skippy Rock

Sample RVLC003 is a coarse grained, diffuse, nebulitic pegmatite, interpreted to result from partial melting. It contains garnet-biotite-plagioclase-K-feldspar phenocrysts-quartz and magnetite. The leucosomes contain ptygmatic folding and contain granoblastic garnets ranging from 1-5cm in diameter. This suggests that partial melting was synchronous with D3 deformation as previously suggested by Janssen *et al.* (2003). Garnet growth within these leucosomes is therefore likely to reflect peak metamorphism. Similarly, monazite in the leucosome is interpreted to be a product of metamorphism.

A total of 21 analyses were preformed on the equivalent number of monazite grains (Table 6) from this sample. Graphic presentation of $^{206}Pb/^{238}U$ ratios using a concordia diagram (Figure 13a) reveals that most data are concordant, with several ages plotting below concordance. Analyses suggest that metamorphism occurred during 510-545 Ma. A probability plot (Figure 12b) suggests that there are three discrete age populations, with peaks at 540 ± 1 Ma; 524 ± 2 Ma and 512 ± 2 Ma. An alternate interpretation is that these ages reflect one metamorphic event, which is represented by a weighted mean average of 18 analyses yields a $^{206}Pb/^{238}U$ age of 525 ± 5 Ma (MSWD = 9.3).

Omitting 7 analyses that are <95% concordant, leaves the remaining 11 concordant analyses (>95% conc.) to give a $^{206}Pb/^{238}U$ age of 532± 4 Ma (MSWD = 2.4) that is interpreted as the age of monazite crystallisation. No prior geochronology has been published from Skippy Rock, however unpublished data quoted in Janssen *et al.* (2003) constrain peak metamorphism and partial melting to 550-500Ma. Therefore, 532 ± 4 Ma interpreted as the best timing of peak metamorphism.

9.3.2 RVLC020 – Cosy Corner

Sample RVLC020 is a granitic gneiss composed of garnet-hornblende-biotite-titanite-ilmanite-plagioclase-K-feldspar and quartz. The sample has been taken from a pegmatitic layer where the foliation is defined by hornblende and biotite minerals. Diffuse, K-feldspar rich melts contain granoblastic garnets >10mm which are interpreted as a product of peak metamorphic conditions. Garnets within the gneiss overgrow remnant hornblende. Pegmatitic melts within the outcrop are restricted to shear zones which constrain partial melting to the last stage of deformation.

A total of 21 analyses were performed on 21 monazite grains from sample RVLC020 (Table 6), however five grains have been excluded as $^{206}Pb/^{238}U$ ratios were uncharacteristically low and therefore the grains were unlikely to be monazite. The remaining 16 analyses are mostly concordant (Figure 14), with the discordance pattern consistent with the recent redistribution of radiogenic Pb. Analysis 11.1 has a $^{206}Pb/^{238}U$ age of 569 ± 4 Ma and plots slightly higher than the concordia line and is interpreted as having lost some radiogenic U. Analysis 9.1 has a concordant $^{206}Pb/^{238}U$ age of 536 ± 4 Ma which reflects similar metamorphic ages throughout the Leeuwin, however the majority of analysis for this sample reflect a younger metamorphic age. A calculated discordia Tera-Wasserberg plot (Figure 14(b)) shows the effect of common ^{204}Pb on data, where data points are moderately discordant. Analysis 10.1 has a $^{206}Pb/^{238}U$ age of 452 ± 3 Ma. If experimental error is excluded, then the remaining analyses are interpreted to represent a single population which is likely to reflect peak metamorphism from 500 to 520Ma. Seven concordant analyses (>95% conc.) provide a weighted mean of 503 ± 5 Ma (MSWD = 2.8) (Figure 14c).

A previous sample from this rock was dated by Nelson (1996). His SHRIMP U-Pb zircon analysis revealed a metamorphic age of 605 ± 36 Ma and a protolith age of 779 ± 23 Ma. This data was later questioned by Collins (2003) who concluded that; "either the rocks Nelson (1996) analysed experienced a different metamorphic history, or the *ca* 605 Ma metamorphic event is an artefact of insufficient data". An alternate interpretation is that this age dates an earlier metamorphic event prior to peak metamorphism at 503 ± 5 Ma. However, there is no petrological evidence for multiple metamorphic events with the Cosy Corner location.

9.3.3 RVLC025 – Cape Freycinet

Sample RVLC025 is taken from a diffuse, nebulitic pegmatite within a highly deformed garnet-bearing migmatite gneiss. Pegmatites crosscut the easterly dipping foliation and biotite defines the pervasive foliation Garnet minerals 2-15mm in diameter occur as porphyroblasts throughout the gneiss. The mineral assemblage for the sample is garnet-biotite-titanite-magnetite-ilmenite-plagioclase-K-feldspar and quartz.

A total of 21 analyses were preformed on 21 monazite grains from this sample (Table 6). One analysis yielded Pb/U ratios that do not reflect a monazite composition and this analysis has therefore been excluded from calculations. The remaining 20 analyses plot concordantly on a Concordia diagram (Figure 15a). Analysis 15.1 has a concordant $^{206}Pb/^{238}U$ age of 480 ± 3 Ma. A probability plot (Figure 15b) suggests that monazite growth occurred at three stages; 530 ± 1.5 Ma, 519 ± 2 Ma and 480 ± 3 Ma. An alternate interpretation is that the monazite data represents a single population. 18 analyses (>95% conc.) produces a $^{206}Pb/^{238}U$ age of 524.3 ± 3.2 Ma (MSWD = 4.0) (Figure 12c) that is interpreted as dating the metamorphism in this rock.

9.3.4 RVLC046 – Willyabrup Cliffs

Sample RVLC046 is a hornblende-biotite-plagioclase-quartz granite gneiss, that has weathered to a distinctive orange. This occurs structurally above the garnet-bearing amphibolite layers of Willyabrup Cliffs. Thin sections indicate that minor garnet (<1mm diameter) has been replaced by plagioclase and hornblende.

A total of 20 analyses on 20 monazite grains from sample RVLC046 (Table 6; Figure 16), with the omission of 1 discordant analysis, the remaining data yields a $^{206}Pb/^{238}U$ weighted mean age of 520 ± 8 Ma (MSWD = 5.6). All analyses appear to reflect a single Gaussian population and with the omission of one apparent outlier the remaining 18 analyses gives a $^{206}Pb/^{238}U$ mean age of 519 ± 5.2 Ma (MSWD = 2.2). Analysis 13.1 has a $^{206}Pb/^{238}U$ age of 490 ± 7 Ma which is negatively discordant and is interpreted to have lost some radiogenic Pb. The weighted mean age of 520 ± 8 Ma (data >95% concordant) is interpreted as constraining the metamorphic age of this rock.

9.3.5 RVLC070 – Honeycombs

This sample is a garnet-biotite-magnetite-plagioclase-K-feldspar-quartz bearing pegmatite. This sample has been taken from a diffuse vein that cross-cuts the local foliation of the garnet ± hornblende bearing gneiss. K-feldspar grains and garnet porphyroblasts up to 30mm within the pegmatite are a likely product of partial melting. Leucosomes from the gneïss feed into the crosscutting pegmatite veins, suggesting that partial melting of the gneiss occurred during metamorphism.

A total of 22 analyses were performed on 22 monazite grains from this sample (Table 6). Analyses 3.1, 5.1, 6.1, 7.1, 9.1 & 11.1 yielded a >85% concordant cluster of data that plot on the Concordia diagram at ~ 250 Ma (Figure 17a) and give a weighted $^{206}Pb/^{238}U$ age of 248 ± 2.9 Ma. These analyses plot on a discordia line that crosses the Concordia diagram at 544 ± 25 Ma and intercepts it again at 0 Ma. Therefore, these grains are interpreted being discordant due to radiogenic Pb loss. No previously published data has revealed any metamorphic disturbance within the Leeuwin Complex at this time. However, an alternate interpretation they may date metamorphic disturbance prior to the breakup of Gondwana (between the India and Australia-Antarctica segments) within the early Mesozoic (Direen *et al.* 2008).

The remaining analyses reflect a single population at 500-540 Ma. With the omission of 3 negatively discordant analyses, a weighted mean of 11 analyses (≥95% conc.) gives a $^{206}Pb/^{238}U$ age of 525 ± 3.2 Ma (MSWD = 1.9) (Figure 17c) which is analytically indistinguishable from the metamorphic age of 522 ± 5 Ma from Collins (2003) of the Sugarloaf gneiss which is located approximately 20km north of this location. Janssen *et*

al (2003) refers to unpublished U-Pb SHRIMP zircon analyses, where zircon rims reflect a metamorphic age of 500 – 550 Ma.

9.3.6 RVLC083 – Honeycombs

Sample RVLC083 is of the Honeycomb leucocratic granite gneiss which is composed of; garnet-biotite-ilmenite-magnetite-plagioclase-feldspar and quartz. The gneiss contains abundant centimetre scale leucosomes that contain biotite selvages. Garnet is concentrated in leucosomes with individual grains averaging 10-20mm and is the result of partial melting reactions (Janssen *et al.* 2003).

A total of 20 analyses were preformed on 20 monazites (Table 5) which has produced a single population (Figure 18a & b) around 500-540 Ma. Analyses 5.1 is negatively discordant. Excluding analysis 5.1 and 3.1, a weighted mean age for all other data is 520 ± 4.3 Ma (MSWD = 0.63) (Figure 18c). The two ages from both Honeycombs samples strongly both support metamorphism occurring at 520-525 Ma.

9.4 *SHRIMP – analytical procedure*

Samples RVLC034, 035 & 041 were analysed on the 27th and 28th of May 2008, U-Th-Pb isotopic data was processed on the SHRIMP 2 which is located in the John De Laeter Centre of Mass Spectrometry, Curtin University, Perth. The primary beam current during analysis was 2.0-2.5 nA and the mass resolution was ~5000. During the analysis session nine analyses of the CZ3 standard were obtained. With the omission of three outliers the remaining six standard analyses yielded a Pb/U spot to spot uncertainty of 2.12% (2σ) and a Pb*/U calibration error of 1.43 (2σ%). However, a standard slope of 2 was used in order to account for the long term stability of the instrument. Results indicate that common ^{204}Pb was largely present as a surface contaminant and therefore corrections to ^{206}Pb counts were made modelled on the composition of Broken Hill ore Pb. Analyses were targeted at zircon rims interpreted to have grown during metamorphism.

9.5 *Zircon Morphology*

Zircons from samples RVLC034, 035 & 041 are clear, pale yellow to a dirty orange. A majority of grains are subhedral to euhedral, whilst elongate grains have rounded terminations and vary greatly in size, ranging from 150 x 550μm to 40 x 100μm. Grains vary in complexity, from well preserved traces of oscillatory zoning to clear, brightly luminescing grains. In many cases brightly luminescent rims appear to have replaced original zircon, rather than have precipitated on a core (Collins, 2003). This is a possible indication that the Neoproterozoic zircon cores were partially reset during Early Cambrian granulite facies metamorphism (Collins, 2003). Cores are often distinguished by poorly luminescent bands and often contain minor fluid and mineral inclusions. In order to constrain the metamorphic age, zircon rims were targeted for analysis. Selected cathodoluminescent images of selected zircon rim analyses are presented with their corresponding $^{206}Pb/^{238}U$ ages in Appendix 3.

9.6 *SHPIMP – zircon age data*

All SHRIMP zircon data are graphically presented using concordia and weighted mean plots in Figures 17-19, and analytical data are presented in Table 7. Sample localities are shown in Figure 12, along with the associated age estimates from this study and previously published data. All ages quoted are $^{206}Pb/^{238}U$ ages unless specified otherwise. Figures 19-21 are graphical presentation of all zircon data.

9.6.1 RVLC034 – Merchant Rocks

This sample is taken from a diffuse, nebulitic, coarse grained pegmatite that is composed of hornblende-garnet-biotite-plagioclase-K-feldspar and quartz. This sample consists of a medium to coarse grained, granoblastic assemblage that is dominated by K-feldspar, plagioclase and quartz. The rock has a strong mineral alignment that is predominantly defined by biotite aggregates. Porphyroblasts of garnet occur throughout the sample and vary in size from 1mm up to 15mm. Minor replacement by plagioclase and feldspars occur within the outer envelope of garnet porphyroblasts. Accessory minerals include zircon, monazite and opaque oxides. The pegmatite crosscuts a migmatitic, garnet bearing gneiss, however is connected by diffuse, migmatitic veins to the network of leucosomes within the rock. The outcrop is dominated by a gneissic

foliation that dips shallowly to the east (12/086). Diffuse pegmatite veins crosscut the foliation, with veins forming conjugate structures.

A total of 12 analyses were preformed on 12 zircon rims (Table 7), several analyses appear to be subject to high ^{207}Pb values which could be attributed to the effect common lead (^{204}Pb) contamination. The subsequent data is presented on a concordia plot in Figure 19 which reveals two distinct age populations. Grain 12.1 lies concordantly with a $^{206}Pb/^{238}U$ age of 1088 ± 17 Ma which may reflect the age 1091 ± 8 Ma (Nelson, 1999) interpreted as the igneous crystallization of the monzogranitic precursor to the gneiss at Redgate beach 6km to the north. Based on the structural and compositional similarities of the rocks from Cape Freycinet to Redgate Beach, it is reasonable that they have been derived from the same monzogranite precursor and have experienced a similar metamorphic history (Janssen *et al,* 2003). Omitting analyses 1.1 which has high ^{204}Pb and 10.1 due to high Pb/U ratios which is likely to be caused by the loss of radiogenic Pb, the remaining population has a weighted mean age of 521 ± 8 Ma (MSWD = 1.5) (Figure 19c), which is considered to date metamorphism.

9.6.2 RVLC035 – Redgate Beach

This sample is a coarse grained, nebulitic pegmatite with a granoblastic assemblage of garnet-biotite-plagioclase-K-feldspar-quartz and opaques (magnetite and ilmenite). Biotite accumulates occur within the selvages of larger garnet porphyroblasts and small centimetre scale fractures. Garnet porphyroblasts (5-15mm) are scattered throughout the pegmatite and adjacent granite gneiss. The granite gneiss is compositionally and structurally similar to the outcrops of Cape Freycinet (refer to Merchant Rocks). Pegmatite veins crosscut the granite gneiss in conjugate sets which indicate late southeast-northwest extension (Janssen *et al.* 2003).

A total of 12 analyses were preformed on 12 zircon grains (Table 7; Figure 20) which has produced three distinct populations of zircons. Analysis 6.1 lies negatively discordant with a $^{206}Pb/^{238}U$ age of 1018 ± 14 Ma and a $^{207}Pb/^{206}Pb$ age of 1114 ± 48 Ma. The $^{206}Pb/^{238}U$ age of 1019 ± 14 Ma is similar to the zircon populations at 1005 ± 46 Ma & 1016 ± 10 Ma from Nelson (1999) which are thought to reflect a disturbance event.

Analyses 12.1 and 13.1 lie slightly below the Concordia line, and give a weighted mean $^{206}Pb/^{238}U$ age of 769 ± 29 Ma (MSWD = 0.044). Previous geochronology from Nelson (1999) does not reveal any zircon disturbances at this age. However, it is within error of the 779 ± 23 Ma event (Nelson, 1995) derived from 12 analyses from Cosy Corner interpreted as the age of granite crystallisation. Therefore, these zircons may have resulted from a magmatism associated with the emplacement of the *c* 750 Ma protoliths.

Analysis 8.1 lies concordantly above the main population with a $^{206}Pb/^{238}U$ age of 576 ± 8 Ma. The main population is represented by the weighted mean $^{206}Pb/^{238}U$ age of 519 ± 8Ma (MSWD = 1.8) (Figure 20c) from the remaining eight analyses. This peak metamorphic age is some 12 Ma younger than the 531 ± 64 Ma $^{207}Pb/^{208}Pb$ age of a single zircon grain (Nelson, 1999) that was previously interpreted by Janssen *et al.* (2003) as the age of metamorphism at Redgate Beach but correlates well with the 521 ± 8 Ma zircon age and the 524 ± 3 Ma monazite ages from Merchant Rocks, and is interpreted as dating the age of metamorphism.

9.6.3 RVLC041- Willyabrup Cliffs

This sample is a hornblende-biotite-ilmenite-magnetite-plagioclase-quartz bearing leucosome that feeds directly into a crosscutting pegmatite. The leucosome is located on the boundary of the garnet-bearing amphibolite and the orange-weathered gneiss. The leucosome is strongly boudinaged and nearby C-S fabrics indicate a NE-side down movement on the east dipping fabric.

A total of 9 analyses were preformed on nine zircon rims (Table 7; Figure 21) that identify two populations of zircon. Analyses 3.1, 5.1 and 6.1 are grouped at a weighted mean age of 544 ± 8 Ma and the remaining analyses yield a weighted mean age of 521 ± 8 Ma (MSWD = 1.2). This population is within error of the 519 ± 5 Ma age derived from the monazite data from sample RVLC046.

The mafic granulite, located structurally below the sample contains relic igneous ortho and clinopyroxene. Therefore, the weighted mean age of 544 ± 8 Ma may date early metamorphism of the two-pyroxene-hornblende mafic granulites, and the weighted

mean age of 519 ± 5 Ma is interpreted to date metamorphism of the garnet-hornblende-orthopyroxene-biotite mafic granulite.

10 Sm-Nd Isotopes

Eight whole rock samples from the Leeuwin Complex have been analysed in this study for Sm-Nd isotopes. The sample locations, petrology and Sm-Nd isotope data are summarised in Table 5 and isotope data is presented in Table 8.

10.1 *Sm-Nd analytical procedure*

Whole rock samples were crushed and powdered in a tungsten carbide mill. Approximately 0.05g of each sample were spiked with 0.4g of standard (Spike F: 1.91375 nm/g^{-1} Nd^{150} & 3.70847 nm/g^{-1} Sm) and evaporated in HF/HNO_3 for a period of four hours. Samples were disseminated in HF/HNO_3 within sealed Teflon bombs at 150°C for three days, and evaporated in HF/HNO_3. Samples were then evaporated in 6M HCL and then digested in oven heated Teflon bombs containing 6M HCL overnight. Isotope dilution methods were used to collect the Nd and Sm which were fused to tantalum and rhenium filaments respectively.

Nd isotope ratios were measured with the Finnigan MAT 262 mass spectrometer and Sm isotope ratios were measured with the Finnigan MAT 261 mass spectrometer. A blank run with the samples produced an Nd total of 2.5ppm and the TASBAS (in-house standard) yielded a $^{143}Nd/^{144}Nd$ ratio of 0.512896 ± 0.000006 (1σ). The $^{143}Nd/^{144}Nd$ ratio was normalised to 0.721903. The running average for La Jolla for the year was 0.511860 ± 0.000007 (1σ).

10.2 *Sm-Nd isotope results*

Data for the Sm and Nd concentrations and Nd isotopic ratios are presented in Table 8 and the Epsilon Nd values have been plotted on a conventional Nd evolution diagram (Figure 22). Epsilon Nd values have been plotted at the assumed protolith ages of 1090 Ma for samples RVLC034 & 035 as these samples are likely to have been inherited

from the syncollisional Mesoproterozoic protolith (Nelson, 1999; 2002; Fitzsimons, 2003; Janssen *et al* 2003). All other samples have been plotted at 750 Ma which can be interpreted as a relatively homogenous protolith age for the remaining samples. Epsilon Nd data from the Grove Mountains (Liu *et al,* 2007), East Antarctica and Natal, Southern Africa (Wareham *et al*, 1998) are also plotted.

11 Discussion

11.1 *Implications for a structural model for the central Leeuwin domain*

Previous geochronology has suggested that there are two igneous protolith ages of the igneous gneisses within the central domain of the Leeuwin complex. SHRIMP zircon dating has revealed a Mesoproterozoic age of 1090 Ma for the precursor to granite gneiss of Redgate Beach (Nelson, 1999) and a ~750 Ma protolith for locations within both the central and northern domains (Nelson, 1996; Collins, 2003). No evidence for a crosscutting, or a contact boundary between these protoliths was found whilst mapping the central domain. This may be because; contact boundaries are preserved beneath Pleistocene beach alluvium, or that peak metamorphism during the early Cambrian alleviated any compositional differences between the two protoliths.

The granitic gneiss at Honeycombs is considered to be a successor of the *c* 750 Ma protolith, as this is considered to be the igneous crystallisation age of a compositionally similar rock ~10 km north of this location (Canal Rocks) (Nelson, 1996). Preserved traces of the S1 foliation within folded amphibolite layers (Figure 4) are axial planar to the D1 folded amphibolite layer that cut the granitic gneiss. The cross cutting nature of the amphibole imply that D1 must have occurred after the emplacement of the 750 Ma protolith. An identical observation was made by Collins (2003) in the northern domain. Collins (2003) suggested that the coaxial and possibly the progressive relationship between D1 and D2 suggests that they were coeval, which is also likely within the central domain.

D2 folding within the central domain of the Leeuwin complex are interpreted is be a result of subvertical shortening that might have been in response to either crustal

thickening, or ductile thinning (Collins, 2003). D3 'kink' folds and disharmonic folds suggest sub-horizontal WSW-ENE shortening. The coaxial relationship between the folds of D2 and D3 with the L2 mineral elongation lineation, suggest that they were coeval. The presence of large garnet porphyroblasts within the D2 fold hinge of the amphibolite (Figure 5a) implies that D2 folding was synchronous with garnet growth and therefore peak metamorphism. Diffuse pegmatites, interpreted as being a product of partial melting (Janssen *el al.* 2003) are often associated with D3 'kink' folds (Figure 6) suggest that D3 is likely to have occurred during, or after high-grade metamorphism.

D4 deformation within the central domain is interpreted to be a product of east-west extension. Conjugate sets of pegmatites occur throughout the central domain, crosscutting the S2 foliation at orientations consistent with normal faulting. The crosscutting nature of the mafic dyke north of Cowaramup Bay is also likely to be a product of late extension. The absence of peak metamorphic minerals in both of these structures suggests that D4 occurred post peak metamorphism at *c* 522 Ma.

No apparent structures of the (D2) east-west, then north-northwest – south-southeast (D3) subhorizontal shortening reported by Collins (2003), for the northern, and Janssen *et al.* (2003) for the southern domain were observed within the central domain of the Leeuwin Complex. This suggests that; i) the central Leeuwin Complex experienced a different tectonic history, when compared to the northern and southern domains, or ii) the subhorizontal structures of the central domain could be a tectonic response to deformation within the northern and southern domains. However, evidence for a structural relationship between these domains is fickle, and more work is needed to be done in order to determine the structural associations between the domains to support this theory.

A tectonic model presented by Harris (1994) suggested that the Leeuwin Complex was part of regional sinistral transcurrent shear zone associated with the Darling Fault zone, where an extensional environment formed within a dilatational jog, in which the rocks of the Leeuwin Complex were intruded and subsequently deformed within a regime of progressive non-coaxial deformation (Harris, 1994). Harris (1994) reported north-south sinistral shear zones from the Leeuwin Complex. However, detailed mapping of the

northern (Collins, 2003) and of the central Leeuwin Complex (this study) has revealed no evidence for any ductile strike-slip deformation.

Based on field observations and structural relationships, two perspective structural models for the central Leeuwin domain are presented in Figure 23. The model for pure shear is based on subvertical compression being the dominant stress vector, whilst box fold sets and 'kink' fold measurements (Figure 6) suggest a bulk σ_2 stress is attributed to east-west to northeast-southwest shortening. The orientation of this strain vector is different to the D3 north-northwest–south-southeast shortening direction for the northern domain (Collins, 2003) and therefore suggests that D3 deformation within the central domain predates a rotation in the contraction vector associated with sinistral movement along the Darling Fault, or D3 is not associated with the reported movement along the Darling Fault Zone at 500-550 Ma (Harris & Li, 1995). The lack of any obvious kinematic indicators of sinistral movement in the northern domain (Collins, 2003) and the central domain (this study) suggests that the reported north-south sinistral shear zones of the Leeuwin Complex (Harris, 1994) are somewhat sceptical, and therefore the structural model for pure shear is favoured over the simple shear model.

11.2 *Metamorphic history*

Pressure-Temperature estimates from this study have obtained peak metamorphic conditions of 650 - 750°C and ~ 6 - 8 kbar and retrograde conditions ~100°C and 1kbar less than peak metamorphism. These conditions are comparable to recent calculations presented by Halpin *et al.* (2008) based on felsic gneiss mineral assemblages collected by dredge hauls, taken from the southern margin of the Naturaliste Plateau. Thermobarometric results indicate peak *P-T* conditions reached ~700°C and ~5.5 – 7.5 kbar, whilst rim compositions suggest that ~50-100°C of post-peak cooling occurred at near isobaric conditions (Halpin *et al.,* 2008).

Average *P-T* estimates for peak metamorphism presented in Figure 10 reveal a ~1.3 kbar pressure decrease at near isothermic conditions from south to north across the Leeuwin Complex. This is also seen in the mineral rim calculations that suggest retrograde conditions exhibited a ~1.2 kbar decrease in pressure and ~40°C decrease in

temperature from south to north. This dismisses a previous suggestion made by Wilde and Murphy (1990), who considered that the Leeuwin Complex experienced one metamorphic event, in which metamorphism changed progressively from amphibolite facies in the south to granulite facies in the north. However, variance in *P-T* conditions may be attributed to the lack of *P-T* calculations performed within the northern domain. Conversely, *P-T* estimates for samples from the northern domain are based on 4-7 independent sets of reactions, whereas average *P-T* calculations for the central and southern domains are based on 7 – 12 independent sets of reactions, which, along with the fact that weighted means were only based a limited number of *P-T* calculations, may contribute to misinterpretation.

As metamorphic garnet, orthopyroxene, horneblende and biotite occur throughout the Leeuwin Complex, it is likely that peak metamorphic conditions were relatively uniform. This is supported by graphic presentation of peak *P-T* estimates (Figure 11a,c), where probability density plots reveal Gaussian populations from which weighted mean calculations yield *ca* 687 ± 28°C (Figure 11b) and *ca* 7.24 ± 0.61 kbar (Figure 11d). These are interpreted as the peak metamorphic conditions for the whole Leeuwin Complex. Retrograde conditions calculated from mineral rim compositions also produce Gaussian populations from which weighted mean calculations generate *ca* 638±20°C and *ca* 6.3 ± 0.56 kbar for the Leeuwin Complex. These calculations dismiss previous suggestions that the Leeuwin Complex was a high temperature – low pressure terrane (i.e. Wilde & Murphy, 1990; Myers, 1994; Wilde, 1999) or that the whole complex was retrogressed to amphibolite facies during the *ca* 540 disturbance event. Rather, the Leeuwin Complex experienced peak metamorphism at *ca* 522 Ma and remained at mid crustal depths (~15-20 km) where moderate pressures existed following peak metamorphism.

Chemical zoning within garnet porphyroblasts (Figure 9) is interpreted to reflect the rocks cooling history, where the homogenous composition of the garnet core is a product of very slow average cooling, and the change in mineral composition within the garnet rim is a response to rapid cooling, driven by exhumation. Garnet-biotite thermometry (presented in Table 4) reveals retrograde conditions of ~600°C, however, ideal mixing of Fe-Mg within chemical equilibrium is difficult to ascertain, and inferred

P-T conditions may not be entirely reliable (Gessman *et al.* 1997). Therefore, this may not reflect the retrograde conditions experienced during exhumation.

^{40}Ar-^{39}Ar fusion dating of hornblende minerals by Nelson (2005) constrains the closure temperature for Ar loss from amphiboles to ~498 – 493 Ma for a range of samples located in Figure 12. Assuming the closure temperature for Ar in hornblende is ~530 ± 40°C (McDougall & Harrison, 1999), and that peak metamorphism temperatures were ~700°C, then an average cooling rate of ~6.3°C per million years can be assumed from peak metamorphism at *ca* 522 Ma to the closure temperature of Ar loss in amphiboles at ~495 Ma. However, a uniform cooling rate is unlikely, as indicated by the chemical zoning of garnets, where core compositions reflect stable to very slow cooling. In contrast garnet coronae contain hornblende-biotite-plagioclase decompression textures that are likely to be a product of rapid cooling caused by exhumation. Therefore it is likely that to a point, average cooling was very slow, which was then followed by a period of rapid cooling driven by exhumation.

11.3 *Geochronology*

Prior geochronological data (Wilde & Murphy, 1990; Nelson, 1996; 1997; 1999; 2002; Collins, 2003) indicate that the protolith of the Leeuwin Complex did not form a single contemporaneous suite, but magmatic intrusions that occurred over ~600 Ma (Collins, 2003). Nelson (1999) obtained a weighted age of 1090 Ma from a population of zircon analyses from the granite gneiss at Redgate beach. A single zircon grain (analysed in this study) from Merchant Rocks, south of Redgate beach yielded a $^{206}Pb/^{238}U$ age of 1088 ± 7 Ma. This zircon is interpreted as a xenocryst from the igneous crystallisation of the monzogranitic precursor, formed within a syncollisional origin (Fitzsimons, 2003).

Two zircon analyses from RVLC035, Redgate Beach give a weighted mean age of 769 ± 29 Ma, which are analytically similar the granite crystallisation age of 779 ± 29 Ma at Cosy Corner (Nelson, 1996) and to the 755 ± 3 Ma zircon age interpreted as the crystallisation age of the protoliths at Sugarloaf (Collins, 2003). This suggests that the

successor to the 1090 Ma protoliths were affected by metamorphism associated with the *ca* 750 Ma protolith emplacement.

High-grade, granulite facies metamorphism is well constrained to 520-530 Ma by LA-ICPMS monazite and SHRIMP zircon data presented in this study. Evidence for this is further supported by the previous geochronological data (Collins, 2003) that dates peak metamorphism at the Sugarloaf antiform (northern Leeuwin Complex) to *ca* 522 ± 5 Ma. This is analytically indistinguishable from the following $^{206}Pb/^{238}U$ ages;

- 525 ± 5 Ma from RVLC003, monazite analyses, Skippy Rock (Figure 13)
- 524 ± 3 Ma from RVLC025, monazite analyses, Round Rocks (Figure 15)
- 521 ± 8 Ma from RVLC034, zircon rim analyses, Merchant Rock (Figure 19)
- 519 ± 8 Ma from RVLC035, zircon rim analyses, Redgate Beach (Figure 20)
- 521 ± 8 Ma from RVLC041, zircon rim analyses, Willyabrup Cliffs (Figure 21)
- 519 ± 5 Ma from RVLC046, monazite analyses, Willyabrup Cliffs (Figure 16)
- 520 ± 4 Ma from RVLC070, monazite analyses, Honeycombs (Figure 17)
- 527 ± 3 Ma from RVLC083, monazite analyses, Honeycombs (Figure 18)

These ages have been determined based on weighted mean calculations of i) ≥95% concordant monazite data and ≥90% concordant zircon data and ii) data that reflects the main population of analyses. Older stages of zircon and monazite growth have been identified and are presented in probability density plots (Figures 13-21). Sample RVLC020, from Cosy Corner reflects a weighted mean age of 503 ± 5 Ma. A Tera-Wasserberg plot (Figure 14b) reveals that the data is slightly discordant and several analyses may be subject to common lead contamination, which may increase the ^{206}Pb, thus decreasing the $^{206}Pb/^{238}U$ ages. However, elevated ^{204}Pb levels were not recorded during analyses, therefore the $^{206}Pb/^{238}U$ age of 503 ± 5 Ma is interpreted as the age of peak metamorphism at Cosy Corner. This is some ~100Ma younger than 605 ± 36 Ma age from four zircon analyses from this rock by Nelson (1996), who interpreted them as dating peak metamorphism. However all four analyses are reversely discordant and have a weighted mean $^{206}Pb/^{207}Pb$ age of 550 ± 23 Ma. Collins (2003) speculated that these grains lie on a discordia line from the crystallisation age to a younger time of Pb loss making their age meaningless, and therefore suggested that evidence for an early metamorphic event at *ca* 615 Ma was far from conclusive.

Sample RVLC070 yields six analyses that plot on a discordia line from the crystallisation age of 527 ± 3 Ma (Figure 17). The weighted mean of this population is 247 ± 3 Ma (MSWD=3.0). As these analyses lie on a discordia line from the crystallisation age, they are interpreted as having lost some radiogenic Pb. No prior geochronological data from the Leeuwin Complex has revealed such Mesozoic ages. However, cretaceous age volcanic carapace overlie the Naturaliste Plateau to the east (Halpin *et al.* 2008). It is possible that these monazites are attributed to the hyperextensional breakup between Australia and Antarctica during the Mesozoic. It is possible that the *ca* 247 ± 3 Ma age represents monazite growth that could have been associated with transcurrent shearing caused by the northward progression of greater India. However, more monazite dating would be needed to be done in order to define monazite growth at this age and support this theory.

Evidence for two early Cambrian metamorphic events is suggested by zircon and monazite dating of a pegmatite at Willyabrup Cliffs. Two populations of zircon yield weighted mean ages of 542 ± 8 Ma (M1) and 521 ± 8 Ma (M2), whilst monazite data suggests a major population at *ca* 519 ± 5 Ma (M2) and a minor population at 538 ± 5 Ma (M1). The earlier metamorphic event is interpreted to be the crystallisation of a clinopyroxene-orthopyroxene-hornblende mafic granulite that is located structurally below the location of this sample. This age is analytically indistinguishable compared to the 540 ± 6 Ma age interpreted as the best estimate of the time of crystallisation of a monzogranite precursor to a hornblende-biotite dyke, north of Cowaramup Bay (Nelson, 1996). Therefore, *ca* 542 ± 8 Ma (zircon) and *ca* 538 ± 5 Ma (monazite) is interpreted to be the crystallisation age of the precursor to the garnet-orthopyroxene-hornblende-biotite amphibolite whose crystallisation age reflects peak metamorphism and *ca* 521 ± 8 Ma (zircon) and *ca* 519 ± 5 Ma (monazite).

Respective probability density plots for all monazite and zircon data (>85% concordant and omitting the *ca* 248 Ma monazite population) are presented with Figure 12 and reveal Gaussian populations for both sets of data. The normal distribution of data appears to reflect a single metamorphic event, where crystallisation occurred from ~550 to 480 Ma. A weighted mean of the 96 monazite data (>95% concordant) gives a $^{206}Pb/^{238}U$ age of 521 ± 3 Ma (MSWD = 6.5). Similarly, with the omission of older

zircon populations, the remaining 23 zircon ages define a Gaussian distribution over ~580 - 460 Ma, with a weighted mean age of 522 ± 5 Ma (MSWD = 2.2). By presenting data in this simplistic view, the complexity of data interpretation has been greatly reduced, as no attempt is made to identify different populations of monazite and zircon ages. However, it does reveal that there is a wide distribution of Early Cambrian monazite and zircon growth. Ages presented in this study, constrain peak metamorphism to ~503 - 527 Ma for the whole Leeuwin Complex, and are analytically indistinguishable to the respective weighted mean ages of 521 ± 3 Ma (for monazite) and 522 ± 5 Ma (for zircon). Therefore, granulite facies metamorphism for the Leeuwin Complex is constrained to *ca* 522 Ma.

11.4 *εNd evolution*

Epsilon Nd values for samples presented with the estimated igneous age of *ca* 750 Ma (Nelson, 1996; 2002; Collins, 2003) have slightly negative εNd values ranging from -0.48 to -2.65. The cluster of these values suggests that the *ca* 750 Ma emplacement of a suite of crustal melt A-type granitiods affected the whole Leeuwin Complex. However, samples RVLC034 & 035 from Cape Freycinet have respective εNd values of -6.75 and -11.03. These evolved εNd values imply that the precursors to the 1090 Ma protoliths are inherited from a much older crustal source. When plotted against the εNd evolution of felsic Yilgarn Crust (from Qlu *et al*, 1999), it seems reasonable that the crustal source may have been derived from the Archaean Yilgarn Craton.

Previous Sm-Nd data from a sample collected near Cape Leeuwin were presented by Fletcher and Libby (1993) that had a calculated εNd value of -12. This value is much more evolved than either of the samples from Sarge Bay and Skippy Rock that have respective εNd of -2.65 and -1.14. Either the sample from Fletcher and Libby (1993) is a product of the 1090 Ma protolith, or the sample has been generated from the remelting of an enriched crustal source.

Samples presented in Liu *et al,* 2007 (Grove Mountains) and Wareham *et al.* (1998) from eastern Antarctica have relatively similar εNd evolutions. Data from Wareham *et al*, 1998 reflect a very large range of εNd values at 1100-1150 Ma that reflect the

evolved εNd data of both Leeuwin Complex Protoliths. Similar comparisons can also be seen with the data from Liu *et al,* 2007. The relatively similar evolution of Nd-Sm isotopes within the rocks of the Leeuwin Complex and Eastern Antarctica suggest that they were inherited from a similar crustal source. This supports recent evidence that the Mesoproterozoic emplacement of the Naturaliste Plateau was a western continuation of the Albany-Fraser crust, and prior to opening of the Southern Rift System, may have been linked to the Mesoproterozoic belt now exposed in Wilkes Land, eastern Antarctica (Haplin *et al.* 2008). It seems reasonable to speculate that the evolved εNd values of the Leeuwin Complex and eastern Antarctica are attributed to the remelting of the Naturaliste Plateau Mesoproterozoic age crust.

12 Conclusions

The main findings from this study are:

- The deformation seen in the central domain of the Leeuwin Complex is structurally different to the deformation within the northern and southern domains (described by Collins, 2003 & Janssen *et al.* 2003). The four phases of deformation are interpreted to have occurred during or after peak metamorphism. The D1 fabric preserved within folded amphibolite layers is attributed to subvertical shortening. D3 folding is coaxial with the dominant (D2) S2 foliation and associated mineral elongation lineation that plunges shallowly to the east, which suggest that they were coeval, or that D3 is a continuation of D2, with subvertical contraction being the dominant stress vector. D3 kink folds are crosscut by diffuse, partial melt leucosomes that suggests that SW-NE compression occurred during, or post peak metamorphism, whilst D4 structures are interpreted to reflect late E-W extension (i.e. Janssen *et al.* 2003).

- The orthogneisses of the Leeuwin Complex preserve metamorphic mineral assemblages that reflect peak metamorphic conditions where T = 650 - 750°C and P = 6 - 8 kbar. Weighted mean averages from *P-T* estimates suggest that *ca* 687 ± 28°C and *ca* 7.24 ± 0.61 kbar peak metamorphic conditions were attained throughout the Leeuwin Complex.

- *P-T* estimations based on mineral rim compositions suggest that retrograde metamorphic conditions of $T = 638 \pm 20°C$ and $P = 6.3 \pm 0.56$ kbar, implying that the Leeuwin Complex remained at mid crustal (15 - 20km) levels after peak metamorphism.

- Chemical composition in garnet cores suggests that post-peak cooling was gradual at near isobaric conditions, whilst chemical zoning in garnet rims suggests that decompression occurred quickly, which is interpreted to be a response to rapid exhumation.

- SHRIMP zircon and LA-ICPMS monazite dating of numerous outcropping locations has constrained peak metamorphism to *ca* 522 ± 5 Ma (zircon) and 521 ± 3 Ma (monazite) for the whole Leeuwin Complex.

- An earlier metamorphic event has been identified at Willyabrup Cliffs, where a clinopyroxene-orthopyroxene-hornblende mafic gneiss is the precursor to the ~522Ma granite gneiss, as it is interpreted to have crystallised at *ca* 540 ± 6 Ma.

- The Leeuwin Complex has evolved εNd values that suggest that the felsic orthogneisses are inherited from an enriched crustal source and are similar to εNd values from eastern Antarctica. Recent Antarctica-Australia reconstructions (Whittaker *et al.* 2007) support the theory that the Naturaliste Plateau was a western continuation of the Albany Fraser crust. The moderately evolved εNd of the Leeuwin Complex and eastern Antarctica may be inherited from the crustal melting of the Mesoproterozoic protoliths of the Naturaliste Plateau.

13 Acknowledgements

First and foremost, I thank my supervisors, Martin Hand and Alan Collins for their guidance throughout the year and for their assistance and knowledge within the field. Many thanks must go to Christopher Clark of Curtin University, for his help in the field, assistance on the SHRIMP and financial contribution towards SHRIMP Pb-U

zircon age dating. I am also grateful to Benjamin Wade, Rachael Brick and Katherine Howard for their assistance in LA-ICPMS analyses and their patience in answering countless questions about the methodology and reduction of geochronological data. Thanks must go to Angus Netting and Peter Self for their technical expertise to and the staff of Adelaide Microscopy for their help and acceptance in coating samples at the last minute. Thanks must go to Honours students of 2008, especially David Tassone; for his help and good company, Ben McGee; as his absence from the honours room has meant less distractions and more desk space for myself, and Andrew Alesci; for being a OK bloke but an ordinary golfer. Dishonourable acknowledgements must be given to Kate Walsh and Daniela De Pretis for their irritating, high octane conversations and constant disruptions throughout the year!

14 References

BESLIER M. O., LE BIHAN T., FÉRAUD G. & GIRARDEAU J. 2001. Cretaceous ultra-slow spreading in the ocean–continent transition along the southwest Australian passive margin: constraints from 40Ar/39Ar dating. *In: European Union of Geosciences XI Abstract Volume*, p. 718. Cambridge Publications, Strasbourg.

BLACK L. P., SHERATON J. W., TINGEY R. J. & MCCULLOCH M. T. 1992. New U-Pb zircon ages from the Denman Glacier area, East Antarctica, and their significance for Gondwana reconstruction. *Antarctic Science* **4**, 447–460.

BORISSOVA I. 2002. Naturaliste Plateau, a continental fragment. *AUSGEO News* **67**, 14–16.

BROWN M. & PRESSLEY R. A., 1999. Crustal melting in nature: Prosecuting source processes. *Phys & Chem, Earth (A)* **24**, 3, 305-316.

BRUGUIER O., BOSCH D., PIDGEON R. T., BYRNE D. I. & HARRIS L. B. 1999. U-Pb chronology of the Northhampton Complex, Western Australia – evidence for Grenvillian sedimentation, metamorphism and deformation and geodynamic implications. *Journal of Mineral Petrology* **136**, 258-272

CAWOOD P. A. & NEMCHIN A. A. 2000. Provenance record of a rift basin: U/Pb ages of detrital zircons from the Perth Basin, Western Australia. *Sedimentary Geology* **134**, 209–234.

COLLINS A.S., 2003. Structure and age of the northern Leeuwin Complex, Western Australia: constraints from field mapping and U-Pb isotopic analysis. *Journal of Australian Earth Sciences*. 50, p. 585-599

COLLINS A. S. & FITZSIMONS I. C. W. 2001. Structural, isotopic and geochemical constraints on the evolution of the Leeuwin Complex, SW Australia. *In*: Sircombe K. N. & Li Z. X. eds. *From Basins to Mountains: Rodinia at the Turn of the Century*, pp. 16–19. Geological Society of Australia Abstracts **65**.

COLLINS A. S. & PISAREVSKY S. A., 2005. Amalgamating eastern Gondwana: The evolution of the Circum-Indian Orogens. Earth Science Reviews, **71**, 229-270

COLLINS A.S., REDDY S.M., BUCHAN C. & MRUMA A., In press. Temporal Constraints on Palaeoproterozoic eclogite formation and exhumation (Usagaran Orogen, Tanzania). *Journal of Earth and Planetary Science Letters.*

COMPSTON W. & ARRIENS P. A. 1968. The Precambrian geochronology of Australia. *Canadian Journal of Earth Science* **5**, 561–583.

COMPSTON W., WILLIAMS I. S., KIRSCHVINK J. L., ZHANG Z. & MA G. 1992. Zircon U–Pb ages for the Early Cambrian time scale. *Journal of the Geological Society of London* **149**, 171–184.

COMPSTON W., WILLIAMS I. S. & MEYER C. 1984. U–Pb geochronology of zircons from lunar breccia 73217 using a sensitive high mass resolution ion microprobe. *Journal of Geophysical Research* **89**, B525–B534.

DIREEN N.G., STAGG H.M.J., SYMONDS P.A. & COLWELL J.B., 2008. The architecture of volcanic rifted margins: New insights from the Exmouth-Gascoyne margin, Western Australia. *Australian Journal of Earth Sciences*, **55**, 325-347.
EGLINGTON B. M. 2006. Evolution of the Namaqua-Natal Belt, southern Africa – A geochronological and isotope geochemical review. *Journal of African Earth Sciences* **46**, 93-111

FITZSIMONS I. C. W. 1997. The Brattstrand Paragneiss and the Søstrene Orthogneiss: a review of Pan-African metamorphism and Grenvillian relics in Southern Prydz Bay. *In*: Ricci C. A. ed. *The Antarctic Region, Geological Evolution and Processes*, pp. 121–130. Terra Antarctica Publications, Siena.

FITZSIMONS I. C. W. 2000a. Grenville-age basement provinces in East Antarctica: evidence for three separate collisional orogens. *Geology* **28**, 879–882.

FITZSIMONS I. C. W. 2000b. A review of tectonic elements in the East Antarctic Shield, and their implications for Gondwana and earlier supercontinents. *Journal of African Earth Sciences* **31**, 3–23.

FITZSIMONS I. C. W. 2002. Comparison of detrital zircon ages in the Pinjarra Orogen (WA) and Maud province (Antarctica): evidence for collision of Western Australia with southern Africa at 1100 Ma. *Geological Society of Australia Abstracts* **67**, 228.

FITZSIMONS I. C. W. KINNY P. D. & HARLEY S. L. 1997. Two stages of zircon and monazite growth in anatectic leucogneiss: SHRIMP constraints on the duration and intensity of Pan-African metamorphism in Prydz Bay, East Antarctica. *Terra Nova* **9**, 47–51.

FITZSIMONS. I. C. W. 2003. Proterozoic basement provinces of southern and southwestern Australia, and their correlation with Antarctica. *In*: Yoshida M., Windley B. F. & Dasgupta S. eds. *Proterozoic East Gondwana: Supercontinent Assembly and Breakup*, pp. 93– 130. Geological Society of London Special Publication **206**.

FLETCHER I. R. & LIBBY W. G. 1993. Further isotopic evidence for the existence of two distinct terranes in the southern Pinjarra Orogen, Western Australia. *Geological Survey of Western Australia Report* **37**, 81–83.

FLETCHER I. R., WILDE S. A. & ROSMAN K. J. R. 1985. Sm-Nd model ages across the margins of the Archaean Yilgarn Block, Western Australia – III. The Western Margin. *Australian Journal of Earth Sciences* **32**, 73-82

GESSMANN C.K., SPIERING B. & RAITH M., 1997. Experimental study of the Fe-Mg exchange between garnet and biotite: Constraints on the mixing behaviour and

analysis of the cation-exchange mechanisms. *American Mineralogist*, Volume **82**, 1225-1240.

HAPLIN J. A., CRAWFORD A. J., DIREEN N. G., COFFIN M. F., FORBES C. J. & BORISSOVA I. 2008. Naturaliste Plateau, offshore Western Australia: A submarine window into Gondwana assembly and breakup. *The Geological Society of America.* **36**; no 10; 807-810.

HARRIS L. B. 1994. Neoproterozoic sinistral displacement along the Darling Mobile Belt, Western Australia, during Gondwanaland assembly. *Journal of the Geological Society of London* **151**, 901–904.

HARRIS L. B. & BEESON J. 1993. Gondwanaland significance of Lower Palaeozoic deformation in central India and SW Western Australia. *Journal of the Geological Society of London* **150**, 811–814.

HARRIS L. B. & LI Z. X. 1995. Paleomagnetic dating and tectonic significance of dolerite intrusions in the Albany Mobile Belt, Western Australia. *Earth and Planetary Science Letters* **131**, 143–164.

HENSEN B. J. & ZHAO B. 1995. A Pan-African granulite facies metamorphic episode in Prydz Bay, Antarctica: evidence from Sm–Nd garnet dating. *Australian Journal of Earth Sciences* **42**, 249–258.

HENSEN B. J. & ZHOU B. 1997. East Gondwana amalgamation by Pan- African collision? Evidence from Prydz Bay, East Antarctica. *In*: Ricci C. A. ed. *The Antarctic Region: Geological Evolution and Processes*, pp. 115–119. Terra Antarctica Publications, Siena.

HOLLAND T. J. P. & POWELL R. 1998. An internally consistent thermodynamic data set for phases of petrological interest. *Journal of Metamorphic Geology*, **13**, 309-343.

HOPGOOD A. M. & BOWES D. R. 1995. Matching Gondwanaland fragments: the significance of granitoid veins and tectonic structures in the Cape Leeuwin – Cape Naturaliste terrane, SW Australia. *Journal of Southeast Asian Earth Sciences* **11**, 253–263.

HOSKIN P. W. O. & BLACK L. P. 2000. Metamorphic zircon formation by solid-state recrystallisation of protolith igneous grains. *Journal of Metamorphic Geology* **18**, 423–439.

JANSSEN D. P. COLLINS A. S. & FITZSIMONS I. C. W. 2003. Structure and tectonics of the Leeuwin Complex and Darling Fault Zone, southern Pinjarra Orogen, Western Australia—a field guide.
Geological Survey of Western Australia Record **2003/15**.

KAY J. G. 1958. The high grade metamorphics of Cape Naturaliste, Western Australia. BSc (Hons) thesis, University of Western Australia, Perth (unpubl.).

KELSEY D. E., WADE B. P., COLLINS A. S., HAND M., SEALING C.R. & NETTING A. 2008. Discovery of a Neoproterozoic basin in the Prydz belt in East Antarctica and its implications for Gondwana assembly and ultrahigh temperature metamorphism. *Precambrian Research*, **161**, 355-388.

LEAKE B. E., WOOLLEY A. R., ARPS C. E. S., BIRCH W. D., GILBERT M.C., GRICE J. D., HAWTHORNE F. C., KATO A., KRIVOVICHEV V. G., LINTHOUT K., LAIRD J., MANDARINO J. A., MARESCH W. V., NICKEL E. H., ROCK N. M. S., SCHUMACHER J. C., STEPHENSON N. C. N., UNGARETTI L., WHITTAKER E. J. W. & YOUZHI, G. 1997. Nomenclature of Amphiboles: Report of the Subcommittee on Amphibole of the International Mineralogical Association, Commission on New Minerals and Mineral Names. *The Canadian Mineralogist*, **35**, 219-246.

LIBBY W. G. De LAETER J. R. & ARMSTRONG R. A. 1999. Proterozoic biotite Rb-Sr dates in the northwestern part of the Yilgarn Craton, Western Australia. *Australian Journal of Earth Sciences.* **46**, 851-860

LIBBY W. G. & De LAETER J. R. 1998. Biotite Rb-Sr age evidence for Early Palaeozoic tectonism along the cratonic margin in southwestern Australia. *Australian Journal of Earth Sciences.* **45**, 623-632.

LOWRY D. C. 1967. Busselton and Augusta, WA. *Geological Survey of Western Australia 1:250 000 Geological Series Explanatory Notes*.

MCCULLOCH M. T. 1987. Sm–Nd Isotopic Constraints on the Evolution of Precambrian Crust in the Australian Continent. *In*: Kröner A. eds. *Proterozoic Lithospheric Evolution*, pp. 115–130. American Geophysical Union Geodynamics Series **17**.

McDOUGALL I. & HARRISON T.M., 1999. Geochronology and Thermochronology by the $^{40}Ar/^{39}Ar$ method: *New York, Oxford University Press*, 288.

MEERT J. G. & VAN DER VOO R. 1997. The assembly of Gondwana 800– 550 Ma. *Journal of Geodynamics* **23**, 223–235.

MOYES A. B. & GROENEWALD P.B. 1996. Isotopic constraints on Pan-African Metamorphism in Dronning Maud Land, Antarctica. *Chemical Geology* **129**, 247-256.

MYERS J. S. 1990a. Albany–Fraser. *Geology and Mineral Resources of Western Australia*, pp. 255–263. Geological Survey of Western

MYERS J. S. 1990b. Anorthosite in the Leeuwin complex of the Pinjarra Orogen, Western Australia. *Australian Journal of Earth Sciences* **37**, 241–245.

MYERS J. S. 1990c. Pinjarra Orogen. *Geology and Mineral Resources of Western Australia*, pp. 265–274. Geological Survey of Western Australia Memoir **3**.

MYERS J. S. 1994. Late Proterozoic high-grade gneiss complex between Cape Leeuwin and Cape Naturaliste. *Geological Society of*

Australia, Western Australian Division, Excursion Guidebook **6**.

NELSON D. R. 1995. *Field Guide to the Leeuwin Complex*. Geological Survey of Western Australia, Perth.

NELSON D. R. 1996. Compilation of SHRIMP U–Pb zircon geochronology data, 1995. *Geological Survey of Western Australia Record* **1996/5.**

NELSON D. R. 1997. Compilation of SHRIMP U–Pb zircon geochronology data, 1996. *Geological Survey of Western Australia Record* **1997/2**.

NELSON D. R. 1999. Compilation of SHRIMP U–Pb zircon geochronology data, 1998. *Geological Survey of Western Australia Record* **1999/2**.

NELSON D. R. 2002. Compilation of Geochronological Data, 2001. *Geological Survey of Western Australia Record* **2002/2**.

NELSON D. R. 2005. 112131: hornblende granite gneiss, Cape Leeuwin; 112132: hornblende granite gneiss, Cape Leeuwin; 112134: granite gneiss, Cosy Corner; 112140: biotite-hornblende monzogranite dyke, Gracetown; 112143: hornblende-biotite monzogranite dyke, Cowaramup Bay north; 112144A: horneblende monzogranite gneiss, Canal Rocks north. *Western Australia Geological Survey*: Geochronology dataset **604**; in compilation of geochronology data, June 2006.

O'BRIEN P. J. 1997. Garnet zoning and reaction textures in overprinted eclogites, Bohemian Massif, European Variscides: A record of their thermal history during exhumation. *Lithos* **41**, 119-133.

PAYNE J. L., HAND M., BAROVICH K. M. & WADE B. P. 2008. Temporal constraints on the timing of high-grade metamorphism in the northern Gawler Craton: implications for assembly of the Australian Proterozoic. *Australian Journal of Earth Sciences* **55,** 623-640.

PEERS R. 1975. The Geology of Western Australia. *Geological Survey of Western Australia*. Memoir 2.

REID J. A., PAYNE J. L. & WADE B. P. 2006. A new geochronological capability for South Australia: U-Pb zircon dating via LA-ICPMS. *MESA Journal* **42,** 27-31.

PISAREVSKY S. A. WINGATE M. T. D. & POWELL C. MCA, JOHNSON S. & EVANS D. A. D. 2003. Models of Rodinia assembly and fragmentation. *In*: Yoshida M., Windley B. & Dasgupta S. eds. *Proterozoic East Gondwana: Supercontinent Assembly and Breakup*, pp 35–55. Geological Society of London Special Publication **206**.

POWELL C. MCA. & PISAREVSKY S. A. 2002. Late Neoproterozoic assembly of East Gondwana. *Geology* **30**, 3–6.

RUBATTO D. & GEBAUER D. 2000. Use of cathodoluminescence for U–Pb zircon dating by ion microprobe: some examples from the western Alps. *In*: Pagel M.,

Barbin V., Blanc P. & Ohnenstetter D. eds. *Cathodoluminescence in Geosciences*, pp. 373–400. Springer- Verlag, Berlin.

SAINT-SMITH E. C. 1912. A geological reconnaissance of a portion of the South-West Division of Western Australia. *Geological Survey of Western Australia Bulletin* **40**, 38–69.

SIRCOMBE K. & FREEMAN M. J. 1999. Provenance of detrital zircons on the Western Australia coastline—implications for the geologic history of the Perth basin and denudation of the Yilgarn. *Geology* **27**, 879–882.

WADE B. P., HAND M., MAIDMENT D. W., CLOSE D. F. & SCRIMGEOUR I.R., 2008. Origin of metasedimentary and igneous rocks from the Entia Dome, eastern Arunta region, central Australia: a U-Pb LA-ICPMS, SHPIMP and Sm-Nd isotope study. *Australian Journal of Earth Sciences* **55,** 703-719.

WAREHAM C. D. PANKHURST R. J. THOMAS R. J. STOREY B. C. GRANTHAM G. H. JACOBS J. & EGLINTON B. M. 1998. Pb Nd and Sr Isotope mapping of Grenville-age crustal provinces in Rodinia. *The Journal of Geology* **106,** 647-659.

WILDE S. A. 1999. Evolution of the western margin of Australia during the Rodinian and Gondwanan supercontinent cycles. *Gondwana Research* **2**, 481–499.

WILDE S. A. & MURPHY D. M. K. 1990. The nature and origin of the Late Proterozoic high-grade gneisses of the Leeuwin Block, Western Australia. *Precambrian Research* **47**, 251–270.

WILDE S. A. & NELSON D. R. 2001. Geology of the western Yilgarn Craton and Leeuwin Complex, Western Australia—a field guide. *Geological Survey of Western Australia Record* **2001/15**.

WINGATE M. T. D. & EVANS D. A. D. 2003. Palaeomagnetic constraints on the Proterozoic tectonic evolution of Australia. *In*: Yoshida M.,

WINGATE M. T. D. & GIDDINGS J. W. 1999. Paleomagnetic test of the Australia–Laurentia connection at 755 Ma. *In: European Union of Geosciences X Abstract Volume*, p. 121. Cambridge Publications, Strasbourg.

ZHU X.K. & O'NIONS R.K., 1999. Zonation of monazite in metamorphic rocks and its implications for high temperature thermochronology; a case stude from the Lewisian terrain. *Earth Planetary Sciences*. 171 (2), 209-220.

15 Figure Captions

Figure 1. Reconstruction of Gondwana from Fitzsimons (2003) modified by Collins (2003) illustrates the significance of the Leeuwin Complex within the Neoproterozoic – Cambrian Pinjarra Orogen. The grey region highlights the regions subject to late Neoproterozoic to Early Cambrian orogenesis. NP, Naturaliste Plateau. Other Pinjarra Inliers: MC, Mullingara Complex; NC North Hampton Complex; RC, Rayner Complex.

Figure 2. Locations of samples used within this study. Inset, the approximate boundaries between the three structurally different domains of the Leeuwin Complex are identified and named. Regions of the central domain that have been mapped in detail are highlighted by blue boxes, and are presented in Figure 3.

Figure 3. Regional-scale structural maps of selected locations within the central domain of the Leeuwin Complex. Structural data are presented on stereonets (lower hemisphere equal-area projections). (a) Honeycombs. (i) Structural data reveals a consistent shallowly dipping easterly foliation with a mineral lineation that plunges down-dip to the foliation, with a minor divergence to the ESE. Folds hinges are parallel to the local lineation. (b) Willyabrup Cliffs (ii) All poles to foliation reveal a east-south-east dipping foliation with a variable mineral lineation. The mineral lineation varies in orientation from north-east to south-east, whilst the majority of fold hinges are axial planar to the foliation, one fold hinge plunges SES which is oblique to the foliation and main mineral lineation. (c) North of Cowaramup Bay. (iii) Poles to foliation reflect the flat lying foliation gently dipping to the SE. The mineral lineation plots down-dip to the foliation. One mineral lineation plots to the NE which is oblique to the foliation. The contact between the mafic dyke and the granitic gneiss show that the mafic dyke crosscuts the foliation at a steeper angle, trending to the east. (d) Redgate Beach (iv) Poles to foliation plot in a well confined cluster that reflects the shallow dipping easterly foliation. Mineral lineation readings trend to the ENE which is slightly oblique to the principal foliation. A single fold hinge trends to the SE which does not reflect the axial planar relationship displayed at other locations. (e) Cape Freycinet (v) Poles to foliation are well clustered reflecting the dominant ESE dipping

foliation. Fold hinges are parallel to the mineral lineation which is slightly oblique to the foliation, tending NE.

Figure 4. Isoclinal folding of amphibolite layer during D2 deformation, located at Honeycomb Cliffs, centred at: E114°59'39.1" S39°46'40.0". (a) A detailed field sketch of the isoclinal fold which is axial planar to the easterly dipping S2 foliation and the fold hinge is parallel to the down-dipping lineation. Traces of the initial S1 fabric are preserved within the hinge of the fold that have been deformed by D2 and are crosscut by the dominant S2 foliation. Inset, Schematic diagrams (1) Detailing the formation of the initial S1 fabric, that overprints the amphibole layer. (2) Prolonged crustal compression leads to isoclinal folding of the amphibolite that is oblique to the principal stress orientation, subsequently folding the layer, along with the S1 fabric. (3) The S2 foliation overprints the folded amphibolite while the S1 fabric remains preserved within the fold hinge. (b) Compiled field photographs of the fold within the cliff face (please note; the photographs are slightly distorted due to the angle at which the photographs were taken. Photographs were taken looking due east). A 100mm compass is used as a scale which is located within the fold hinge.

Figure 5. Field photographs from the central Leeuwin Complex that highlight specific deformation structures. A 100mm field compass in used as a scale in photographs, where the compass in not present, a scale is given. (a) S1 foliation fabric preserved within the fold hinge (F1) of the amphibolite layer presented in Figure 4, Honeycomb Cliffs. Inset, large garnet porphyroblasts located within the fold hinge - photo taken looking east. (b) An isolated lens of D3, S-type folds of the S2 fabric that are encapsulated by the easterly dipping S2 foliation. The lens is highlighted by the black line and the inset photo clearly displays the S-type nature of the folds. The fold hinges of these folds are parallel to the gently ENE plunging mineral lineation. Photograph is taken looking east. Located at Round Rocks, Cape Freycinet (Figure 2). (c) Garnet bearing leucosome that has been isoclinally folded (F3) during D3 deformation. The fold is located within the region of low strain that is presented in figure 6 (Inset 2). Photograph is taken looking northwest at Honeycombs (refer to Figure 2). (d) Strain partitioning across an amphibolite layer. The relatively undeformed central region contains deep-red garnet porphyroblasts and the gentle easterly dipping foliation is fickle. Strain has partitioned to the boundaries of the amphiolite that are in contact

with the garnet absent granitic gneiss. Hornblende-biotite-plagioclase coronae increase in intensity towards the gneiss and eventually completely replace garnet grains. Photograph is taken at Willyabrup Cliffs looking east. (e) Late stage K-feldspar pegmatite vein that has distinct boundaries with the gneiss when compared to the nebulitic pegmatites attributed to D3. The easterly plunging vein is a product of D4, east-west extension – photo taken and Honeycomb Cliffs, looking west. (f) Crosscutting contact boundary between the pyroxene-hornblende-biotite mafic and the massive granite gneiss, north of Cowaramup Bay. The ill-defined foliation dips shallowly to the east, as does the crosscutting contact boundary. Photograph is taken looking northeast.

Figure 6. Kink folds within garnet bearing leucocratic granite gneiss, produced by (σ^2) NE-SW compression. (a) Schematic diagram illustrating the ill-defined boundaries of leucosomes within a 'kink' fold set, where diffuse, nebulitic pegmatites form within the hinge zones. Biotite selvages form on leucosome boundaries. (b) Photograph of structure, taken looking ESE at Honeycombs. (c) Poles to planes of conjugate kink folds at honeycombs. The dominant kink fold orientation is to the ENE, implying WSW-ENE compression. (d) Poles to planes of conjugate kink folds at Willyabrup Cliffs. The dominant kink fold orientation is ~E, implying E-W compression.

Figure 7. Detailed outcrop map illustrating the partitioning of high strain within foliation parallel amphibolite layers. In such layers the foliation is exacerbated and is brittle. Plagioclase rich pegmatites are elongate and parallel to the foliation within the amphibolite layers, whilst crosscutting pegmatites participate towards the low strain regions where they accumulate within the boudin necks and fold hinges of leucosomes. Many leucosomes feed into the diffuse nebulitic pegmatites; a key indication of partial melting. Insets: (1) Elongate, parallel to foliation pegmatite veins within a high strain, amphibolite layer. (2) Isoclinally folded leucosome illustrated in Figure 5c. (3) Poorly defined σ shaped pegmatites within a high strain amphibolite layer, an unreliable kinematic indication of E-W shearing.

Figure 8. Photomicrographs that illustrate key petrological characteristics. All photomicrographs are in plane polarised light except for (a) which is taken in cross polarised light. (a) Granoblastic mosaic mineral assemblage of the granitic gneiss at Skippy Rock (Figure 2). Mineral grains are equidimensional, with rounded >0.6mm garnet grains surrounded by plagioclase and euhedral K-feldspar phenocrysts. Sparse biotite grains are aligned in an orientation that defines the local foliation that dips steeply to the east. Sample RVLC007. Width of view is 3 mm. (b) Accessory titanite strongly associated metamorphic hornblende porphyroblasts. Relic garnet porphyroclast is replaced by metamorphic plagioclase and K-feldspar. Sample RVLC008, Sarge Bay. Width of view is 5mm. (c) Garnet porphyroclast enveloped by elongate, well aligned biotite. Line A-B is the transect line analysed and presented in Figure 9. Sample RVLC045, Willyabrup Cliffs. Width of view is 13mm. (d) Metamorphic orthopyroxene enveloped by elongate biotite that defines the foliation, within a matrix of plagioclase and hornblende. Sample RVLC052 Willyabrup Cliffs. Width of view 4mm. (e) Garnet grain enveloped by a coronae of plagioclase and hornblende. Ilmenite and magnetite are in abundance where amphiboles are the dominant mineral assemblage. Sample RVLC077, Honeycombs. Width of view 4mm. (f) Disseminated garnet that contains plagioclase and oxide inclusions. Garnet is isolated by abundant plagioclase and K-feldspar. Minor biotite occurs on garnet boundaries. Sample RVLC084, Sugarloaf. Width of view is 5mm.

Figure 9. Chemical zoning of a single garnet porphyroblast. A transect of microprobe analyses were preformed across the garnet profile (Figure 8c). Microprobe analyses were spaced at 33μm at the garnet rim and 250μm across the core. The transect reveals considerable changes in end-member composition towards the garnet rims. Where: X_{Fe} (Fe/Fe+Ca+Mg+Mn) is almandine; X_{Ca} (Ca/Ca+Fe+Mg+Mn) is grossular; X_{Mg} (Mg/Mg+Fe+Ca+Mn) is pyrope and X_{Mn} (Mn/Mn+Fe+Ca+Mg) is spessartine.

Figure 10. Simplified map of the Leeuwin Complex, that identifies the three structural domains and shows the location of samples selected for thermobarometry and their associated *P-T* estimates for peak and retrograde metamorphism. *P-T* calculations presented in this figure are identified in Table 4. The *P-T* estimates of

the three structural domains are determined form weighted mean calculations from these highlighted *P-T* estimates for reasons mentioned within the text.

Figure 11. Diagrammatic representation of selected *P-T* estimates that reveal Gaussian distributions for *P-T* estimates from all localities suggests uniform metamorphic conditions across the Leeuwin Complex. (1a & 2a) Probability density plot for selected peak and retrograde average *T* estimates from all locations. (1b & 2b) Weighted averages of selected peak and retrograde average *T* estimates from all locations. (1c & 2c) Probability density plot for selected peak and retrograde average *P* estimates from all locations. (1d & 2d) Weighted averages of selected peak and retrograde average *P* estimates from all locations.

Figure 12. Simplified map of the Leeuwin Complex, showing the locations of samples used for geochronology and their corresponding $^{206}Pb/^{238}U$ ages. Ages of previously published data are also presented at their given locations. (*) Represents ages that are interpreted to date the granite crystallisation age. Inset (i) Probability density plot for all monazite data >85% concordant, with the exclusion of the ~248 Ma population from sample RVLC070. (ii) Probability density plot for all zircon data presented. The dominant populations are interpreted as representing peak metamorphism.

Figure 13. Diagrammatic representations of LA-ICPMS monazite data from sample RVLC003. (a) Concordia plot for all monazite analyses from this sample (n=21). Inset, $^{206}Pb/^{238}U$ weighted average of the 10 most concordant analyses. (b) Probability density plot of $^{206}Pb/^{238}U$ ages that reveals separate populations of monazite. (c) $^{206}Pb/^{238}U$ weighted average of all monazite data, assuming data reflects a single population of monazite (n=18). All $^{206}Pb/^{238}U$ ages are quoted with ± 1 sigma and red error ellipses imply that data have been excluded from weighted mean averages.

Figure 14. Diagrammatic representations of LA-ICPMS monazite data from sample RVLC020. (a) Concordia plot for all monazite analyses from this sample (n=15). Inset, Probability density plot of $^{206}Pb/^{238}U$ ages that reveals separate populations of monazite. (b) Tera-Wasserburg Concordia plot demonstrates the effect of common lead on data concordance. (c) $^{206}Pb/^{238}U$ weighted average of monazite data, assuming

data reflects a single population of monazite (n=7). All $^{206}Pb/^{238}U$ ages are quoted with ± 1 sigma and red error ellipses imply that data have been excluded from weighted mean averages.

Figure 15. Diagrammatic representations of LA-ICPMS monazite data from sample RVLC025. (a) Concordia plot for all monazite analyses from this sample (n=20). (b) Probability density plot of $^{206}Pb/^{238}U$ ages that reveals two separate populations of monazite. (c) $^{206}Pb/^{238}U$ weighted average of all monazite data, assuming data reflects a single population of monazite (n=19). All $^{206}Pb/^{238}U$ ages are quoted with ± 1 sigma and red error ellipses imply that data have been excluded from weighted mean averages.

Figure 16. Diagrammatic representations of LA-ICPMS monazite data from sample RVLC046. (a) Concordia plot for all monazite analyses from this sample (n=19). Inset, Probability density plot of $^{206}Pb/^{238}U$ ages a relatively Gaussian, normal distribution of monazite ages that is interpreted to represent a single population. (b) Tera-Wasserburg concordia plot reveals a concordant population, with common lead having a negligible effect on data concordance. (c) $^{206}Pb/^{238}U$ weighted average of monazite data, assuming data reflects a single population of monazite (n=18). All $^{206}Pb/^{238}U$ ages are quoted with ± 1 sigma and red error ellipses imply that data have been excluded from weighted mean averages.

Figure 17. Diagrammatic representations of LA-ICPMS monazite data from sample RVLC070. (a) Concordia plot for all monazite analyses from this sample (n=22) with a discordia line that intercepts at 0 Ma. (b) Probability density plot of $^{206}Pb/^{238}U$ ages that reveals two separate populations of monazite. (c) $^{206}Pb/^{238}U$ weighted average of all monazite data, assuming data reflects a single population of monazite (n=11). All $^{206}Pb/^{238}U$ ages are quoted with ± 1 sigma and red error ellipses imply that data have been excluded from weighted mean averages.

Figure 18. Diagrammatic representations of LA-ICPMS monazite data from sample RVLC080. (a) Concordia plot for all monazite analyses from this sample (n=20). (b) Probability density plot of $^{206}Pb/^{238}U$ ages that reveals a single Gaussian population of monazite. (c) $^{206}Pb/^{238}U$ weighted average of all monazite data, assuming data reflects

a single population of monazite (n=18). All $^{206}Pb/^{238}U$ ages are quoted with ± 1 sigma and red error ellipses imply that data have been excluded from weighted mean averages.

Figure 19. Diagrammatic representations of SHRIMP zircon rim analyses from sample RVLC034. (a) Concordia plot for all zircon data from this sample (n=12). Inset, Probability density plot of $^{206}Pb/^{238}U$ ages that reveals two unique populations of zircon growth. (b) Concordia plot and concordia age of Early Cambrian zircon growth (n=7) (c) $^{206}Pb/^{238}U$ weighted average of all zircon data >90% concordant, assuming data reflects a single population of zircon growth (n=7). All $^{206}Pb/^{238}U$ ages are quoted with ± 1 sigma and red error ellipses imply that data have been excluded from concordia age and weighted mean average calculations.

Figure 20. Diagrammatic representations of SHRIMP zircon rim analyses from sample RVLC035. (a) Concordia plot for all zircon data from this sample (n=12). Inset, Probability density plot of $^{206}Pb/^{238}U$ ages that reveals three unique populations of zircon growth. (b) Concordia plot and concordia age of Early Cambrian zircon growth (n=7) (c) $^{206}Pb/^{238}U$ weighted average of all zircon data >90% concordant, assuming data reflects a single population of zircon growth (n=7). All $^{206}Pb/^{238}U$ ages are quoted with ± 1 sigma and red error ellipses imply that data have been excluded from concordia age and weighted mean average calculations.

Figure 21. Diagrammatic representations of SHRIMP zircon rim analyses from sample RVLC041. (a) Concordia plot for all zircon data from this sample (n=9). (b) Probability density plot of $^{206}Pb/^{238}U$ ages that reveals two unique populations of zircon growth (c) $^{206}Pb/^{238}U$ weighted average of all zircon data >90% concordant, assuming data reflects a single population of zircon growth (n=7). All $^{206}Pb/^{238}U$ ages are quoted with ± 1 sigma and red error ellipses imply that data have been excluded from weighted mean average calculations.

Figure 22. Epsilon Nd plot (Nd-Sm data in Table 5). εNd evolved values have been plotted at the two apparent protolith ages (from Nelson, 1996; 1999; Collins, 2003) 1090 Ma (for Redgate Beach and Cape Freycinet samples) and protolith age of 750

Ma (for all remaining samples) εNd data from east Antarctica and Natal, Southern Africa (see text for references).

Figure 23. Structural models based on field observations within the central domain of the Leeuwin Complex, where structural observation has been used to model the orientation of strain from deformation structures. (a) Pure shear (coaxial) model, showing the development of rotational strain, with its resulting linear and planar fabric elements. (b) Simple shear (non-coaxial) model, showing the development of rotational strain, with its resulting linear and planar fabric elements. (c) Strain configuration of the finite strain ellipsoid in response to both pure and simple shear, where the orientation strain ellipsoid is identical for both models.

Table 1. Summary of the previously described deformation structures for the northern and southern domains of the Leeuwin Complex. Deformation within the northern domain is based the descriptions of Collins (2003) and the southern domain is a summary of Janssen *et al* (2003).

Domain	D1 Structures	D2 Structures	D3 Structures	D4 Structures
Northern	Gneissic foliation (S1) that is wrapped around (D2) Nauturliste Antiform, foliation is axial planar to D1 isoclinal folds. D1 strain reflects a low vorticity number and dominated by pure-shear shortening	Tight, asymmetric, parasitic Z-folds. Fold hinges plunge (NW-NE) parallel to the D1/D2 mineral lineration. D2 strain is coaxial with D1 strain, dominated by pure-shear E-W shortening.	ENE-WSW trending D3 folding resultant from a late NNW-SSE contractional deformation phase	Open undulatory folding of the S1 foliation along the NE facing coast attributed to a late NW-SE contractional phase
Southern	D1 gneissic foliation, axial planar to F1 isoclinal folds that are north trending, upright to inclined folds that gently plunge and axial planes that steeply dip to the east. Sub-horizontal SE dipping lineation defined by biotite.	F2 tight to isoclinal folds that deform the S1 foliation. F2 is coaxial to F1, implying that F2 is a continuation of D1	Open warping, trending WNW, with a wavelength of ~10km. Defined by the undulation of the L1 mineral lineation	Near vertical E-trending brittle faults with minor centimetre scale offset.

Table 2. Petrology and mineral assemblages for the samples selected for Electron Microprobe Analysis and average P-T calculations

Sample	Location	Sample Lithology	Mineral Assemblage	Petrological Description
RVLC007	Skippy rock 3	granitic gneiss containing abundant kf, quartz biotite and small, but abundant garnet	Garnet-biotite-spinel-plagioclase-K-feldspar-quartz	Garnet porphyroblasts (1-5mm) contain plagioclase inclusions and biotite intrusions.
RVLC008	Sarge Bay 4	Foliated Garnet - hornblende bearing gneiss with biotite, quartz and plagioclase defining migmatite layering	Garnet-hornblende-biotite-titanite-illmenite-clinopyroxene-plagioclase-K-feldspar-quartz	Plagioclase coronae isolate garnet porphyroblasts (1-10mm). Titanite and ilmenite occur within hornblende accumulates which are rimmed by biotite
RVLC009	Sarge Bay 4	Foliated Garnet - hornblende bearing gneiss with biotite, quartz and plagioclase defining migmatite layering	Garnet-hornblende-clinopyroxene-plagioclase-illmenite-K-feldspar-quartz	Plagioclase coronae isolate relic garnets (1-3mm) and clinopyroxene clasts. Garnets contain ilmenite inclusions.
RVLC018	Cosey Corner 7	Hornblende, biotite, quartz and sparse garnet. Taken from remanent mafic dykes	Garnet-hornblende-biotite-plagioclase-epidote-ilmenite-quartz	Large (20-40mm) garnet porphyroblasts with plagioclase coronae and hornblende intrusions. Ilmenite occurs within hornblende grains and epidote is isolated by plagioclase
RVLC027	Merchant Rock 9	Remanent mafic intrusion, with garnet decompression textures	Garnet-hornblende-biotite-plagioclase-epidote-ilmenite-quartz	Relic garnet porphyroblasts (1-3mm) are consumed by plagioclase and hornblende. Ilmenite occur within hornblende and biotite accumulates
RVLC045	Willyabrup 14	Mafic containing biotite, hornblende and garnet	Garnet-biotite-plagioclase-quartz.	Garnet porphyroblasts (10-20mm) contain biotite and plagioclase intrusions. Elongate biotite grains define laminar flow textures.
RVLC051	Willyabrup 16	Biotite, garnet mafic, with minor coronas of plagioclase around garnet	Garnet-hornblende-orthopyroxene-biotite-plagioclase- ilmenite-quartz	Decompressed garnet porphyroblasts (5-25mm), consumed by plagioclase and biotite coronae. Garnets contain inclusions of plagioclase and ilmenite.
RVLC052	Willyabrup 16	Mafic, remanent garnet, dominated by plagioclase & biotite reaction textures	Garnet-hornblende-orthopyroxene-biotite-plagioclase-illmenite-quartz	Decompressed garnet porphyroblasts (10-30mm) with well defined plagioclase, biotite and hornblende coronae. Garnets contain ilmenite, plagioclase and hornblende inclusions
RVLC059	Gracetown 18	High grade, gneiss contains subhorizontal foliations garnet, biotite & plagioclase and crystalline K-feldspar	Garnet-biotite-plagioclase-K-feldspar-quartz.	Elongate garnet porphyroblasts (5-25mm) contain ilmenite, biotite and plagioclase inclusions. Garnets are isolated by a plagioclase, K-feldspar, quartz matrix
RVLC063	Honeycomb 19	Remanent amphibolite layer containing garnet, hornblende & biotite	Garnet-hornblende-biotite-K-feldspar-quartz	Garnet porphyroblasts (10-30mm) with plagioclase inclusions. Garnets are isolated by hornblende, plagioclase and biotite coronae.
RVLC077	Honeycomb 22	Remanent amphibolite: garnet reaction textures defined by plagioclase	Garnet-hornblende-biotite-plagioclase-spinel-ilmenite-quartz	Small garnet (<1mm) relics are almost completely consumed by plagioclase. Garnet porphyroblasts (10-25mm) are isolated by plagioclase coronae. Spinel, ilmenite and plagioclase occur as inclusions within hornblende.
RVLC080	Canal Rocks 24	Foliated gneiss bearing garnet-biotite melanosomes and K-feldspar-garnet leucosomes	Garnet-biotite-plagioclase-K-feldspar-spinel-ilmenite-quartz.	Garnet porphyroblasts (2-10mm) contain biotite and magnetite inclusions and plagioclase intrusions.
RVLC084	Sugarloaf 25	sample from large meter scale boulders - bt-gt migmatitic gneiss	Garnet-biotite-plagioclase-ilmenite-quartz	Garnet porphyroblasts (1-8mm) contain plagioclase inclusions. Biotite and ilmenite are sparsely dispersed throughout
RVLC092	Bunker Bay 32	Garnet-hornblende bearing felsic gneiss	Garnet-hornblende-plagioclase-K-feldspar-magnetite-ilmenite	Few garnet porphyroblasts (1-5mm) are well preserved with well rounded boundaries in contact with plagioclase, K-feldspar, ilmenite and quartz.

Table 3. Summary of mineral chemistry for all petrological analyses

	Skippy Rock	Sarge Bay	Sarge Bay	Cosy Corner	Cape Freycine	Willyabrup Cliffs				Gracetown	Honeycombs		Sugarloaf	Bunker Bay
	RVLC007	RVLC008	RVLC009	RVLC018	RVLC027	RVLC045		RVLC051	RVLC052	RVLC059	RVLC063	RVLC077	RVLC084	RVLC092
Garnet						Core	Rim							
X_{Fe}	0.69 - 0.70	0.530 - 0.574	0.48 - 0.54	0.50 - 0.54	0.59 - 0.63	0.62 - 0.68	0.66 - 0.74	0.54 - 0.59	0.55 - 0.60	0.78 - 0.82	0.61 - 0.66	0.66 - 0.72	0.50 - 0.63	0.67 - 0.69
X_{Mn}	0.067 - 0.090	0.046 - 0.078	0.03 - 0.12	0.09 - 0.18	0.05 - 0.09	0.038 - 0.048	0.051 - 0.069	0.031 - 0.039	0.029 - 0.037	0.03 - 0.039	0.047 - 0.086	0.03 - 0.08	0.01 - 0.14	0.08 - 0.09
X_{Mg}	0.039 - 0.054	0.03 - 0.04	0.058 - 0.081	0.04 - 0.05	0.08 - 0.12	0.23 - 0.26	0.14 - 0.23	0.24 - 0.28	0.22 - 0.27	0.03 - 0.057	0.06 - 0.07	0.06 - 0.08	0.18 - 0.29	0.05 - 0.055
X_{Ca}	0.16 - 0.2	0.32 - 0.38	0.29 - 0.39	0.27 - 0.35	0.19 - 0.22	0.051 - 0.088	0.048 - 0.053	0.10 - 0.13	0.13 - 0.14	0.11 - 0.12	0.19 - 0.26	0.16 - 0.19	0.04 - 0.19	0.17 - 0.19
Biotite														
X_{Ti}	0.05 - 0.072	-	-	0.042	0.05 - 0.07	0.047 - 0.05		0.04 - 0.05	0.048 - 0.053	0.046 - 0.067	0.05 - 0.07	0.06 - 0.07	0.04 - 0.06	-
X_{Fe}	0.41 - 0.47	-	-	0.43 - 0.45	0.34 - 0.36	0.29 - 0.33		0.18 - 0.25	0.21 - 0.25	0.44 - 0.47	0.39 - 0.45	0.40 - 0.44	0.23 - 0.29	-
X_{Mg}	0.13 - 0.19	-	-	0.299 - 0.309	0.42 - 0.44	0.27 - 0.31		0.58 - 0.70	0.58 - 0.64	0.21 - 0.24	0.27 - 0.37	0.32 - 0.34	0.52 - 0.62	-
X_{Na}	0.0077 - 0.032	-	-	0.011 - 0.035	0.007 - 0.028	0.046 - 0.052		0.07 - 0.11	0.09 - 0.11	0.01 - 0.04	0.009 - 0.026	0.02 - 0.05	0.01 - 0.02	-
Hornblende														
X_{Fe}	-	0.820 - 0.825	0.66 - 0.72	0.68 - 0.70	0.55 - 0.60	-		0.37 - 0.41	0.37 - 0.41	-	0.55 - 0.71	0.7 - 0.73	-	0.79 - 0.81
X_{Mg}	-	0.21 - 0.29	0.28 - 0.33	0.29 - 0.32	0.39 - 0.45	-		0.58 - 0.62	0.59 - 0.62	-	0.29 - 0.44	0.26 - 0.28	-	0.18 - 0.20
Ortho-pyroxene														
X_{Ca}	-	-	-	-	-	-		0.0065 - 0.010	0.007 - 0.010	-	-	-	-	-
X_{Fe}	-	-	-	-	-	-		0.39 - 0.43	0.40 - 0.43	-	-	-	-	-
X_{Mg}	-	-	-	-	-	-		0.53 - 0.54	0.53 - 0.55	-	-	-	-	-
Clino-pyroxene														
X_{Ca}	-	0.46 - 0.48	0.45 - 0.47	-	-	-		-	-	-	-	-	-	-
X_{Fe}	-	0.39 - 0.43	0.24 - 0.26	-	-	-		-	-	-	-	-	-	-
X_{Mg}	-	0.32 - 0.39	0.22 - 0.24	-	-	-		-	-	-	-	-	-	-
Plagioclase														
X_{Ab}	0.59 -0.66	0.42 - 0.51	0.38 - 0.49	0.51 - 0.64	0.24 - 0.52	0.67 - 0.685		0.45 - 0.56	0.49 - 0.56	0.64 - 0.78	0.59 - 0.67	0.59 - 0.65	0.70 - 0.72	0.66 - 0.72
X_{Na}	0.58 - 0.65	0.36 - 0.54	0.38 - 0.48	0.50 - 0.62	0.24 - 0.51	0.669 - 0.690		0.45 - 0.55	0.49 - 0.56	0.64 - 0.77	0.58 - 0.66	0.58 - 0.64	0.69 - 0.71	0.54 - 0.60
X_{Ca}	0.33 - 0.40	0.35 - 47	0.50 - 0.60	0.35 - 0.48	0.47 - 0.76	0.31 - 0.33		0.44 - 0.55	0.43 - 0.50	0.21 - 0.35	0.32 - 0.39	0.34 - 0.40	0.26 - 0.27	0.20 - 0.28
X_{K}	0.009 - 0.02	0.010 - 0.017	0.012 - 0.018	0.009 - 0.019	0.003 - 0.009	0.007 - 0.01		0.001 - 0.005	0.001 - 0.005	0.008 - 0.012	0.01 - 0.02	0.009 - 0.019	0.02 - 0.03	0.008 - 0.02
K-Feldspar														
X_{Ab}	-	-	-	0.13 - 0.17	0.08 - 0.25	-		-	-	0.09 - 0.12	0.11 - 0.13	-	-	0.1 - 0.2
Illmenite														
X_{Mn}	-	0.041 - 0.043	0.033 - 0.036	0.67 - 0.69	0.66 - 0.67	-		0.67 - 0.68	0.67 - 0.68	0.67 - 0.68	0.64 - 0.68	0.67 - 0.68	0.68 - 0.69	0.68
X_{Ihm}	-	0.88 - 0.93	0.90- 0.94	0.89 - 0.97	0.6 - 0.1	-		0.8 - 0.1	0.80 - 0.93	0.90- 0.94	0.88 - 0.93	0.82 - 0.96	0.9 - 0.55	0.088
X_{Ti}	-	0.510 - 0.512	0.50 - 0.69	0.51 - 0.52	0.50 - 0.51	-		0.51 - 0.512	0.51 - 0.52	0.51 - 0.52	0.50 - 0.51	0.50 - 0.51	0.52 - 0.53	0.51
Magnetite														
X_{Fe3}	0.62 - 0.66	-	-	-	0.51 - 0.63	-		-	-	-	-	0.63 - 0.66	0.50 - 0.58	0.62 - 0.64
X_{Fe2}	0.33 - 0.35	-	-	-	0.37 - 0.41	-		-	-	-	-	0.33 - 0.35	0.32 - 0.35	0.31 - 0.34
X_{Al}	0.007 - 0.028	-	-	-	0.002 - 0.020	-		-	-	-	-	0.006 - 0.022	0.08 - 0.12	0.007 - 0.014

Table 4. Average P-T calculations using the internally consistant software THERMOCALC. Where activities have been omitted from calculations they are crossed out. Fe-Mg exchange thermometers have been used where applicable.

Location	Sample	Analysis	Activities	Average P T Calculations T°C ± 1σ	P (kbar) ± 1σ	correl	Sigfit	aH2O (best fit)	Average Temperature Ave T°C ± 1σ	Average Pressure Ave P (kbar) ± 1σ	Fe-Mg exchange Thermometry gt-bt T(°C)±1σ	gt-hbd T(°C)±1σ	gt-cpx T(°C)±1σ	gt-opx T(°C)±1σ
Skippy Rock	RVLC007	core	py gr alm spss an ab mt usp phl ann east	672 ± 172	8.2 ± 4.2	0.886	0.41	excluded	664 ± 71	8.2 ± 1.97	665 ± 124			
Skippy Rock	RVLC007	rim	phl ann east py gr alm spss an ab mt usp	630 ± 127	6.2 ± 127	0.783	0.47	excluded	638 ± 73	6.6 ± 1.86	832 ± 181			
Sarge Bay	RVLC008	core	py gr alm spss andr an ab san ilm hem pnt di hed cats tr fact ts parg sph	691 ± 71	7.4 ± 0.9	0.675	0.79	0.1	681 ± 45	7.5 ± 0.68		779 ± 159	729 ± 148	
				815 ± 91	9.0 ± 1.1	0.746	0.76	0.5	690 ± 53	7.9 ± 0.67				
Sarge Bay	RVLC008	rim	py gr alm spss andr an ab san ab ilm hem pnt di hed cats tr fact ts parg sph	676 ± 71	6.9 ± 0.9	0.645	0.78	0.1	669 ± 47	7.1 ± 0.69		675 ± 133	621 ± 122	
				772 ± 85	8.2 ± 1.0	0.705	0.96	0.5	777 ± 45	7.5 ± 0.68				
Sarge Bay	RVLC009	core	di hed an ab tr fact ts parg py gr alm spss ilm hem pnt geik	704 ± 64	8.2 ± 1.2	0.593	1.17	0.1	688 ± 48	8.4 ± 0.94		902 ± 142	874 ± 165	
				881 ± 78	11.0 ± 1.4	0.683	0.92	0.5	829 ± 49	10 ± 0.94				
Sarge Bay	RVLC009	rim	di hed an ab tr fact ts parg py gr alm spss ilm hem pnt geik	653 ± 50	5.9 ± 0.9	0.309	0.76	0.1	653 ± 45	6.1 ± 0.91		686 ± 100	642 ± 115	
				783 ± 65	7.8 ± 1.1	0.389	0.99	0.5	753 ± 57	7.7 ± 0.97				
Cosy Corner	RVLC018	core	an ab ~~cz~~ san py gr alm spss andr ilm ~~hem~~ pnt geik phl ann east tr fact parg mt	676 ± 111	5.8 ± 1.6	0.691	0.95	excluded	606 ± 78	6.0 ± 1.18	800 ± 165	611 ± 89		
				599 ± 42	6.2 ± 0.8	0.085	0.96	0.5	606 ± 44	5.1 ± 0.87				
Cosy Corner	RVLC018	rim	an ab ~~cz~~ san py gr alm spss andr ilm ~~hem~~ pnt geik phl ann east tr fact parg mt	544 ± 82	4.6 ± 1.4	0.705	1.07	excluded	538 ± 54	5.6 ± 1.01	720 ± 144	576 ± 86		
				586 ± 42	5.2 ± 0.8	0.03	1	0.5	565 ± 41	5.5 ± 0.9				
Cape Freycinet	RVLC027	core	phl ann east tr fact ts parg an ab py gr alm spss andr ilm ~~hem~~ pnt	752 ± 111	6.5 ± 1.9	0.711	1.04	excluded	724 ± 68	6.4 ± 1.3	927 ± 179	710 ± 96		
				806 ± 98	7.6 ± 1.5	0.577	1	0.5	770 ± 71	7.3 ± 1.2				
Cape Freycinet	RVLC027	rim	phl ann east tr fact ts parg an ab py gr alm spss andr ilm ~~hem~~ pnt	688 ± 95	6.2 ± 1.7	0.767	0.77	excluded	688 ± 55	6.4 ± 1.14	804 ± 133	676 ± 91		
				733 ± 76	7.1 ± 1.4	0.591	0.75	0.5	719 ± 47	7.0 ± 1.13				
Wilyabrup	RVLC045	core	py gr alm spss phl ann east an ab					excluded	1020 ± 122	11.2 ± 2.41	1067 ± 191			
								0.5	1021 ± 119	11.2 ± 2.41				
Wilyabrup	RVLC045	rim	py gr alm spss phl ann east an ab					excluded	1000 ± 112	11.2 ± 2.41	602 ± 96			
								0.5	589 ± 73	4.1 ± 1.76				
Wilyabrup	RVLC051	core	en fs an ab phl ann east py gr alm spss ilm hem pnt geik tr fact ts parg gl	628 ± 76	6.6 ± 1.4	0.678	1.18	excluded	604 ± 52	6.5 ± 0.99	778 ± 126	689 ± 384		693 ± 154
				669 ± 49	7.0 ± 1.3	0.615	1.14	0.5	659 ± 35	6.9 ± 0.98				
Wilyabrup	RVLC051	rim	en fs an ab phl ann east py gr alm spss ilm hem pnt geik tr fact ts parg gl	617 ± 64	6.1 ± 1.3	0.629	1.22	excluded	608 ± 47	6.2 ± 1.03	840 ± 133	764 ± 98		764 ± 160
				645 ± 38	6.3 ± 1.2	0.754	1.18	0.5	652 ± 22	6.4 ± 1.02				
Wilyabrup	RVLC052	core	py gr alm spss mt usp ilm hem pnt geik tr fact ts parg gl phl ann east an ab en fs mgts	678 ± 70	7.1 ± 1.3	0.675	1.13	excluded	656 ± 48	7.0 ± 0.9	924 ± 155	761 ± 97		760 ± 176
				733 ± 46	7.5 ± 1.3	0.732	1.13	0.5	723 ± 30	7.3 ± 0.83				
Wilyabrup	RVLC052	rim	py gr alm spss mt usp ilm hem pnt geik tr fact ts parg gl phl ann east an ab en fs mgts	634 ± 68	6.3 ± 1.4	0.644	1.121	excluded	620 ± 49	6.1 ± 0.98	856 ± 145	758 ± 98		764 ± 169
				639 ± 36	6.3 ± 1.3	0.77	1.15	0.5	635 ± 17	6.1 ± 0.68				
Gracetown	RVLC059	core	py gr alm spss phl ann east san an ab ilm hem pnt	779 ± 177	6.8 ± 3.8	0.804	0.11	excluded	775 ± 85	6.8 ± 2.3	781 ± 162			
				736 ± 79	5.9 ± 1.2	-0.156	0.22	0.5	736 ± 67	5.9 ± 1.2				
Gracetown	RVLC059	rim	py gr alm spss phl ann east san an ab ilm hem pnt	590 ± 40	6.5 ± 0.9	-0.606	0.29	excluded	620 ± 28	6.3 ± 1.54	544 ± 100			
				658 ± 48	8.0 ± 0.9	-0.461	0.55	0.5	657 ± 34	8.1 ± 0.82				
Honeycomb	RVLC063	core	san tr fact ts parg an ab ilm hem pnt py gr alm spss phl ann ~~east~~	540 ± 53	6.3 ± 0.8	0.172	0.85	0.25	532 ± 53	6.3 ± 0.79	880 ± 182	687 ± 100		
				618 ± 64	7.6 ± 0.9	0.279	0.94	0.5	619 ± 66	7.6 ± 0.83				
Honeycomb	RVLC063	rim	san tr fact ts parg an ab ilm hem pnt py gr alm spss phl ann ~~east~~	613 ± 50	5.5 ± 0.9	-0.054	1.01	0.25	600 ± 46	5.5 ± 0.89	862 ± 29	656 ± 17		
				682 ± 60	6.8 ± 1.0	0.034	0.93	0.5	668 ± 51	6.8 ± 0.95				
Honeycombs	RVLC077	core	an ab tr fact ts parg gl phl ann east py gr alm spss andr mt ilm ~~hem~~ pnt geik	748 ± 94	6.4 ± 1.5	0.546	0.81	0.25	732 ± 48	6.2 ± 1.35	806 ± 156	697 ± 99		
				779 ± 99	7.1 ± 1.6	0.572	0.89	0.5	733 ± 60	6.3 ± 1.23				
Honeycombs	RVLC077	rim	an ab tr fact ts parg gl phl ann east py gr alm spss andr mt ilm ~~hem~~ pnt geik	654 ± 80	5.5 ± 1	0.425	0.46	0.25	631 ± 66	5.5 ± 0.95	712 ± 134	647 ± 92		
				677 ± 84	6.2 ± 1.1	0.481	0.54	0.5	666 ± 65	6.2 ± 0.97				
Sugarloaf	RVLC084	core	py gr alm spss phl ann east an ab ilm ~~hem~~ pnt geik	773 ± 169	5.5 ± 3.5	0.66	1.26	excluded	721 ± 94	5.2 ± 2.04	779 ± 135			
				773 ± 169	5.5 ± 3.5	0.66	1.26	0.5	721 ± 94	5.9 ± 2.12				
Sugarloaf	RVLC084	rim	py gr alm spss phl ann east an ab ilm ~~hem~~ pnt ~~geik~~	599 ± 116	4.0 ± 2.6	0.612	1.18	excluded	626 ± 74	4.1 ± 1.76	610 ± 93			
				599 ± 116	4.0 ± 2.6	0.612	1.18	0.5	602 ± 119	4.4 ± 1.8				
Bunker Bay	RVLC092	core	san ab py gr alm spss andr tr fact parg gl mt usp ilm hem pnt an ab	581 ± 236	4.7 ± 1.9	0.853	0.44	0.1	718 ± 121	5.8 ± 1.17		692 ± 132		
				733 ± 416	7.5 ± 4	0.957	0.54	0.5	615 ± 99	6.9 ± 1.09				
Bunker Bay	RVLC092	rim	san ab py gr alm spss andr tr fact parg gl mt usp ilm hem pnt an ab	490 ± 162	3.7 ± 1.3	0.726	0.45	0.1	561 ± 134	4.7 ± 1.06		707 ± 130		
				566 ± 206	5.4 ± 1.8	0.852	0.65	0.5	612 ± 106	6.0 ± 1.01				

Table 5. Samples selected for geochronology, for sample locations refer to Figure 2.

Sample	Location	Location GDA 94, MGA (zone 50) Easting	Northing	Analytical Method	Lithology
RVLC001	Skippy Rock	327497	6196838	Sm-Nd	Pegmatite Feldspar-plagioclase-qartz-biotite-garnet
RVLC003	Skippy Rock	327497	6196838	LA-ICPMS - monazite	Crystalline Pegmatite - Feldspar-plagioclase-quartz-magnetite-garnet
RVLC012	Sarge Bay	329564	6195422	Sm-Nd	Plagioclase-magnetite-titanite-horneblende-cpx-garnet gneiss
RVLC020	Cosey Corner	318233	6207627	LA-ICPMS - monazite, Sm-Nd	Feldspar-plagioclase-biotite-horneblende-garnet gneiss
RVLC025	Round Rocks	315243	6226158	LA-ICPMS - monazite	Feldspar-plagioclase-magnetite-biotite-horneblende-garnet gneiss
RVLC034	Merchant Rock	315018	6225745	SHRIMP - zircon, Sm-Nd	Feldspar-plagioclase-magnetite-biotite-horneblende-garnet gneiss
RVLC035	Redgate Beach	315298	6231812	SHRIMP - zircon, Sm-Nd	Crystalline Pegmatite - Feldspar-quartz-biotie-garnet
RVLC041	Wilyabrup Cliffs	314799	6258208	SHRIMP - zircon, Sm-Nd	Crystalline Pegmatite - Plagioclase-quartz-biotite-horneblende
RVLC070	Honeycombs (North)	314244	6260807	LA-ICPMS - monazite, Sm-Nd	Crystalline Pegmatite - Feldspar-plagioclase-quartz-magnetite-biotite-garnet
RVLC083	Honeycombs (South)	314264	6260761	LA-ICPMS - monazite	Feldspar-plagioclase-biotite-garnet gneiss
RVLC080	Canal Rocks	314241	6260751	Sm-Nd	Feldspar-quartz-plagioclase-magnetite-monazite-biotie-garnet gneiss

Table 6. *LAPCIMS U-Pb isotopic data of* monazites from selected rock samples

Sample	Spot No.	$^{207}Pb/^{235}U$	1σ	$^{206}Pb/^{238}U$	1σ	rho	$^{206}Pb/^{238}U$ Age	1σ	$^{207}Pb/^{235}U$ Age	1σ	Concordancy
RVLC003	1.1	0.70865	0.00583	0.08425	0.00056	0.81	521.4	3.36	543.9	3.47	104
	2.1	0.67	0.0053	0.08266	0.00055	0.84	512	3.28	520.7	3.22	102
	3.1	0.68818	0.00486	0.08226	0.00054	0.93	509.6	3.21	531.7	2.92	104
	4.1	0.68218	0.00504	0.0883	0.00058	0.89	545.5	3.46	528.1	3.04	97
	5.1	0.68503	0.00578	0.08903	0.00061	0.81	549.8	3.59	529.8	3.48	96
	6.1	0.67367	0.00579	0.08261	0.00057	0.80	511.7	3.38	522.9	3.51	102
	7.1	0.67391	0.00561	0.08843	0.0006	0.82	546.3	3.58	523.1	3.4	96
	8.1	0.67843	0.00533	0.08511	0.00058	0.87	526.6	3.44	525.8	3.23	100
	9.1	0.67457	0.00563	0.08219	0.00057	0.83	509.2	3.38	523.5	3.41	103
	10.1	0.69782	0.00546	0.08515	0.00058	0.87	526.8	3.47	537.5	3.27	102
	11.1	0.71783	0.00646	0.08736	0.00063	0.80	539.9	3.73	549.4	3.82	102
	12.1	0.69014	0.00487	0.08646	0.0006	0.98	534.6	3.54	532.9	2.93	100
	13.1	0.69432	0.00489	0.08641	0.00059	0.97	534.3	3.53	535.4	2.93	100
	14.1	0.69265	0.00504	0.08689	0.0006	0.95	537.1	3.58	534.4	3.02	99
	15.1	0.69487	0.00519	0.08685	0.00061	0.94	536.9	3.6	535.7	3.11	100
	16.1	0.67153	0.00485	0.0839	0.00058	0.96	519.3	3.46	521.6	2.95	100
	17.1	0.679	0.00484	0.08535	0.00059	0.97	528	3.51	526.2	2.93	100
	18.1	0.69873	0.00584	0.08633	0.00062	0.86	533.8	3.66	538	3.49	101
	19.1	0.67133	0.00473	0.08351	0.00058	0.99	517	3.44	521.5	2.87	101
	20.1	0.6899	0.0059	0.08455	0.00061	0.84	523.2	3.61	532.7	3.55	102
	21.1	0.69891	0.00499	0.08696	0.0006	0.97	537.5	3.59	538.1	2.98	100
RVLC020	1.1	0.64946	0.00557	0.08025	0.00056	0.81	497.6	3.35	508.1	3.43	102
	2.1	0.63534	0.00459	0.08067	0.00055	0.94	500.1	3.25	499.4	2.85	100
	3.1	0.64288	0.00457	0.08047	0.00054	0.94	499	3.22	504.1	2.83	101
	4.1	0.63394	0.00447	0.07936	0.00053	0.95	492.3	3.18	498.5	2.78	101
	5.1	0.62549	0.00503	0.07772	0.00053	0.85	482.5	3.16	493.3	3.14	102
	6.1	0.62605	0.00453	0.07844	0.00053	0.93	486.8	3.15	493.6	2.83	101
	7.1	0.65578	0.00458	0.08109	0.00054	0.95	502.6	3.23	512	2.81	102
	8.1	0.62424	0.00463	0.07817	0.00052	0.90	485.2	3.14	492.5	2.9	102
	9.1	0.68539	0.00607	0.08675	0.00065	0.85	536.3	3.84	530	3.65	99
	10.1	0.57939	0.00659	0.07269	0.00053	0.64	452.3	3.2	464.1	4.23	103
	11.1	0.72811	0.00617	0.09528	0.00069	0.85	586.7	4.09	555.4	3.62	95
	12.1	0.66693	0.00453	0.08382	0.00056	0.98	518.9	3.33	518.8	2.76	100
	13.1	0.64919	0.00478	0.08098	0.00056	0.94	502	3.33	508	2.94	101
	14.1	0.64645	0.00478	0.08272	0.00058	0.95	512.3	3.46	506.3	2.95	99
	15.1	0.62578	0.00476	0.07936	0.00053	0.88	492.3	3.17	493.5	2.97	100

Table 6 cont.

Sample	Spot No.	$^{207}Pb/^{235}U$	1σ	$^{206}Pb/^{238}U$	1σ	rho	$^{206}Pb/^{238}U$ Age	1σ	$^{207}Pb/^{235}U$ Age	1σ	Concordancy
RVLC025	1.1	0.66477	0.00444	0.08337	0.00052	0.93	516.2	3.1	517.5	2.71	100
	2.1	0.68265	0.0047	0.08532	0.00054	0.92	527.8	3.19	528.4	2.83	100
	3.1	0.66985	0.00463	0.08466	0.00053	0.91	523.9	3.16	520.6	2.81	99
	4.1	0.36044	0.00263	0.04477	0.00028	0.86	282.3	1.75	312.5	1.96	111
	5.1	0.67557	0.00468	0.08448	0.00053	0.91	522.8	3.17	524.1	2.83	100
	6.1	0.68305	0.00616	0.08574	0.00057	0.74	530.3	3.39	528.6	3.72	100
	7.1	0.70938	0.00461	0.08727	0.00055	0.97	539.4	3.24	544.4	2.74	101
	8.1	0.68629	0.00483	0.08573	0.00054	0.89	530.2	3.23	530.6	2.91	100
	9.1	0.69047	0.00449	0.0858	0.00054	0.97	530.6	3.19	533.1	2.7	100
	10.1	0.69525	0.00517	0.08613	0.00056	0.87	532.6	3.3	536	3.1	101
	11.1	0.69142	0.00467	0.0862	0.00055	0.94	533	3.24	533.7	2.8	100
	12.1	0.69072	0.00548	0.08487	0.00055	0.82	525.1	3.27	533.2	3.29	102
	13.1	0.67526	0.00481	0.08435	0.00054	0.90	522.1	3.21	523.9	2.92	100
	14.1	0.66501	0.00461	0.08312	0.00053	0.92	514.7	3.16	517.7	2.81	101
	15.1	0.60774	0.0061	0.07727	0.00053	0.68	479.8	3.18	482.1	3.85	100
	16.1	0.69502	0.00515	0.08616	0.00056	0.88	532.8	3.3	535.8	3.09	101
	17.1	0.68516	0.00477	0.08506	0.00054	0.91	526.2	3.23	529.9	2.88	101
	18.1	0.67066	0.00487	0.08392	0.00054	0.89	519.5	3.22	521.1	2.96	100
	19.1	0.68433	0.00477	0.08495	0.00054	0.91	525.6	3.22	529.4	2.88	101
	20.1	0.66935	0.00541	0.08315	0.00055	0.82	514.9	3.25	520.3	3.29	101
RVLC046	1.1	0.6459	0.00986	0.08502	0.00122	0.94	526	7.27	506	6.08	96
	2.1	0.66173	0.00909	0.08693	0.00123	0.97	537.3	7.31	515.7	5.55	96
	3.1	0.66807	0.00944	0.08791	0.00125	0.99	543.2	7.42	519.5	5.75	96
	4.1	0.71006	0.01	0.08372	0.00116	0.98	518.3	6.9	544.8	5.94	105
	5.1	0.64968	0.00905	0.08378	0.00116	0.99	518.6	6.93	508.3	5.57	98
	6.1	0.66464	0.00922	0.08491	0.00118	1.00	525.4	7.01	517.4	5.62	98
	7.1	0.65815	0.00959	0.08344	0.00117	0.96	516.6	6.95	513.5	5.87	99
	8.1	0.66621	0.00937	0.08452	0.00118	0.99	523	7.02	518.4	5.71	99
	9.1	0.68096	0.00925	0.08702	0.0012	0.99	537.9	7.12	527.4	5.59	98
	10.1	0.66716	0.00894	0.08293	0.00119	0.93	513.6	7.11	519	5.45	101
	11.1	0.67891	0.0092	0.08373	0.00121	0.94	518.3	7.22	526.1	5.57	102
	12.1	0.64389	0.00895	0.07896	0.00112	0.98	489.9	6.68	504.7	5.53	103
	13.1	0.66628	0.00902	0.08339	0.0012	0.94	516.3	7.15	518.4	5.5	100
	14.1	0.69904	0.00937	0.08347	0.00119	0.94	516.8	7.09	538.2	5.6	104
	15.1	0.66135	0.00881	0.08268	0.00117	0.94	512.1	6.99	515.4	5.38	101
	16.1	0.67676	0.00913	0.08312	0.00119	0.94	514.7	7.07	524.8	5.53	102
	17.1	0.63393	0.00914	0.08145	0.00111	0.95	504.8	6.64	498.5	5.68	99
	18.1	0.65967	0.00887	0.0821	0.00117	0.94	508.6	6.96	514.4	5.43	101
	19.1	0.65751	0.00886	0.08184	0.00117	0.94	507.1	6.95	513.1	5.43	101

Table 6 cont.

Sample	Spot No.	$^{207}Pb/^{235}U$	1σ	$^{206}Pb/^{238}U$	1σ	rho	$^{206}Pb/^{238}U$ Age	1σ	$^{207}Pb/^{235}U$ Age	1σ	Concordancy
RVLC070	1.1	0.68219	0.00507	0.08581	0.00054	0.85	530.7	3.21	528.1	3.06	100
	2.1	0.67741	0.00625	0.08396	0.00054	0.70	519.7	3.23	525.2	3.78	101
	3.1	0.30925	0.00357	0.03913	0.00026	0.58	247.5	1.61	273.6	2.77	111
	4.1	0.6798	0.00533	0.08557	0.00054	0.80	529.3	3.22	526.7	3.22	100
	5.1	0.30587	0.00287	0.03853	0.00025	0.69	243.7	1.55	271	2.23	111
	6.1	0.30605	0.00298	0.03901	0.00025	0.66	246.7	1.57	271.1	2.32	110
	7.1	0.31623	0.00331	0.03955	0.00026	0.63	250	1.61	279	2.55	112
	8.1	0.68755	0.00528	0.08657	0.00055	0.83	535.2	3.25	531.3	3.17	99
	9.1	0.3031	0.00341	0.03852	0.00026	0.60	243.7	1.58	268.8	2.66	110
	10.1	0.66418	0.00495	0.08422	0.00053	0.84	521.3	3.16	517.2	3.02	99
	11.1	0.30478	0.00405	0.03947	0.00027	0.51	249.6	1.66	270.1	3.15	108
	12.1	0.66575	0.00862	0.08227	0.00056	0.53	509.7	3.36	518.1	5.26	102
	13.1	0.66186	0.00633	0.08198	0.00054	0.69	507.9	3.23	515.8	3.87	102
	14.1	0.68971	0.00626	0.08188	0.00054	0.73	507.3	3.19	532.6	3.76	105
	15.1	0.69213	0.00544	0.08151	0.00052	0.81	505.2	3.12	534.1	3.26	106
	16.1	0.682	0.00517	0.08452	0.00054	0.84	523.1	3.22	528	3.12	101
	17.1	0.67748	0.00559	0.08568	0.00056	0.79	529.9	3.31	525.3	3.38	99
	18.1	0.6905	0.00523	0.08484	0.00054	0.84	524.9	3.23	533.1	3.14	102
	19.1	0.69478	0.0056	0.08602	0.00056	0.81	531.9	3.3	535.7	3.36	101
	20.1	0.6854	0.00622	0.08424	0.00055	0.72	521.4	3.29	530	3.75	102
	21.1	0.69349	0.00615	0.07997	0.00053	0.75	496	3.16	534.9	3.69	108
	22.1	0.68095	0.00527	0.0853	0.00055	0.83	527.7	3.29	527.4	3.18	100
RVLC083	1.1	0.66873	0.00866	0.08394	0.00108	0.99	519.6	6.41	519.9	5.27	100
	2.1	0.67394	0.00876	0.0847	0.00109	0.99	524.1	6.48	523.1	5.31	100
	3.1	0.69684	0.00925	0.08559	0.00111	0.98	529.4	6.59	536.9	5.54	101
	4.1	0.66963	0.00873	0.08394	0.00108	0.99	519.6	6.43	520.5	5.31	100
	5.1	0.77169	0.01003	0.08596	0.00111	0.99	531.6	6.57	580.7	5.75	109
	6.1	0.66141	0.00854	0.08286	0.00107	1.00	513.2	6.35	515.5	5.22	100
	7.1	0.67799	0.00882	0.08446	0.00109	0.99	522.7	6.48	525.6	5.34	101
	8.1	0.66113	0.00866	0.08306	0.00107	0.98	514.4	6.35	515.3	5.29	100
	9.1	0.6411	0.00823	0.08127	0.00105	0.99	503.7	6.24	503	5.09	100
	10.1	0.69493	0.00925	0.08438	0.0011	0.98	522.2	6.52	535.8	5.54	103
	11.1	0.67467	0.00891	0.08522	0.00111	0.99	527.2	6.59	523.6	5.4	99
	12.1	0.67663	0.00895	0.08485	0.00111	0.99	525	6.58	524.7	5.42	100
	13.1	0.68657	0.00913	0.08603	0.00113	0.99	532	6.68	530.7	5.49	100
	14.1	0.64632	0.00851	0.08168	0.00107	0.99	506.2	6.38	506.2	5.25	100
	15.1	0.64936	0.00849	0.08307	0.00109	1.00	514.4	6.49	508.1	5.23	99
	16.1	0.65402	0.00854	0.08229	0.00108	0.99	509.8	6.44	510.9	5.25	100
	17.1	0.68548	0.00909	0.0855	0.00113	1.00	528.9	6.69	530.1	5.47	100
	18.1	0.67675	0.00904	0.08627	0.00114	0.99	533.4	6.77	524.8	5.47	98
	19.1	0.6773	0.00897	0.08471	0.00112	1.00	524.2	6.66	525.1	5.43	100
	20.1	0.69324	0.00948	0.08766	0.00117	0.98	541.7	6.94	534.7	5.69	99

Table 7. SHRIMP Pb-U isotopic data of zircon analyses from selected samples

Spot No.	% common 206	ppmU	ppmTh	$^{232}Th/^{238}U$	$^{207}Pb/^{206}U$		$^{207}Pb/^{235}U$		$^{206}Pb/^{238}U$		error correction	$^{206}Pb/^{238}U$		$^{207}Pb/^{206}Pb$		% Discordant
34-1.1	6.18	1353	248	0.189	0.069	± .0027	0.711	± 0.030	0.075	± 0.001	0.398	464	± 8	902	± 81	94
34-2.1	1.56	1099	185	0.174	0.059	± .0017	0.671	± 0.023	0.082	± 0.001	0.475	510	± 8	570	± 64	12
34-3.1	5.32	1348	184	0.141	0.066	± .0039	0.751	± 0.045	0.082	± 0.001	0.269	509	± 8	818	± 121	61
34-4.1	1.08	1133	148	0.135	0.057	± .0017	0.671	± 0.023	0.085	± 0.001	0.471	524	± 8	511	± 66	-2
34-5.1	1.59	1068	282	0.273	0.057	± .0016	0.654	± 0.021	0.083	± 0.001	0.498	513	± 8	498	± 61	-3
34-6.1	2.83	1336	167	0.129	0.062	± .0021	0.676	± 0.026	0.079	± 0.001	0.420	491	± 8	673	± 74	37
34-7.1	1.08	995	241	0.250	0.059	± .0014	0.742	± 0.022	0.092	± 0.002	0.566	566	± 9	554	± 53	-2
34-8.1	0.56	1088	151	0.143	0.058	± .0011	0.682	± 0.017	0.085	± 0.001	0.655	528	± 8	529	± 41	0
34-10.1	8.35	1377	205	0.154	0.079	± .0033	0.818	± 0.036	0.075	± 0.001	0.363	466	± 7	1173	± 82	152
34-11.1	1.00	671	109	0.168	0.077	± .0010	1.942	± 0.046	0.183	± 0.004	0.817	1084	± 19	1119	± 27	3
34-12.1	0.74	1081	137	0.131	0.057	± .0010	0.664	± 0.016	0.085	± 0.001	0.671	526	± 8	480	± 39	-9
34-13.1	1.39	994	131	0.136	0.057	± .0019	0.676	± 0.025	0.085	± 0.001	0.441	527	± 8	511	± 72	-3
35-1.1	1.74	956	310	0.335	0.058	± .0022	0.665	± 0.028	0.083	± .0014	0.388	516	± 8	524	± 85	2
35-2.1	0.86	990	251	0.262	0.077	± .0018	1.803	± 0.053	0.170	± .0028	0.570	1015	± 16	1114	± 48	10
35-3.1	3.10	773	185	0.247	0.058	± .0023	0.682	± 0.029	0.085	± .0014	0.383	526	± 8	539	± 86	3
35-4.1	1.05	1447	356	0.254	0.059	± .0012	0.688	± 0.017	0.084	± .0013	0.634	522	± 8	574	± 42	10
35-5.1	4.04	937	302	0.333	0.067	± .0022	0.743	± 0.028	0.080	± .0013	0.448	498	± 8	840	± 70	69
35-6.1	0.59	1598	73	0.047	0.059	± .0011	0.753	± 0.019	0.093	± .0015	0.659	573	± 9	557	± 41	-3
35-7.1	1.34	1203	199	0.171	0.056	± .0016	0.648	± 0.021	0.083	± .0013	0.503	515	± 8	472	± 61	-8
35-8.1	1.42	1378	338	0.253	0.058	± .0017	0.669	± 0.022	0.083	± .0013	0.479	513	± 8	548	± 64	7
35-9.1	1.99	1248	790	0.654	0.059	± .0030	0.699	± 0.038	0.085	± .0014	0.299	529	± 8	580	± 111	10
35-10.1	1.76	626	159	0.263	0.068	± .0024	1.185	± 0.058	0.127	± .0043	0.688	770	± 25	861	± 74	12
35-11.1	1.68	770	175	0.235	0.070	± .0023	1.219	± 0.049	0.126	± .0029	0.581	764	± 17	937	± 67	23
35-12.1	0.99	1570	123	0.081	0.057	± .0014	0.653	± 0.019	0.083	± .0013	0.556	515	± 8	489	± 52	-5
41-1.1	0.71	1010	90	0.092	0.060	± .0013	0.686	± 0.018	0.083	± .0013	0.598	511.8	± 7.9	612	± 47	10
41-2.1	1.74	521	105	0.208	0.053	± .0021	0.613	± 0.026	0.083	± .0014	0.392	515.3	± 8.1	347	± 87	-33
41-3.1	0.39	1330	54	0.042	0.057	± .0007	0.692	± 0.014	0.088	± .0014	0.799	543.3	± 8.3	496	± 26	-9
41-4.1	1.65	911	153	0.174	0.057	± .0018	0.663	± 0.024	0.084	± .0014	0.455	518.8	± 8.1	507	± 70	-2
41-5.1	1.27	809	41	0.052	0.057	± .0016	0.693	± 0.022	0.087	± .0014	0.510	540.5	± 8.3	509	± 60	-6
41-6.1	0.68	864	22	0.026	0.059	± .0010	0.710	± 0.017	0.088	± .0014	0.669	542.9	± 8.3	552	± 39	2
41-7.1	1.04	598	98	0.169	0.054	± .0022	0.617	± 0.027	0.083	± .0014	0.369	514.2	± 8.1	367	± 93	-29
41-8.1	0.46	1052	97	0.096	0.057	± .0014	0.674	± 0.020	0.086	± .0014	0.536	533.2	± 8.2	479	± 56	-10
41-9.1	1.63	675	102	0.156	0.059	± .0023	0.685	± 0.029	0.084	± .0014	0.378	522.2	± 8.1	561	± 87	8

Table 8. Sm-Nd Isotopic Data for Selected Samples from the Leeuwin Complex

Sample	Est. Age (Ma)[a]	Nd (ppm)	Sm (ppm)	$^{147}Sm/^{144}Nd$	$^{143}Nd/^{144}Nd$		2□[b]	ϵNd
RVLC001	750	17.6	4.3	0.1462	0.512255	±	.000006	-2.65
RVLC012	750	69.8	11.1	0.0960	0.512085	±	.000006	-1.14
RVLC020	750	72.6	13.9	0.1156	0.512163	±	.000006	-1.51
RVLC034	1090	17.7	4.0	0.1350	0.511852	±	.000006	-6.75
RVLC035	1090	12.1	3.5	0.1723	0.511900	±	.000006	-11.03
RVLC041	750	54.8	10.0	0.1098	0.512186	±	.000006	-0.48
RVLC070	750	91.6	17.0	0.1119	0.512087	±	.000006	-2.63
RVLC080	750	133.4	25.2	0.1144	0.512128	±	.000006	-2.07

[a] Ages represent crystallisation age, for clarity 750Ma has been applied to all samples except 034 & 035 as this best represents a homogenous crystallisation age. For samples 034 & 035 the igneous age from Nelson (1999) has been applied. [b] Isotope error measurements are 2□. $^{143}Nd/^{144}NdCHUR(0) = 0.512638$, $^{147}Sm/^{144}NdCHUR = 0.1967$. CHUR = chondroitic uniform reservoir. Depleted mantle model as per Goldstein et al. (1984): $^{143}Nd/^{144}Nd = 0.51315$, $^{147}Sm/^{144}Nd = 0.2145$.

Figure 1. Reconstruction of Gondwana

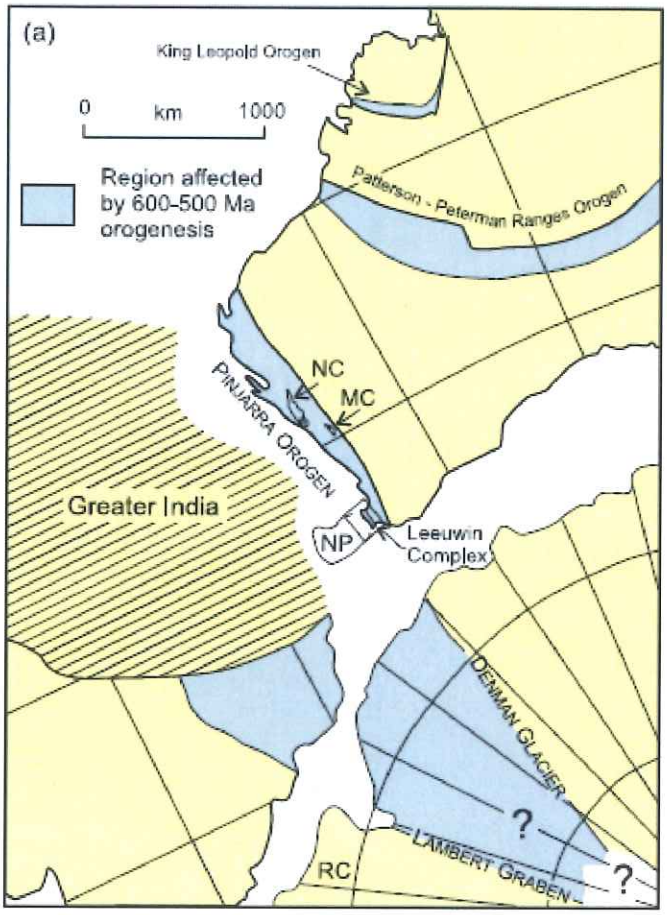

Figure 2 - Petrological, isotopic and geochronological sample locations

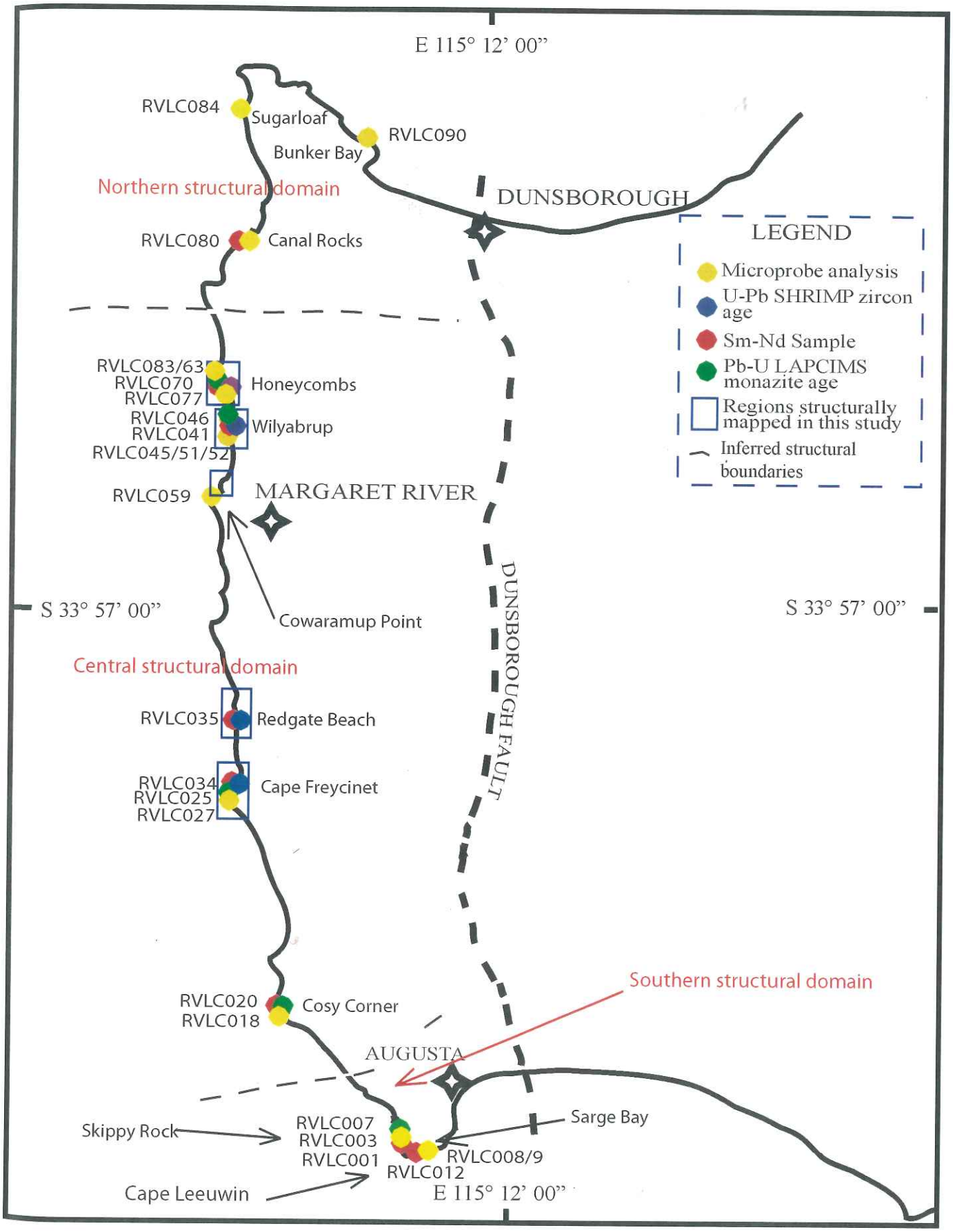

Figure 3.

Regional structural maps of the central Leeuwin Complex

a) Honeycombs

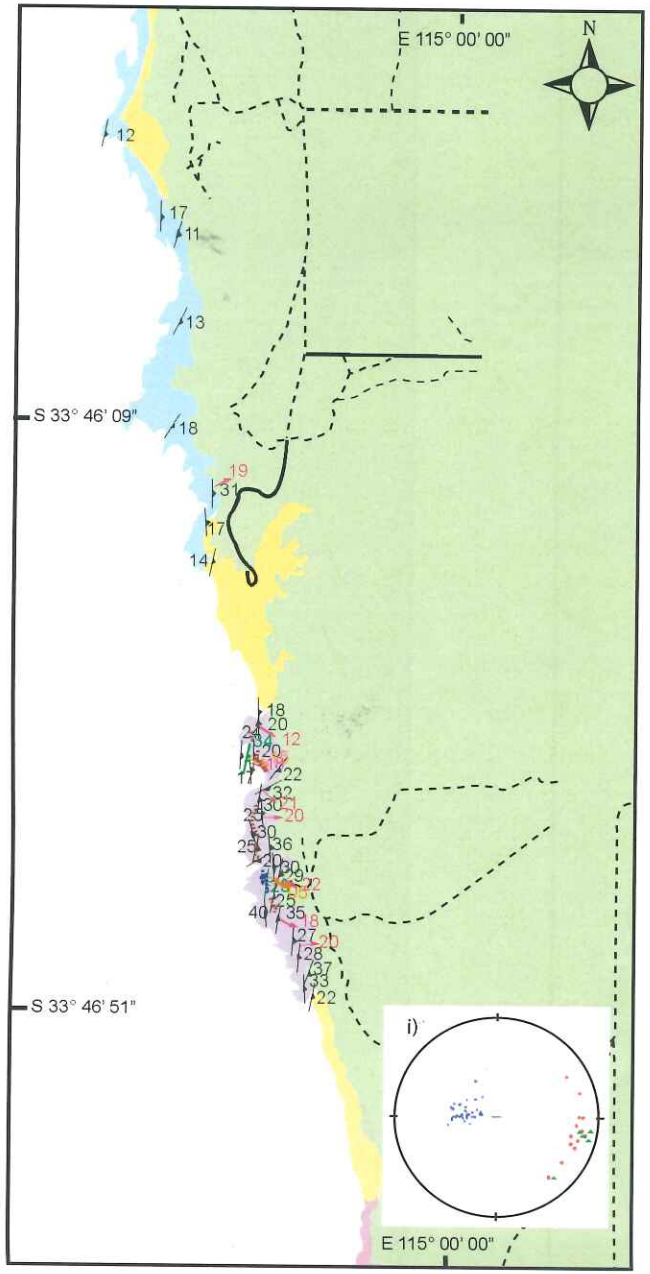

b) Willyabrup

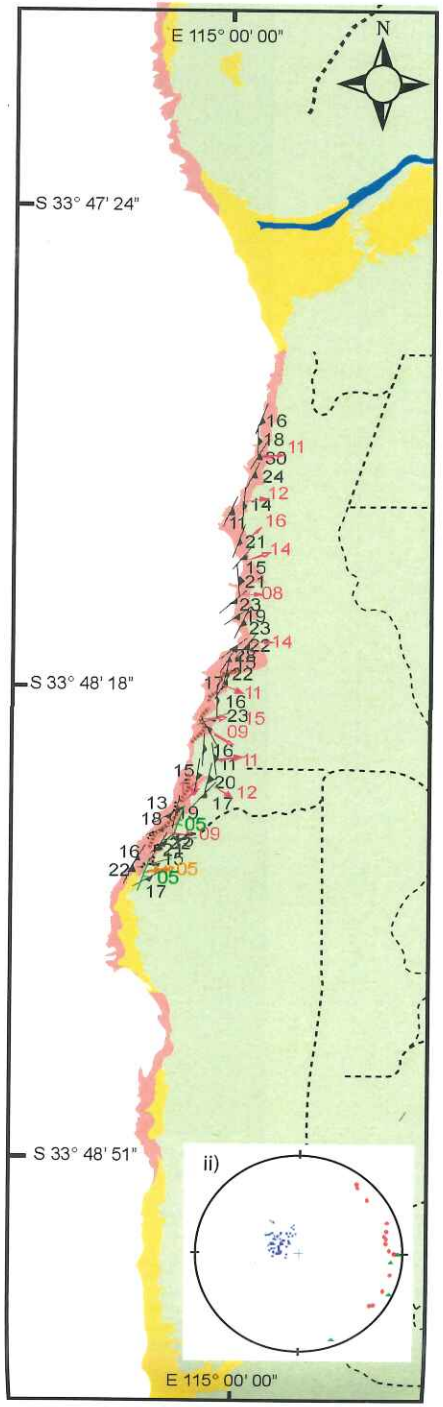

c) Gracetown (north of Cowaramup Bay)

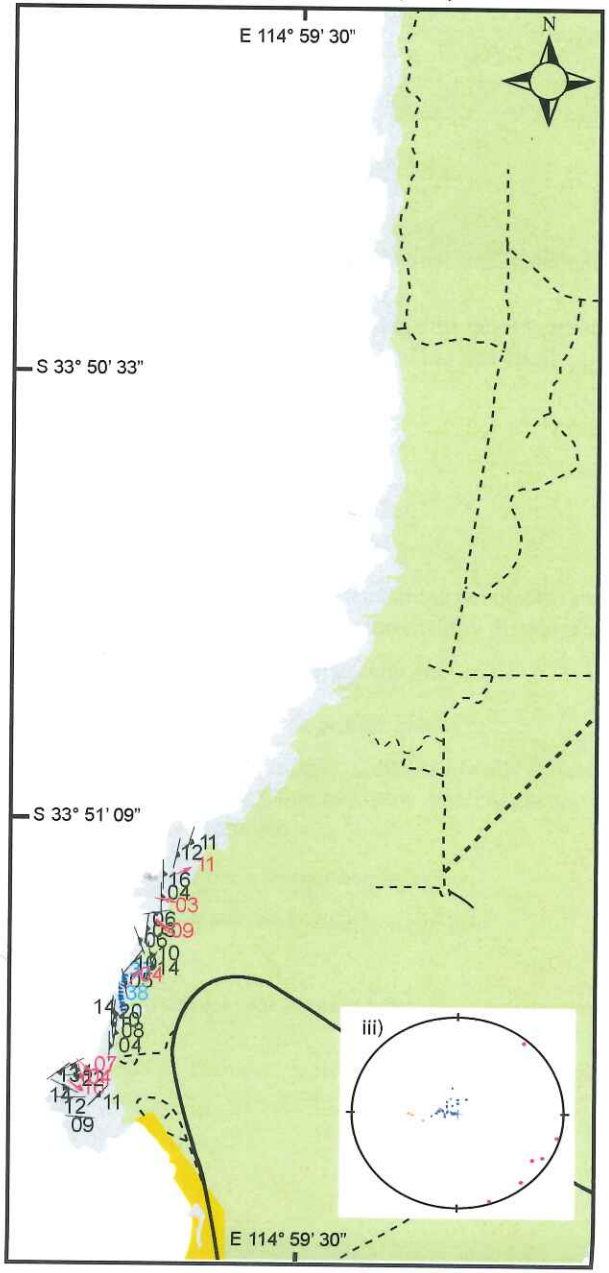

d) Redgate Beach

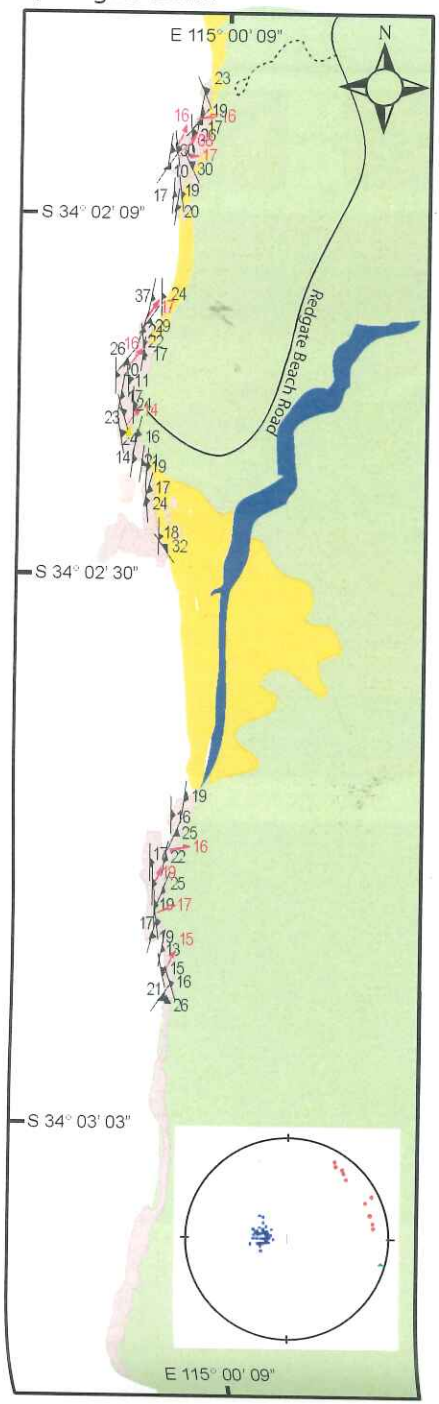

e) Cape Freycinet

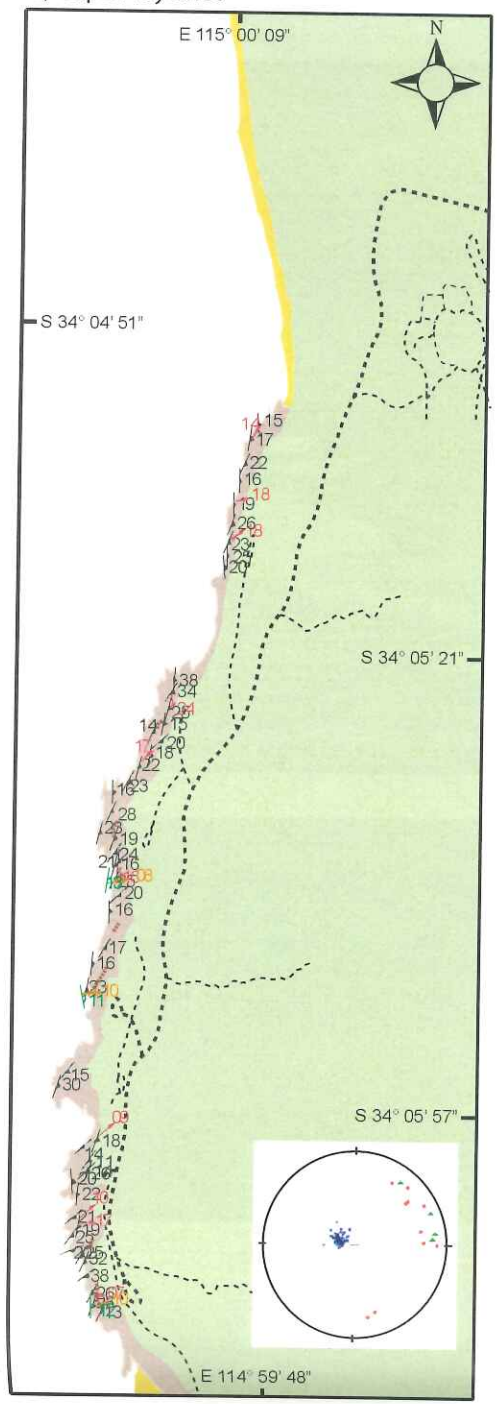

LEGEND

Unsealed Road

Sealed Road

Freshwater stream or waterway

Pleistocene deposits of beach alluvium and aeolian dune sands

Quaternary Tamala Limestone along the coast vegetated by low lying shrubland. Perennial famland and eucalypt forests inland

LITHOLOGIES

Garnet bearing granite migmatite gneiss

Garnet absent granite gneiss containing centimetre scale leucosomes that are parallel to the shallow SE dipping folia-

Garnet-bearing leucocratic granite gneiss

Orange, felsic leucocratic granite gneiss

Massive granitic gneiss Inset: Compositionally different, hornblende-Ortho & Clino pyroxene bearing gneiss with a ill-defined flat foliation.

Hornblende-biotite ± garnet amphibolites

Two Pyroxene-hornblende-biotite mafic dyke

Italic: See Metamorphic Petrology for detailed lithological descriptions

STEREONETS

Poles to foliation

Mineral Lineation

Fold Hinges

Figure 4. D2 folding of intruded amphibolite and preservation of S1 foliation

a)

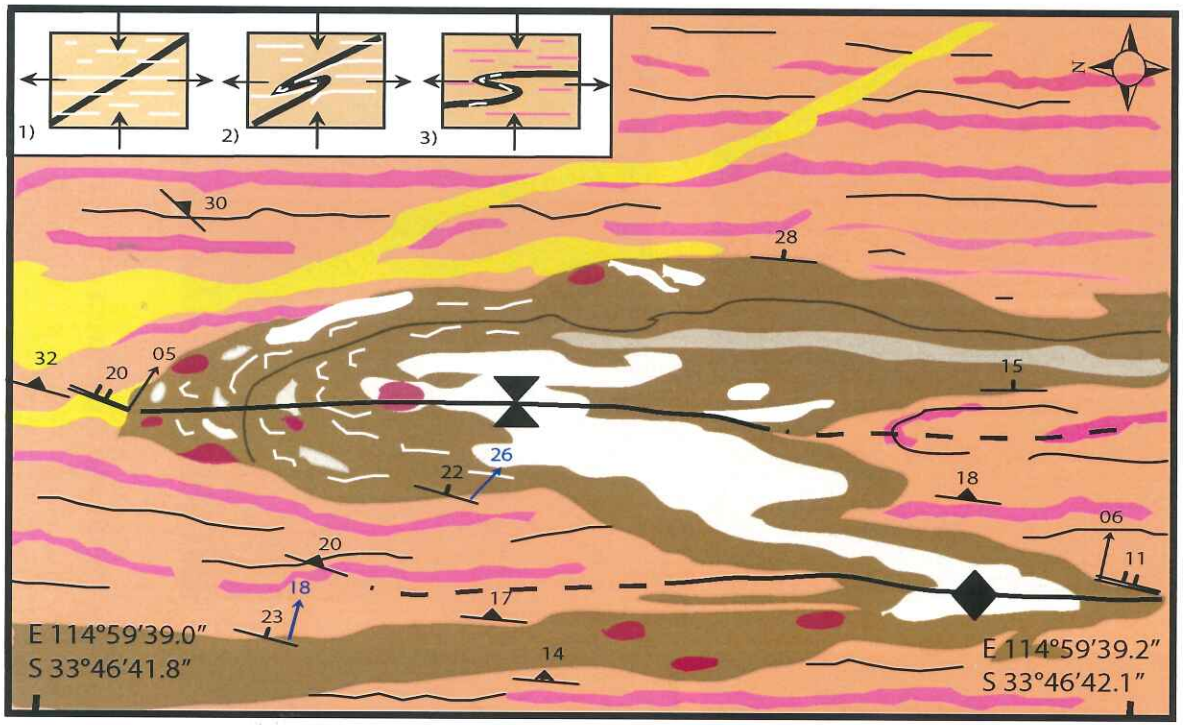

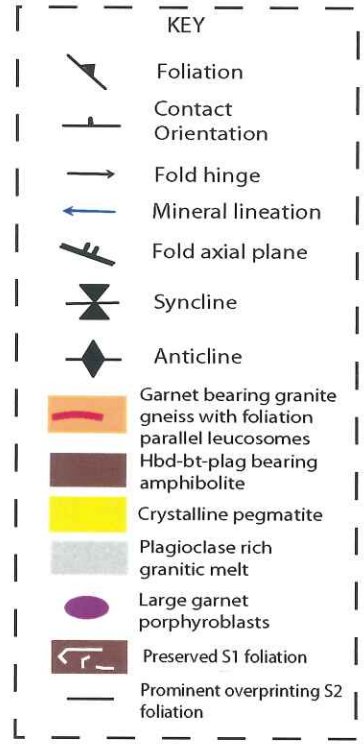

b)

Figure 5.

Field photographs of deformation structures

Figure 6. 'Kink' folding of leucosomes, Honeycombs

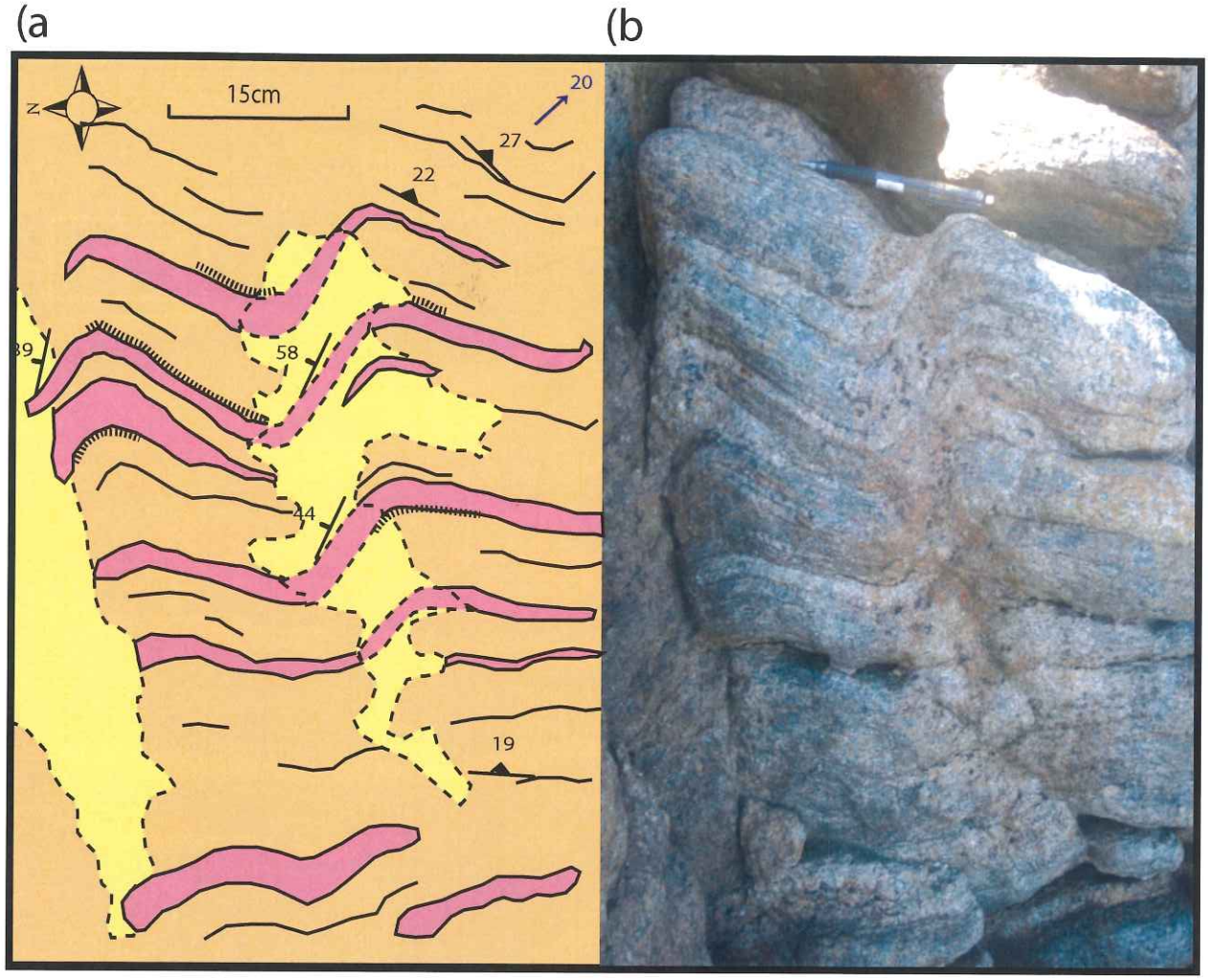

KEY

- Garnet bearing leucocratic granite gneiss
- K-feldspar, garnet bearing leucosomes
- Diffuse leucosome boundaries in 'kink' folds
- Diffuse, nebulitic crosscutting pegmatites
- Biotite rich selvages
- Dominant S2 mineral foliation
- 27 — Foliation dip/dip direction
- 44 — Orientation fold of 'kink' folds
- 20 — Mineral elongation lineation

STEREONETS

- Poles to plane of 'Kink' folds
- Poles to plane of conjugate 'Kink' folds
- Mineral elongation lineation
- Fold hinges

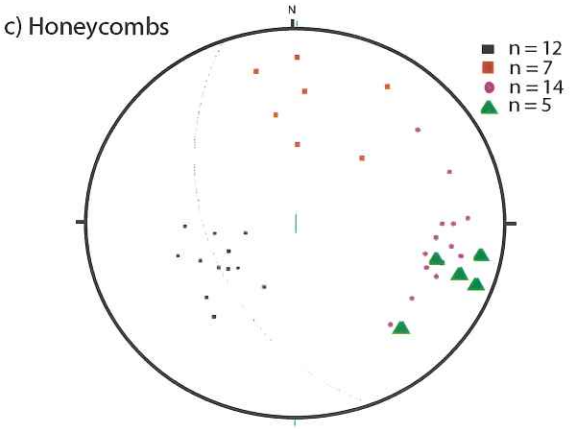

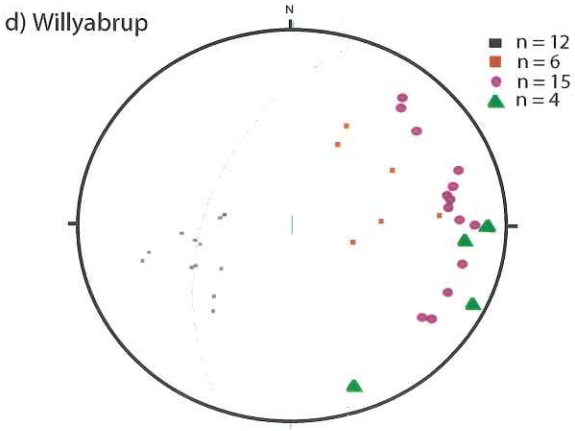

Figure 7. Strain partitioning to amphibolite layers, honeycombs

E 114° 59′ 38.1″
S 33° 46′ 29.8″

E 114° 59′ 38.1″
S 33° 46′ 30.1″

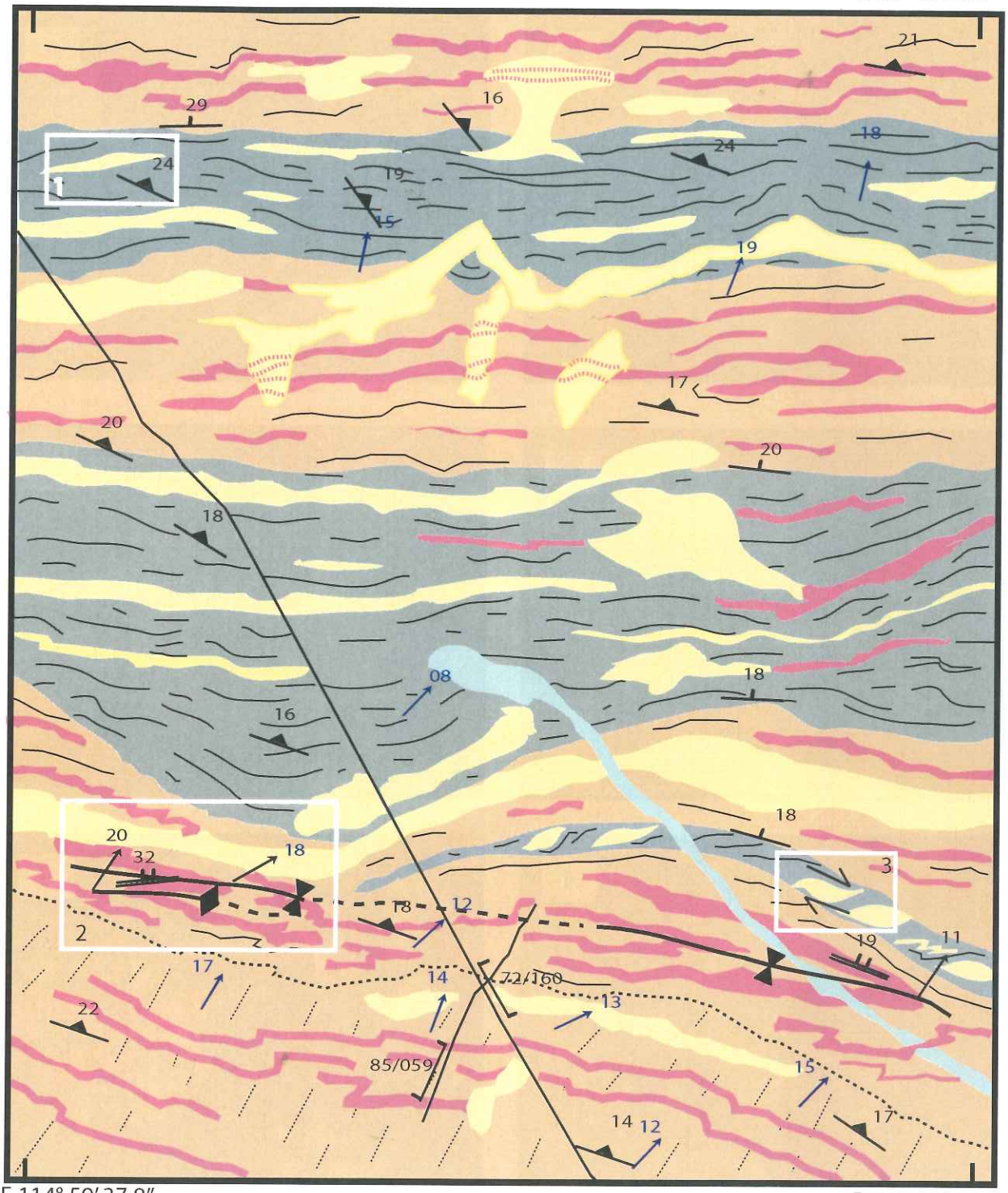

E 114° 59′ 37.8″
S 33° 46′ 29.7″

E 114° 59′ 37.7″
S 33° 46′ 36.0″

Key

- Foliation
- Contact
- Orientation
- Fold hinge
- Mineral lineation
- Fold axial plane
- Syncline
- Anticline
- Joint orientation
- Late stage crosscutting, crystalline pegmatite
- Nebulitic, crosscutting pegmatites
- K-feldspar rich, garnet bearing leucosomes
- Diffuse boundaries of leucosomes
- Mineral elongation lineations on foliation plane
- Garnet bearing leucocratic granite gneiss - low strain zone
- Hornblende-biotite amphibolite: planar high strain zone
- S2 foliation
- Joint

Figure 8. Photomicrographs, illustrating key mineral characteristics

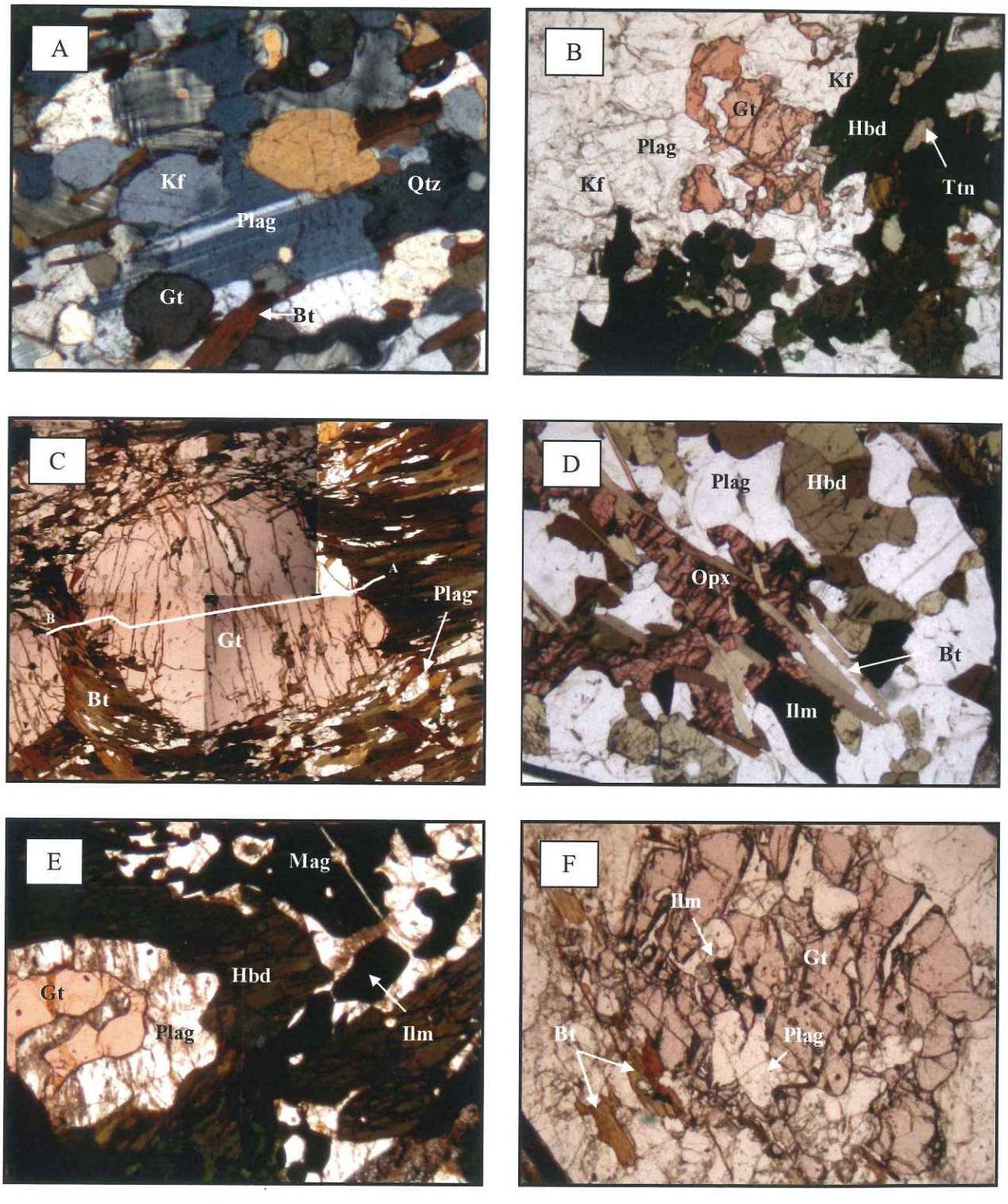

Figure 9. Garnet transect, illustrating chemical zoning within the outer garnet rim (Sample RVLC045).

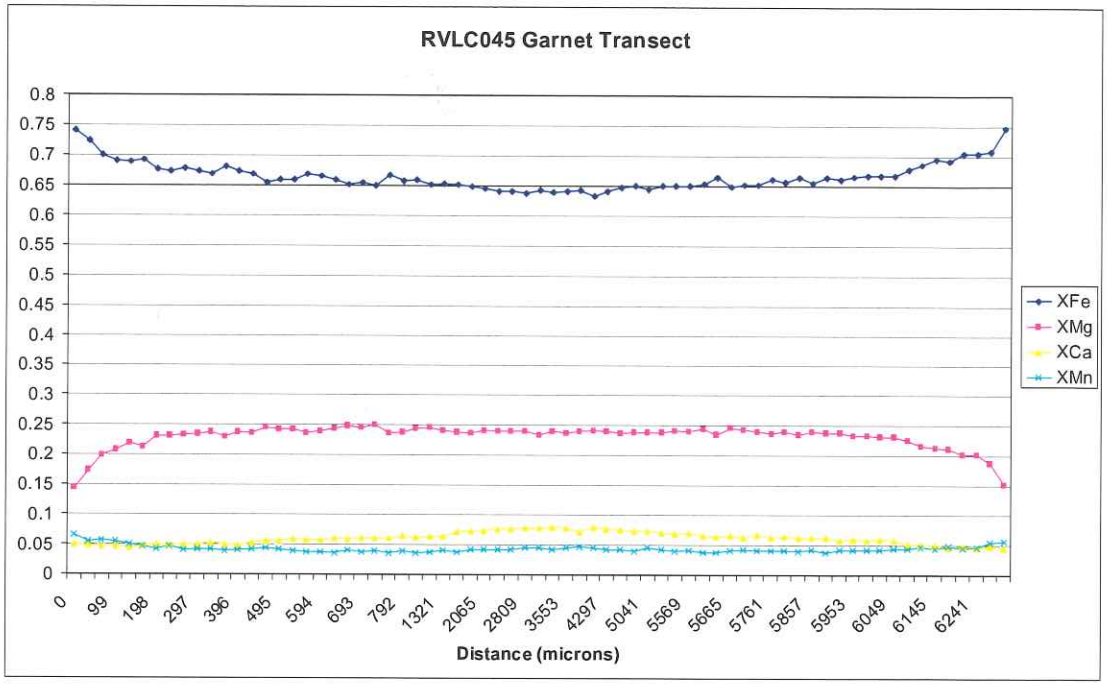

Figure 10. Localities for P-T estimations determined from core and rim mineral analyses.

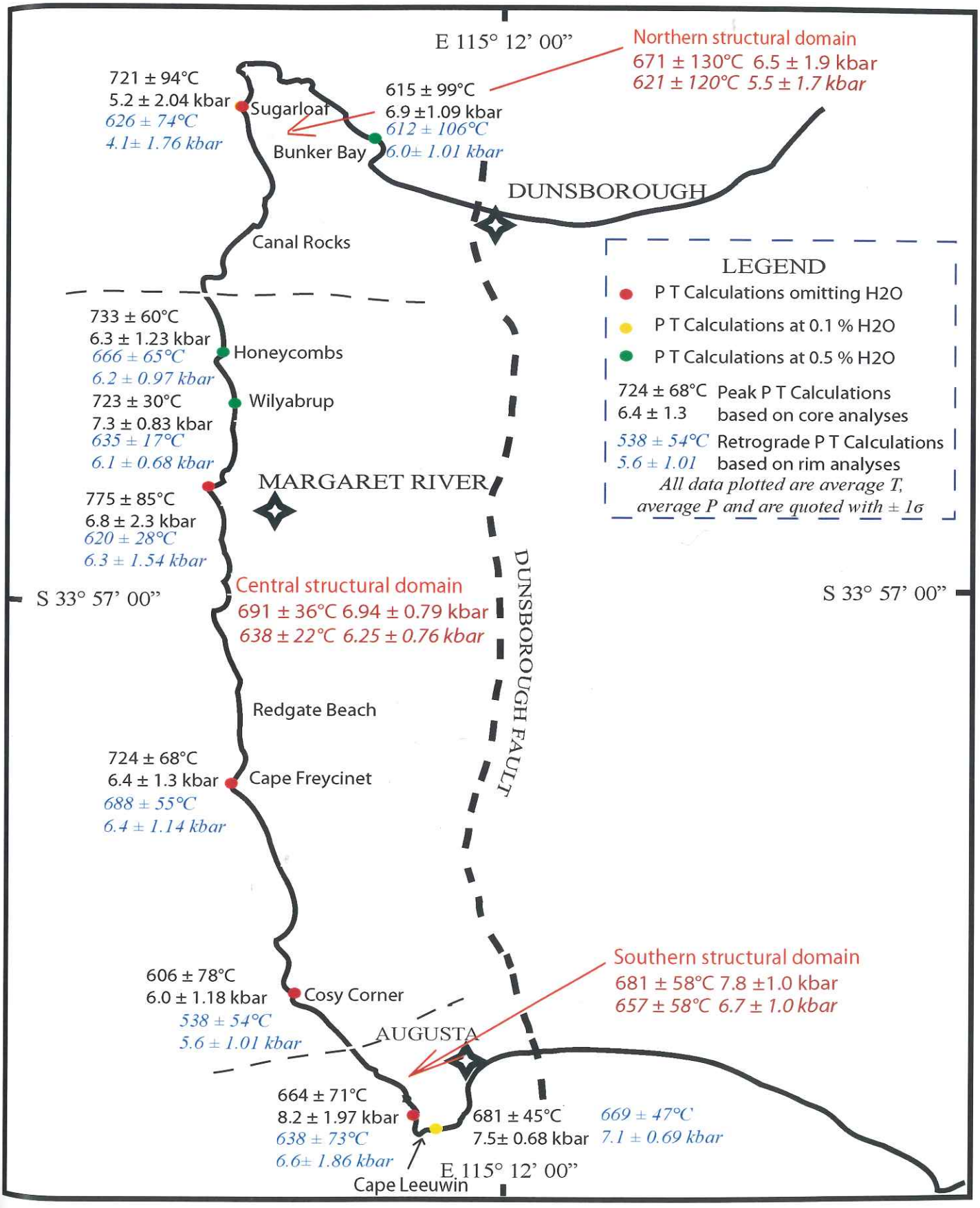

Figure 11. Metamorphic *P-T* estimates for the Leeuwin Complex based on selected *P-T* calculations identified in Table 4.

1. a) Probability plot for selected peak average temperatures identified in Table 3.

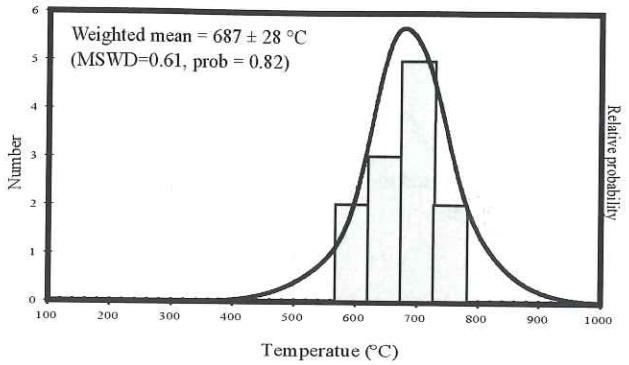

b) T°C weighted average for selected peak average temperatures

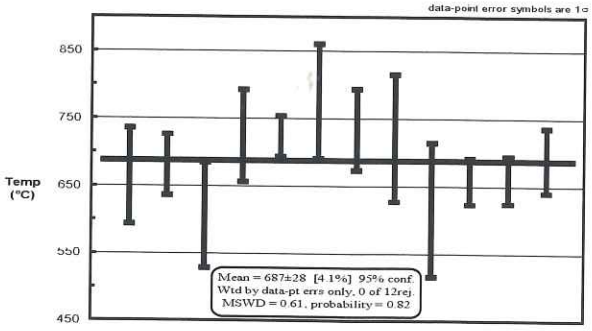

c) Probability plot for selected peak average pressures identified in Table 3.

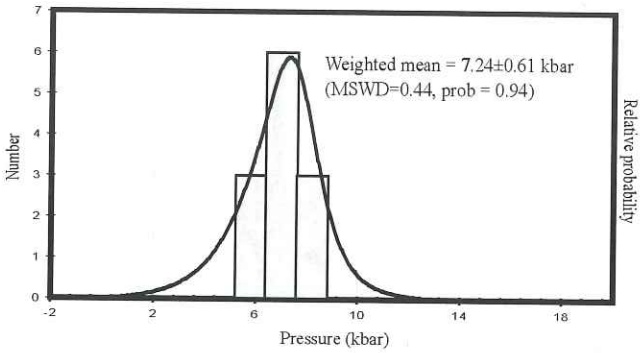

d) Kbar weighted average for selected peak average pressures

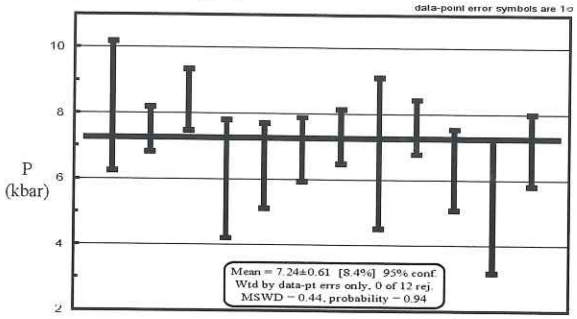

2. a) Probability plot for selected retrograde temperatures identified in Table 3.

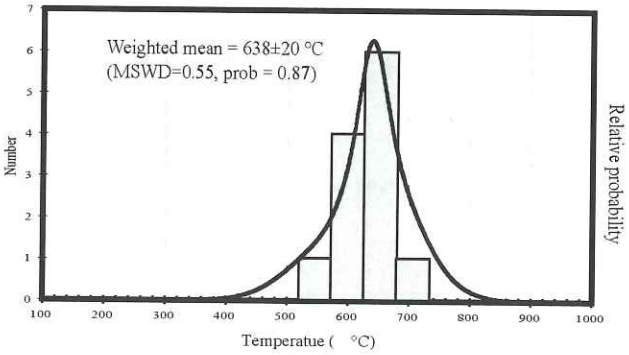

b) T°C wighted average for selected retrograde average temperatures

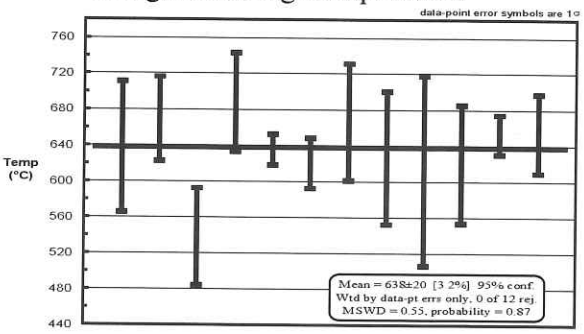

c) Probability plot for selected retrograde average pressures identified in Table 3.

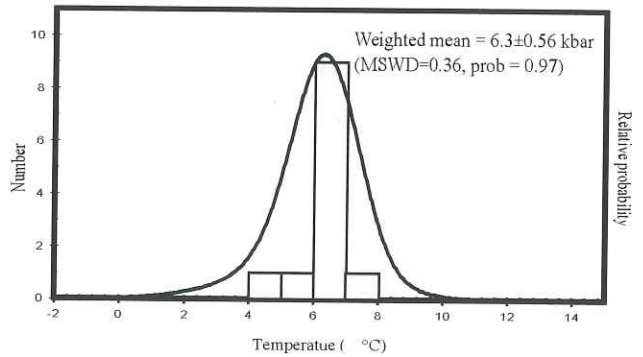

d) Kbar weighted average for selected retrograde average pressures

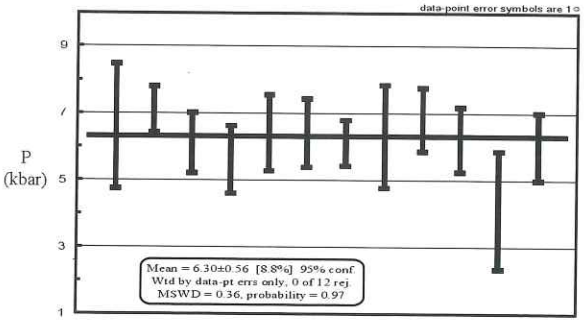

Figure 12. Geochronological data from this study and other previously published data

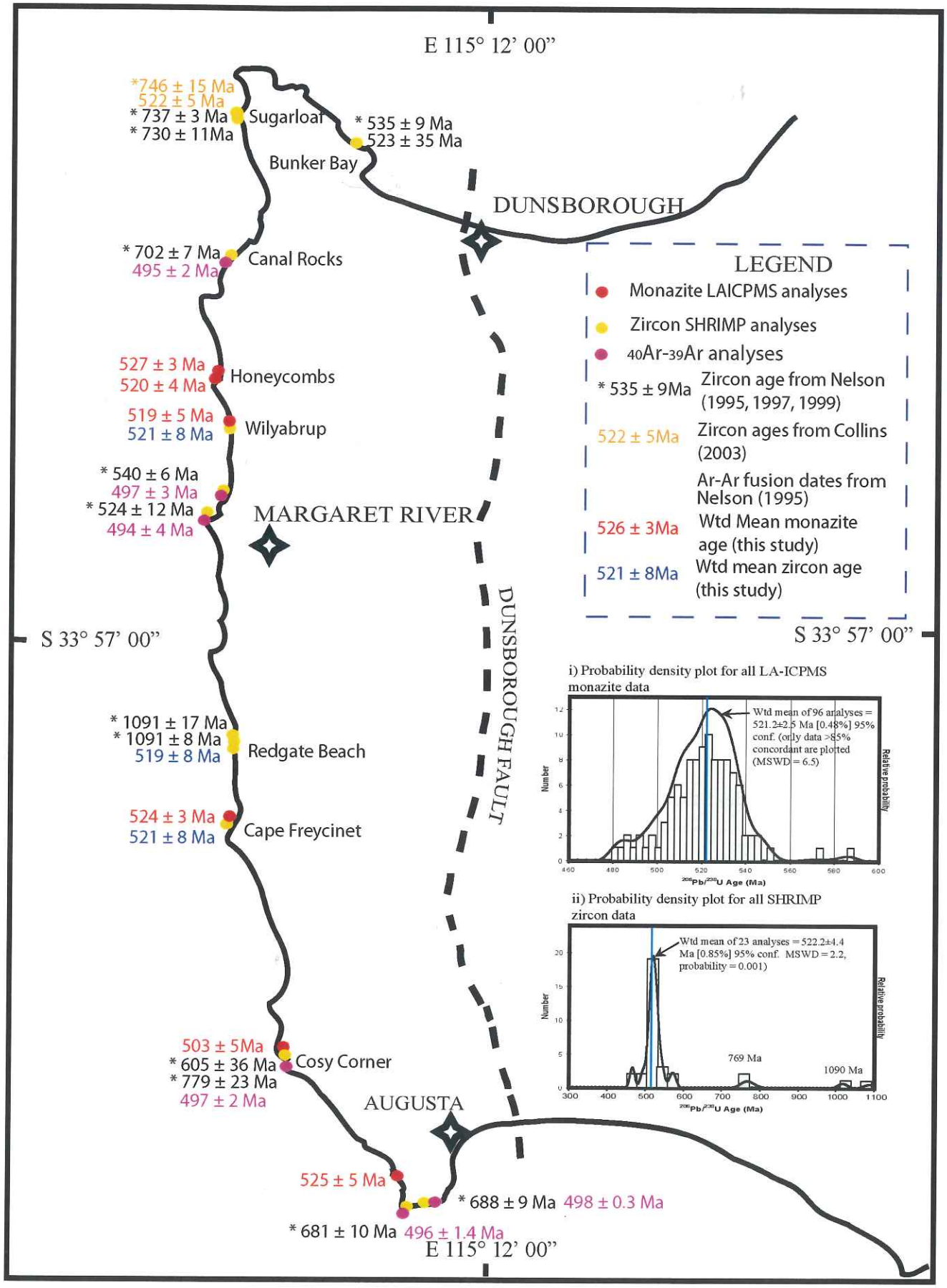

Figure 13. RVLC003 - Skippy Rock

a) Concordia diagram of all data points (n = 21)

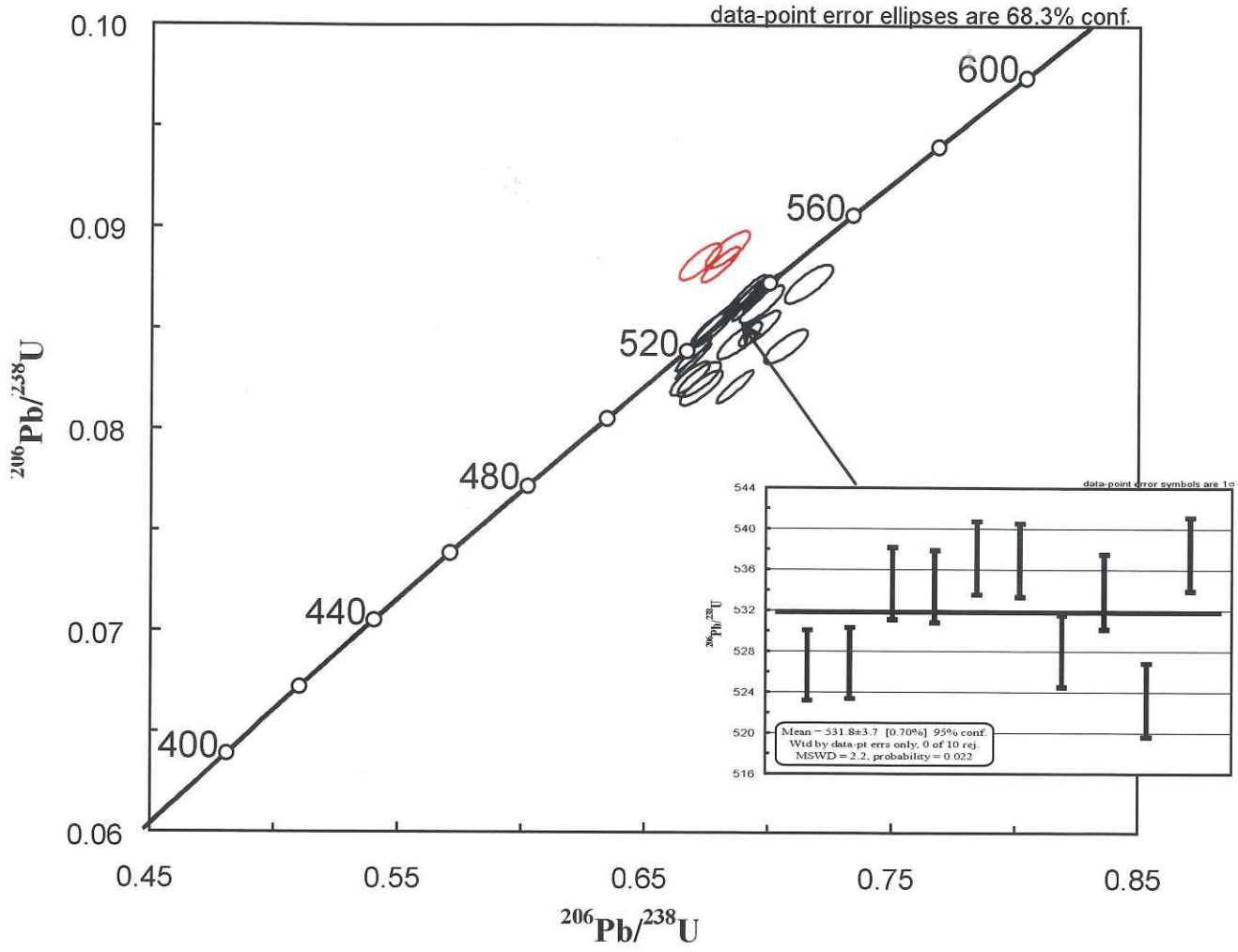

b) Probability density plot

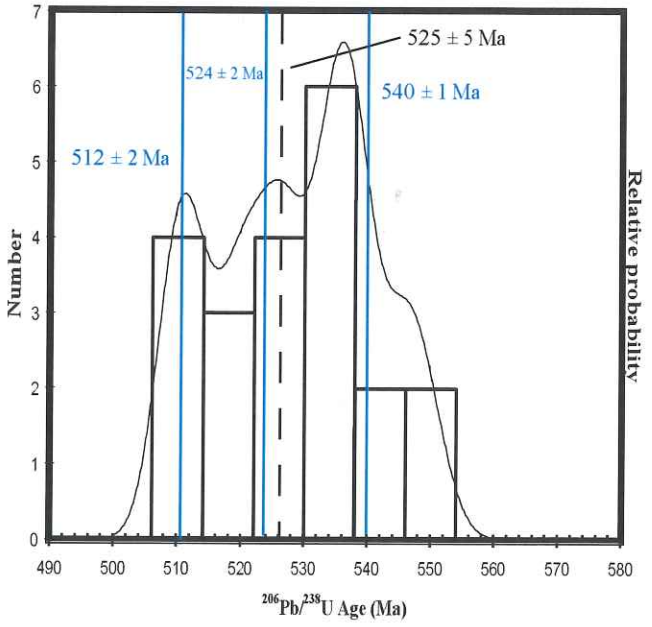

c) Weighted Average

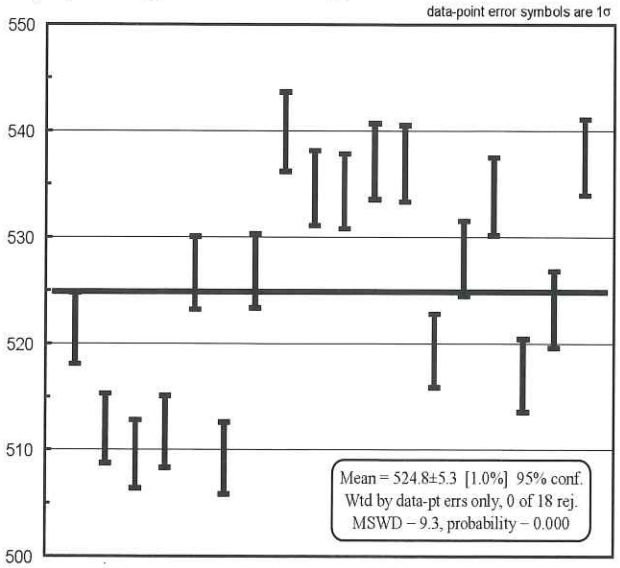

Figure 14. RVLC020 - Cosy Corner

a) Concordia diagram of all data points

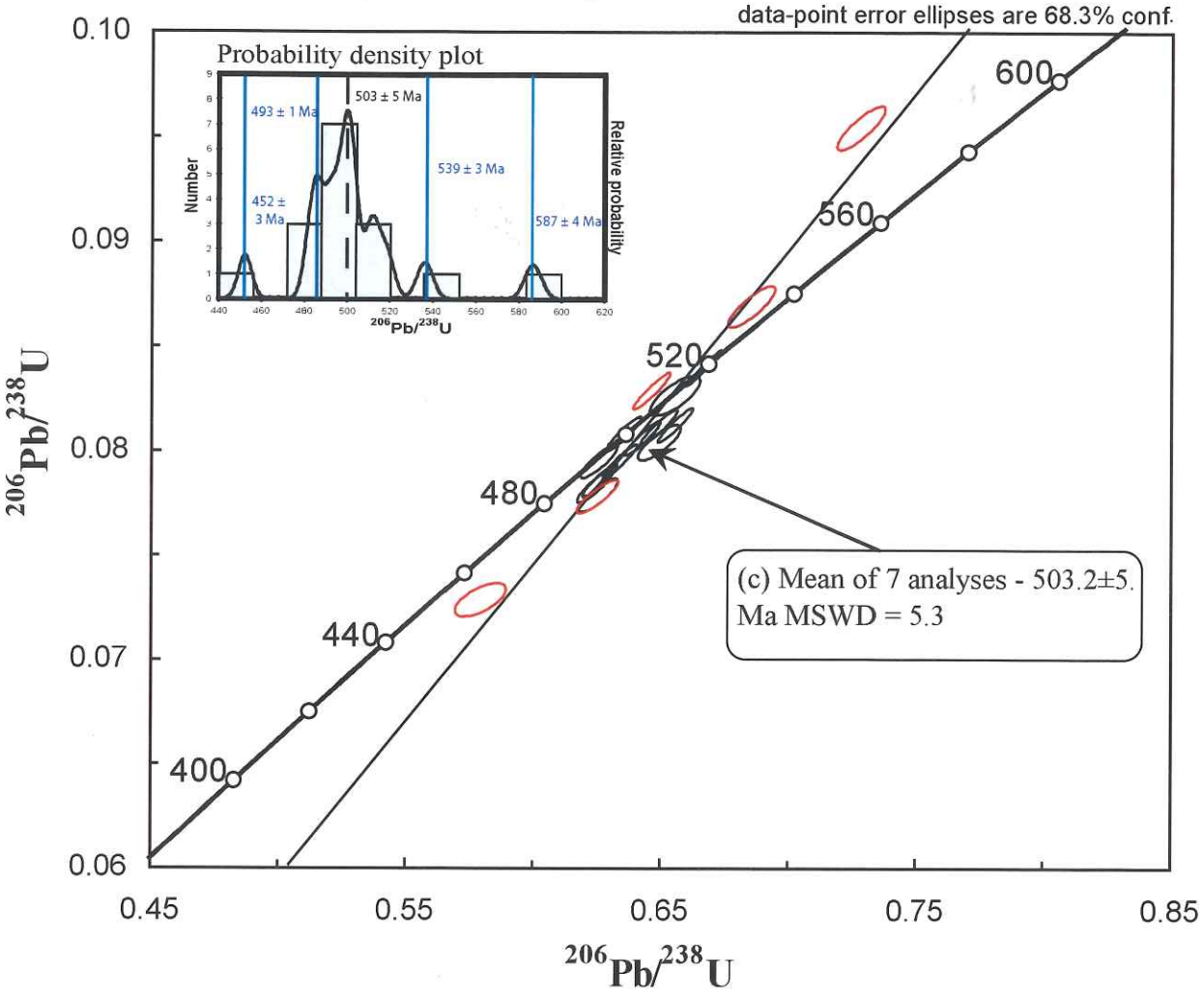

b) Tera-Wasserberg Plot

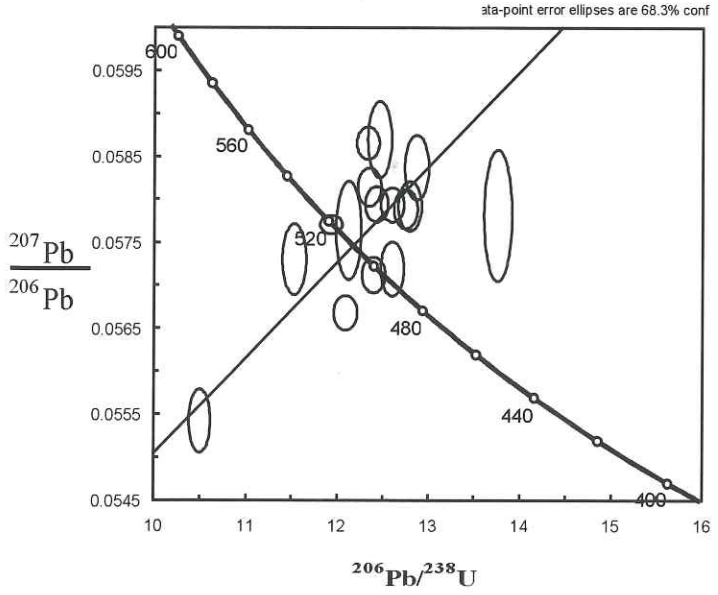

c) Weighted Average

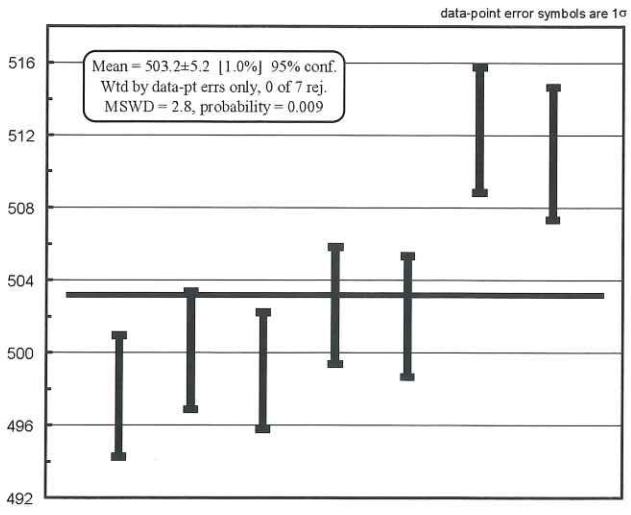

Figure 15. RVLC025 - Merchant Rocks

a) Concordia diagram of all data points

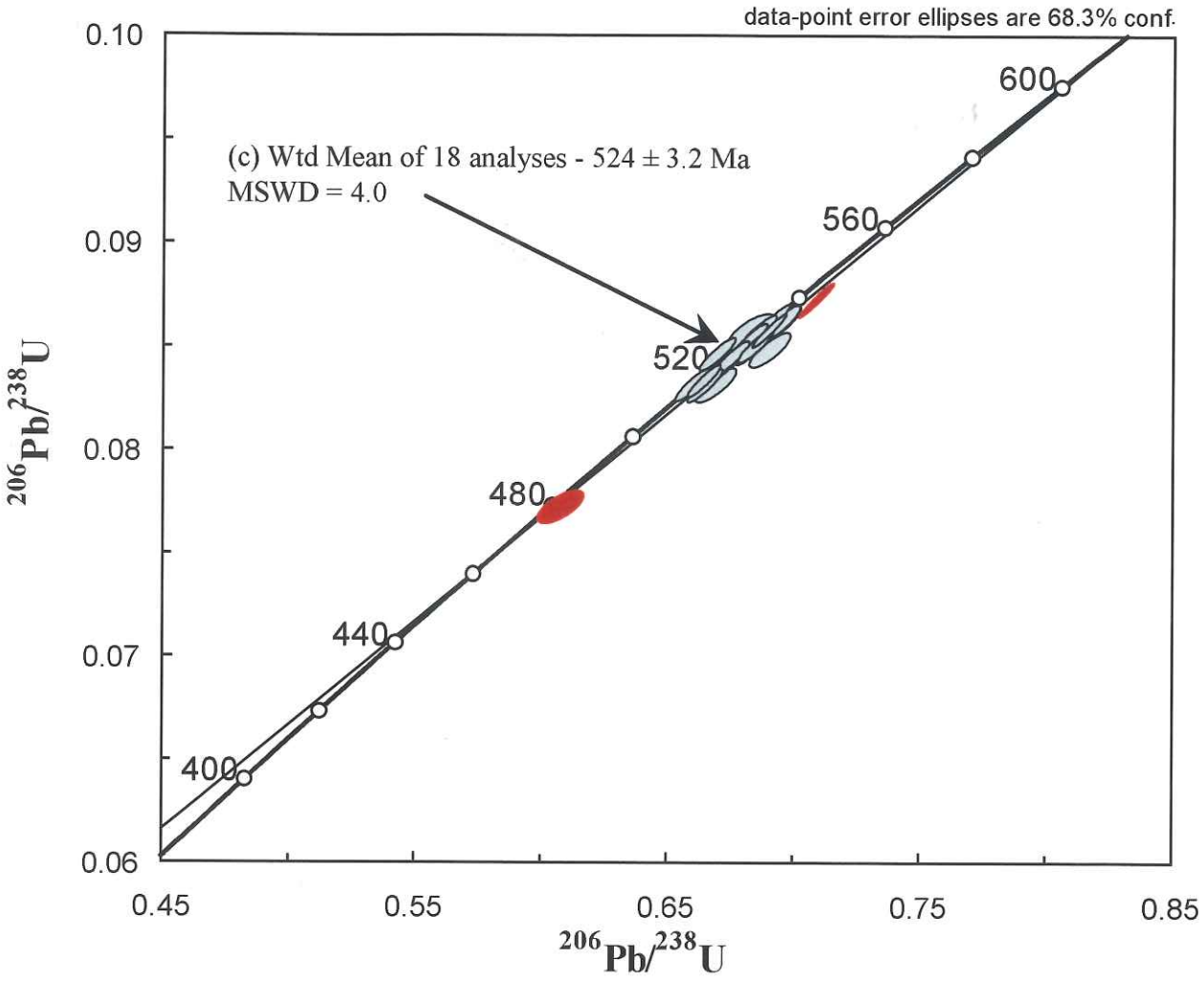

b) Probability density plot

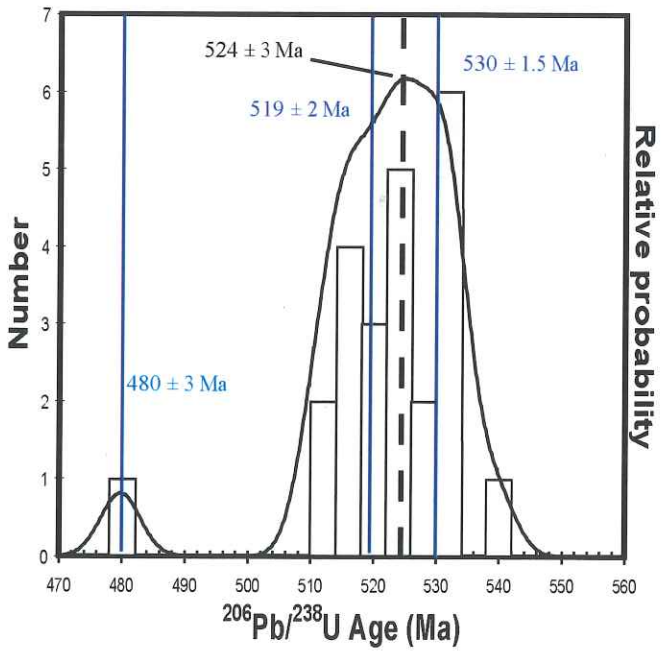

c) Weighted Average

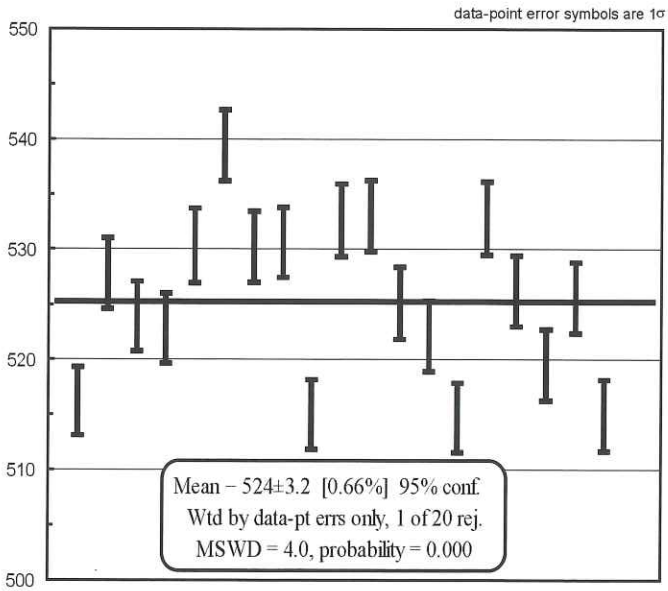

Figure 16. RVLC046 - Willyabrup Cliffs

a) Concordia diagram of all data points

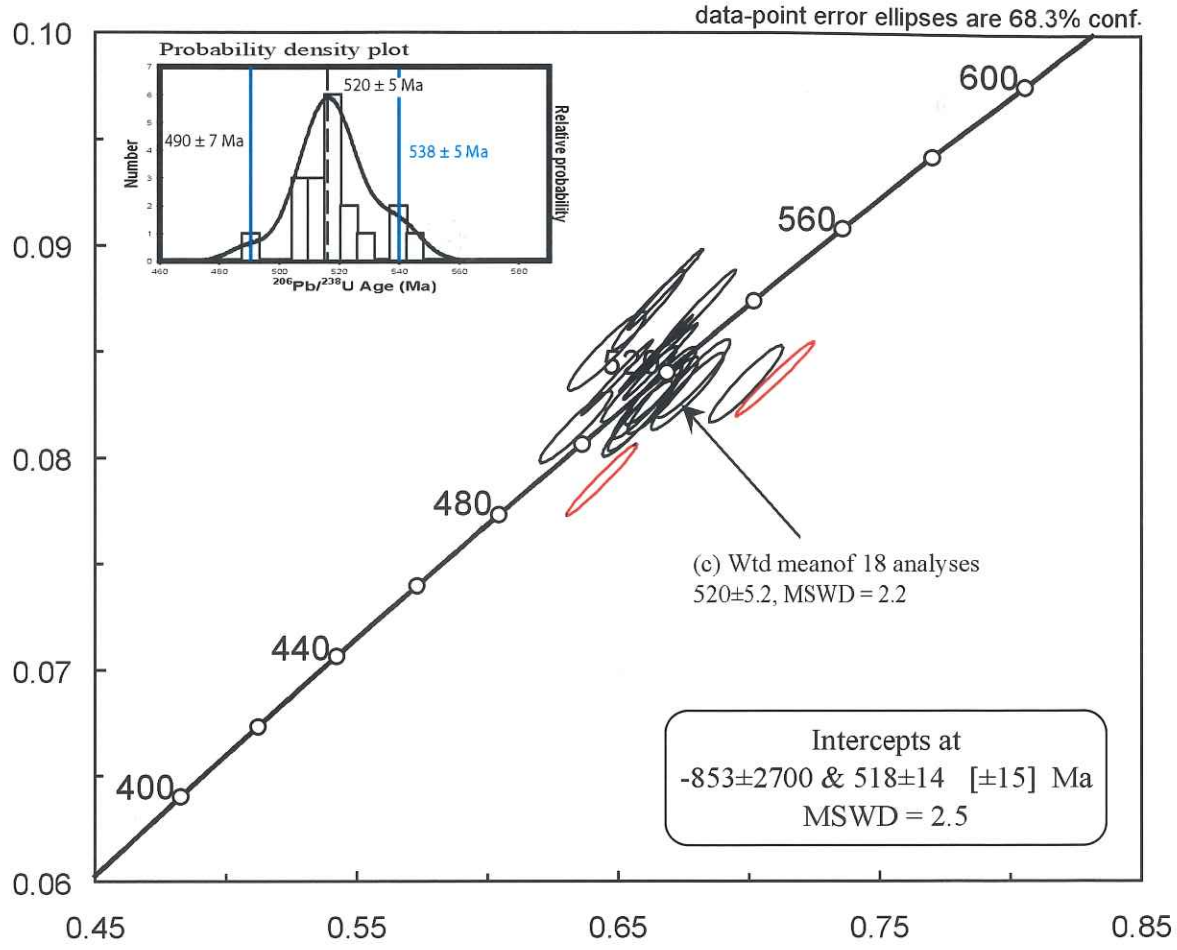

b) Terra-Wasserberg plot

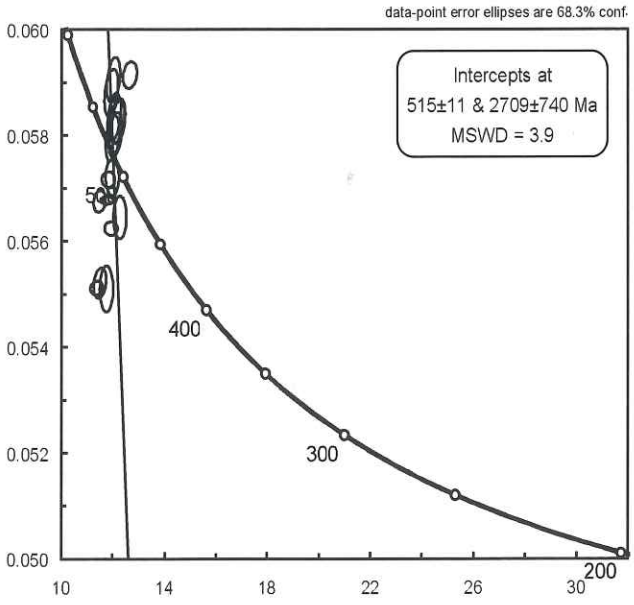

c) Weighted Average

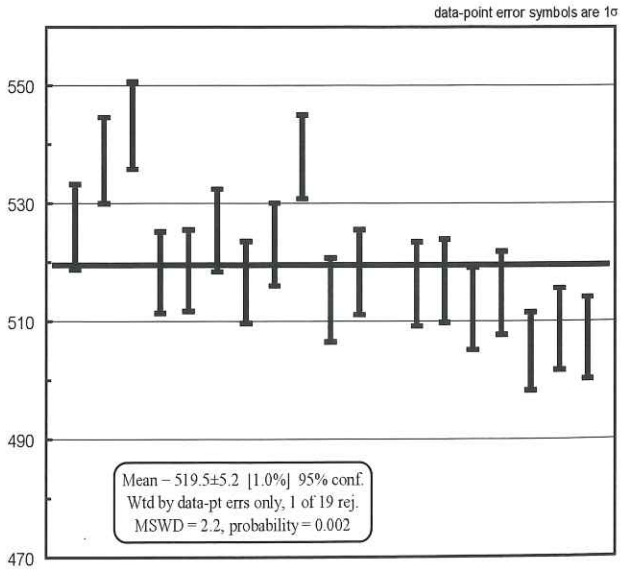

Figure 17. RVLC070 - Honeycombs

a) Concordia diagram of all data points

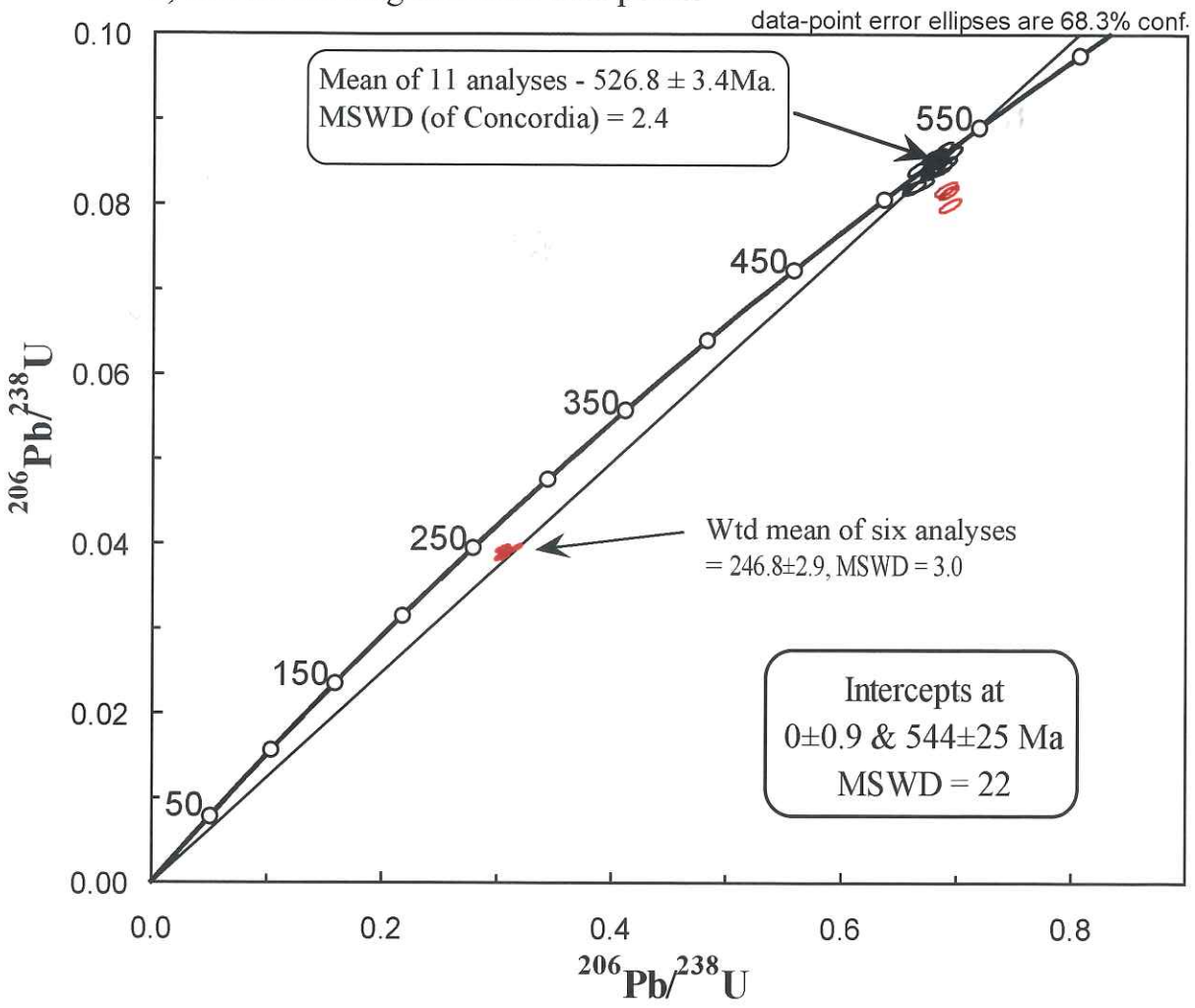

b) Probability density plot

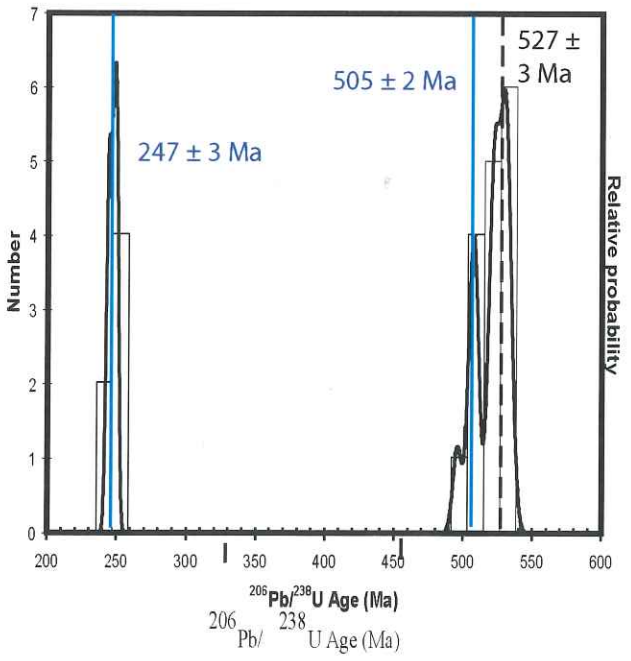

c) Weighted Average

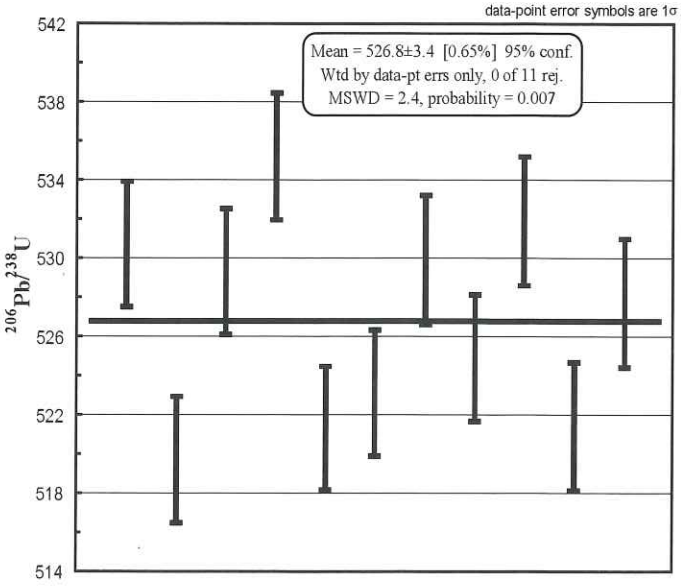

Figure 18. RVLC083 - Honeycombs

a) Concordia diagram of all data points

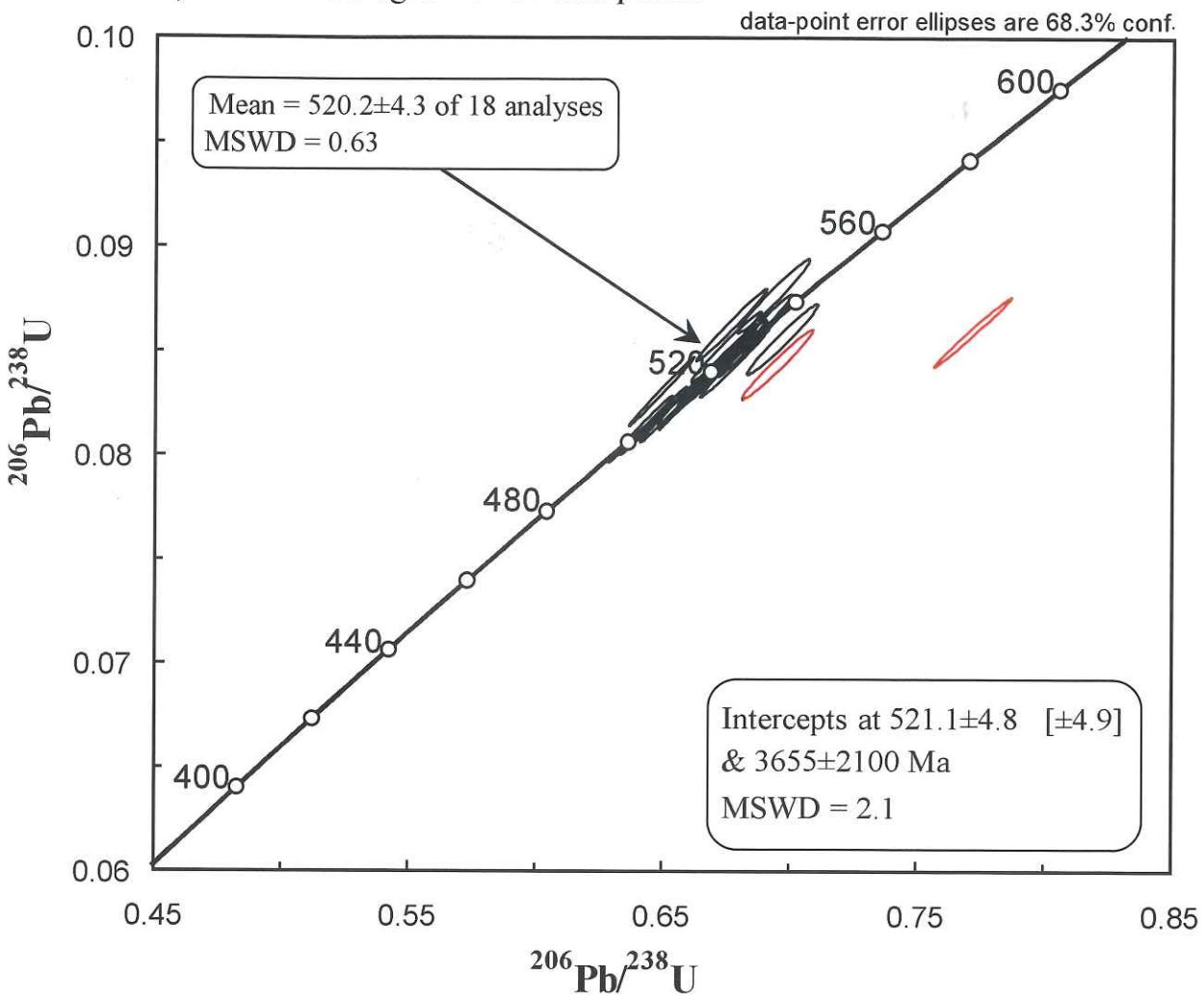

b) Probability density plot

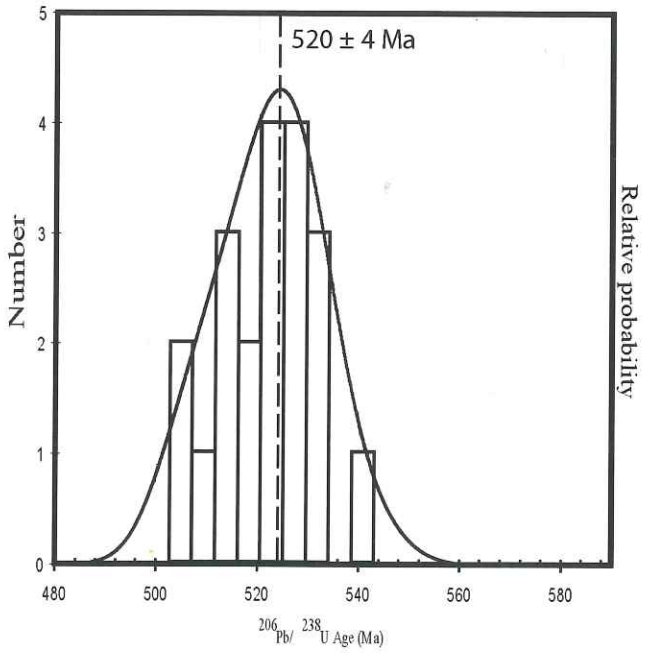

c) Weighted Average

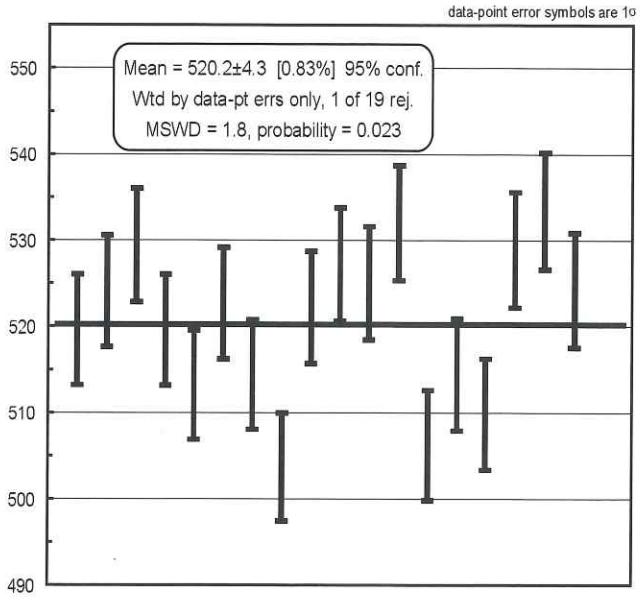

Figure 19. RVLC034 - Round Rocks (Cape Freycinet)

a) Concordia diagram of all data points

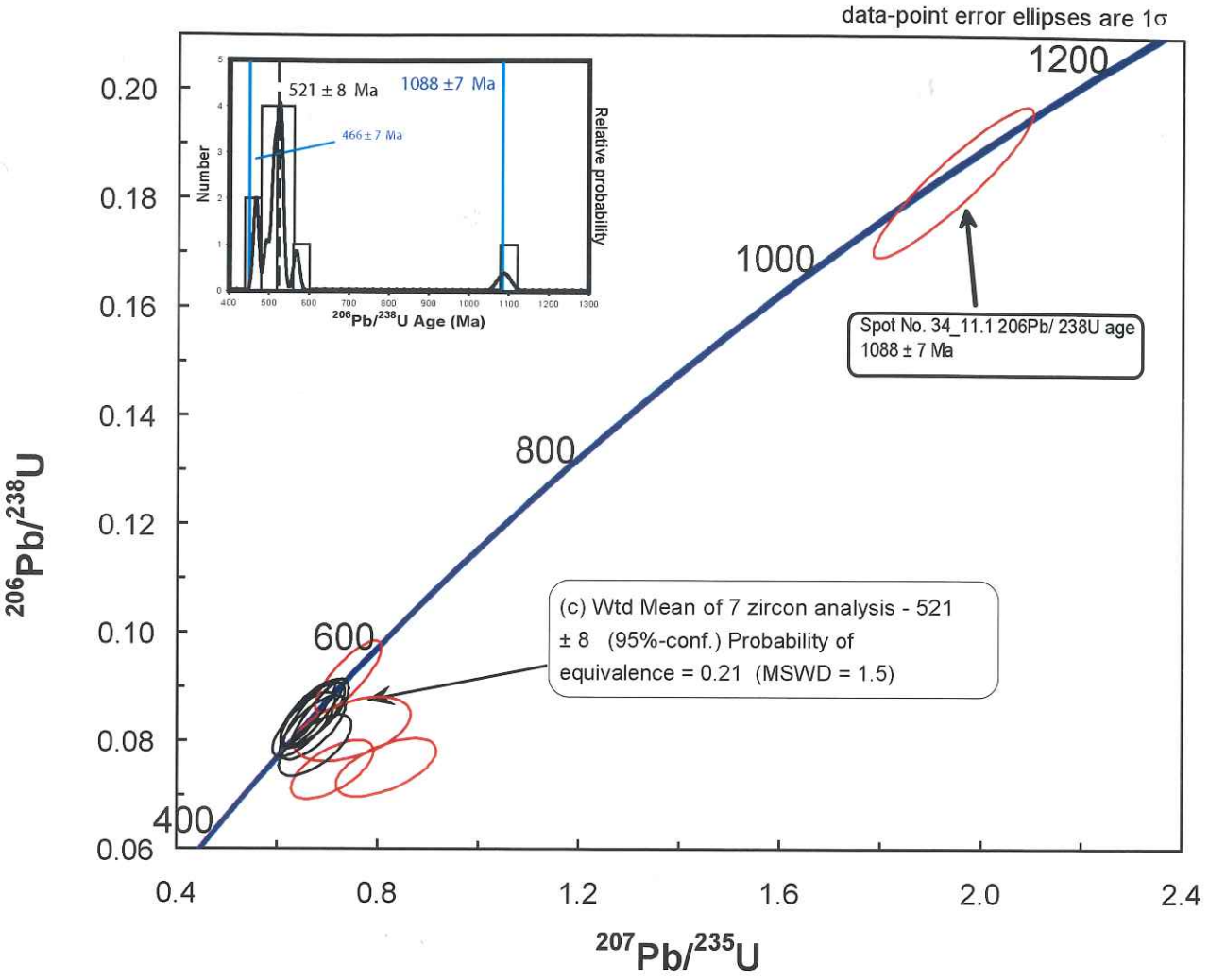

b) Concordant data

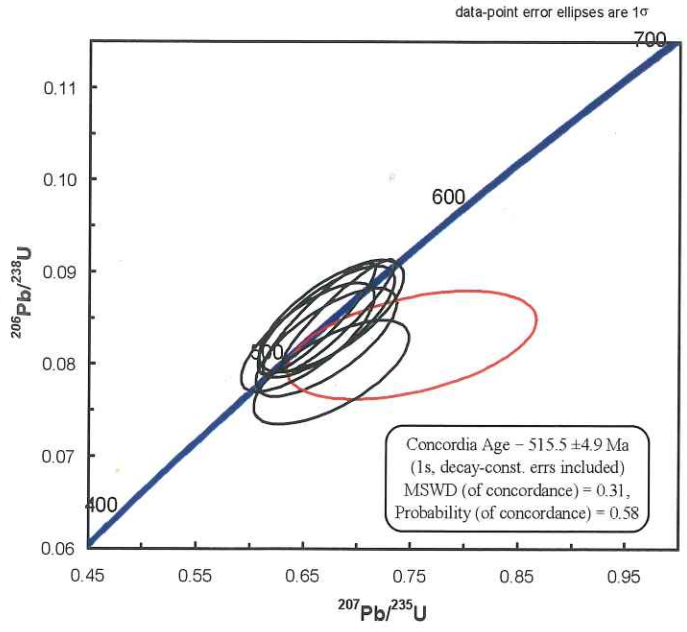

c) Weighted Average

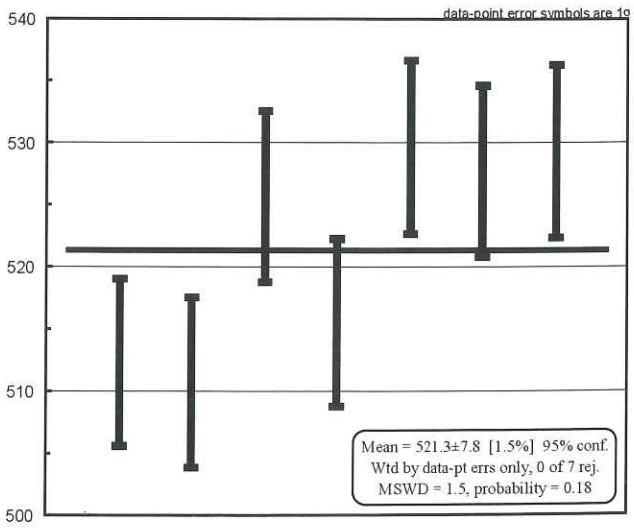

Figure 20. RVLC035 - Redgate Beach

a) Concordia diagram of all data points

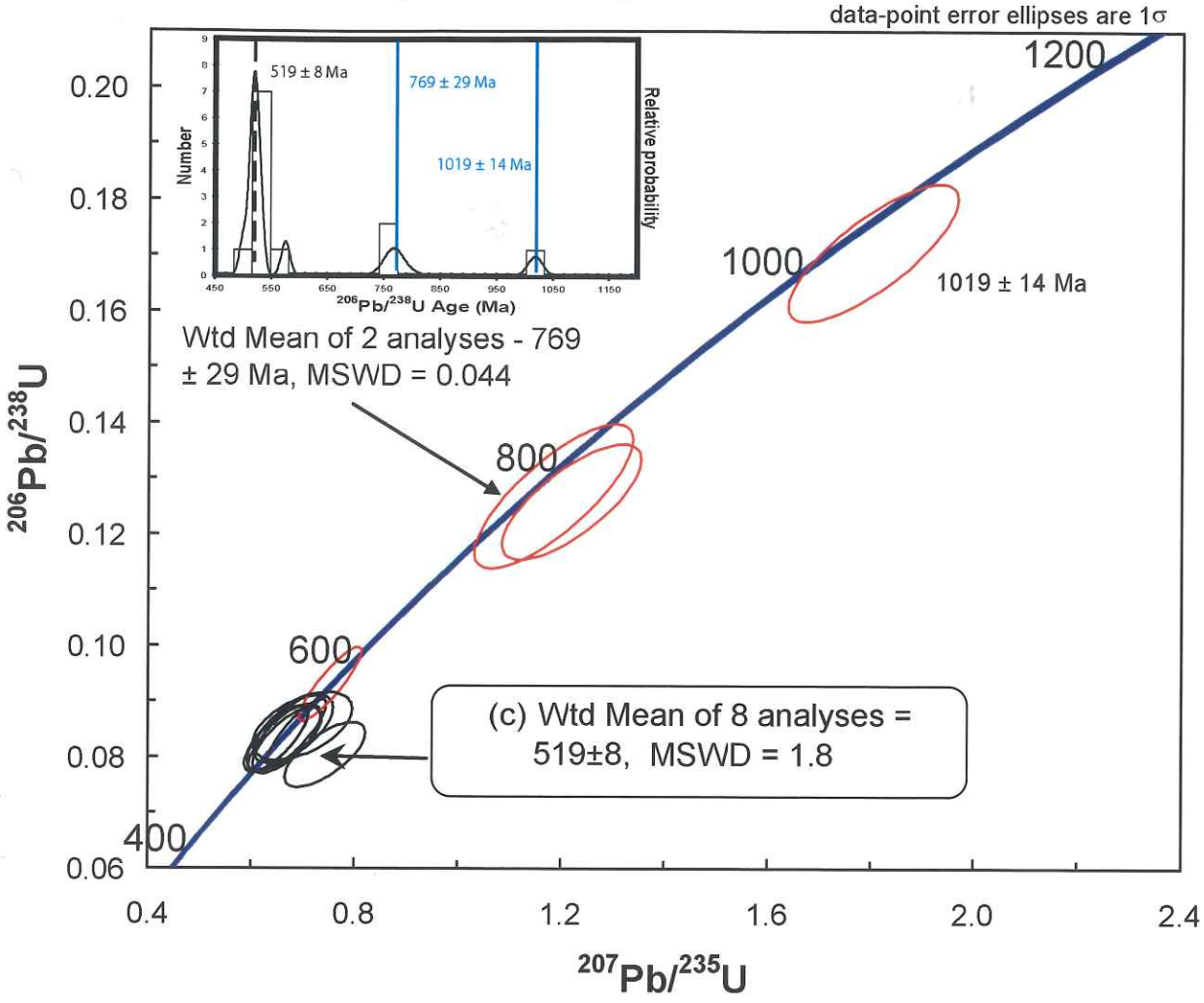

b) Concordant data

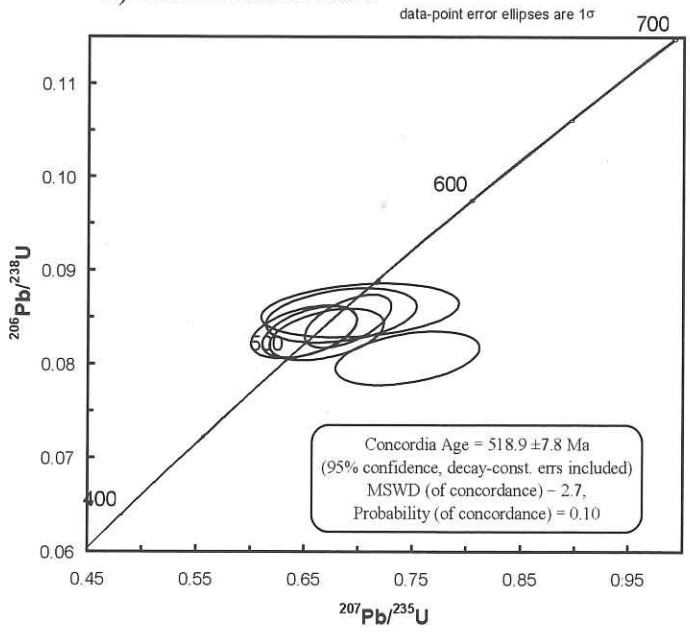

c) Weighted Average

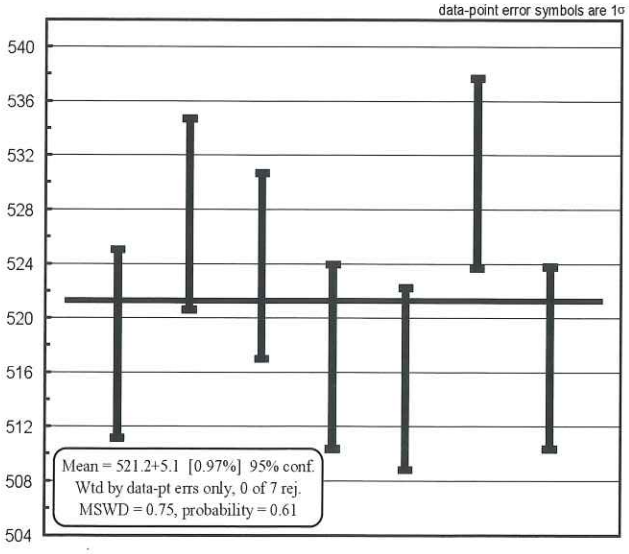

Figure 21. RVLC041 - Willyabrup Cliffs

a) Concordia diagram of all data points

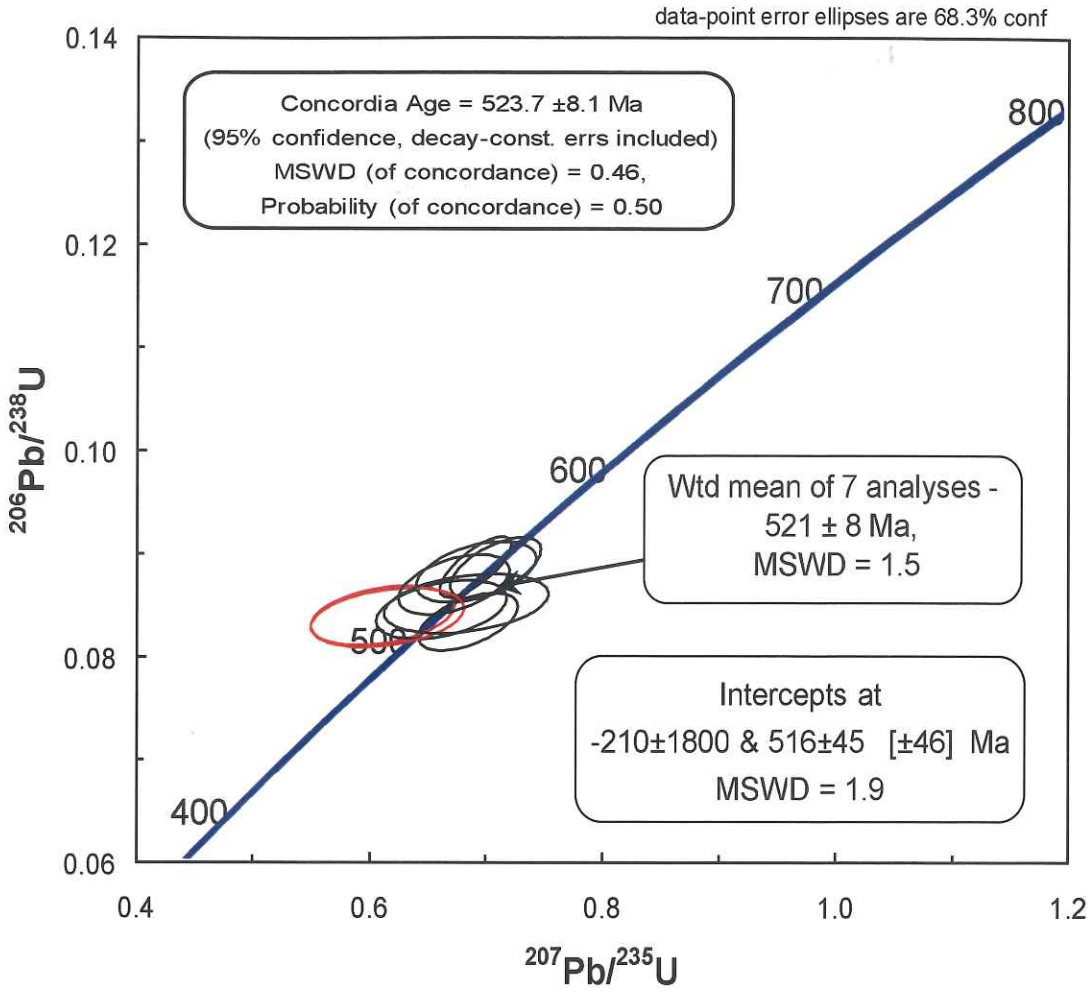

b) Probability density plot

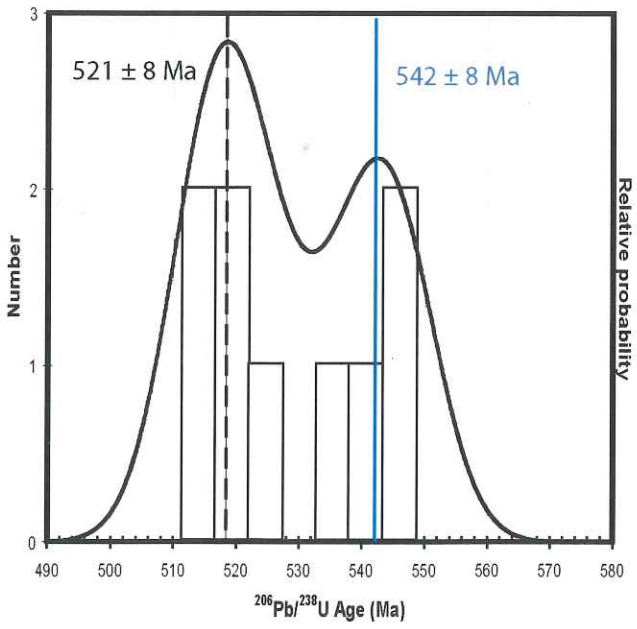

c) Weighted Average

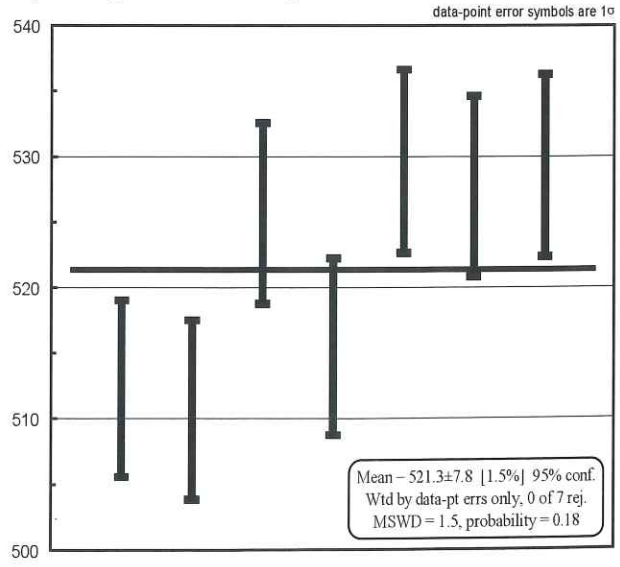

Figure 22. Epsilon Nd evolution at protolith age (Ma)

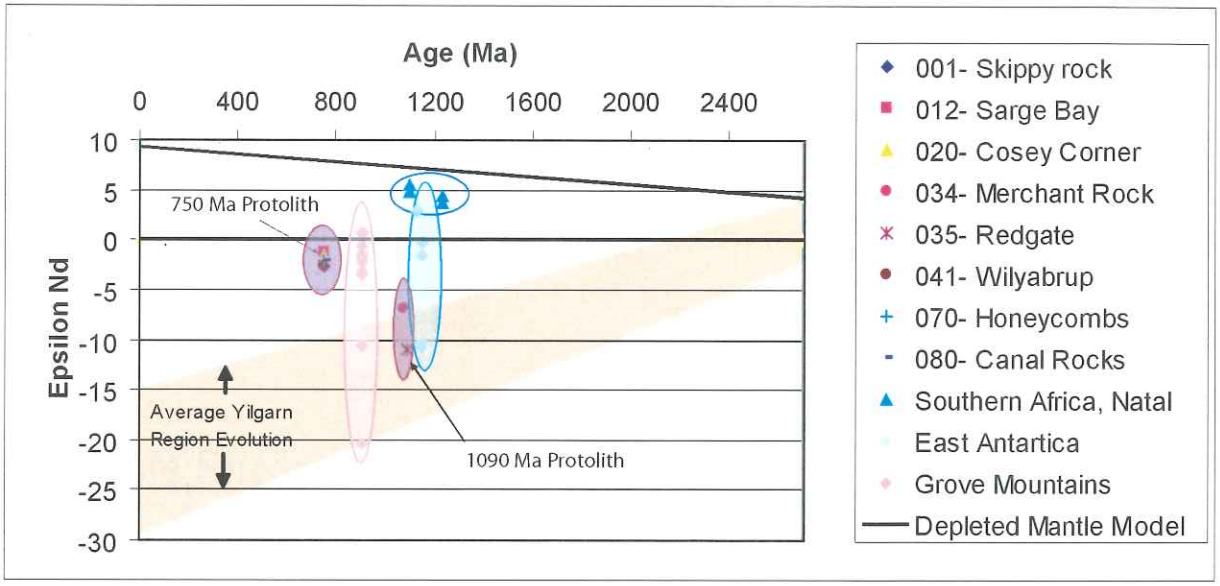

Figure 23. Structural models

a) Pure Shear

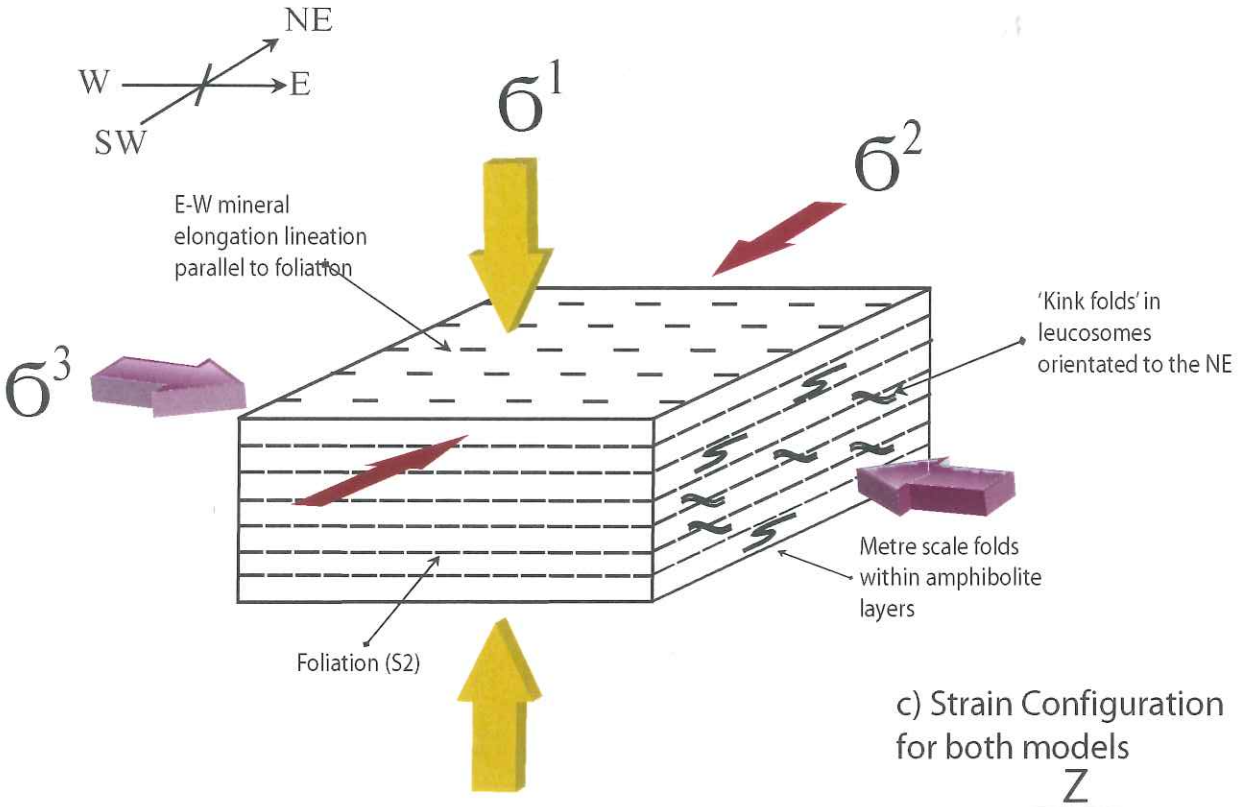

c) Strain Configuration for both models

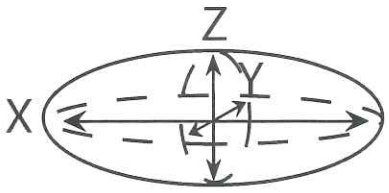

b) Simple Shear

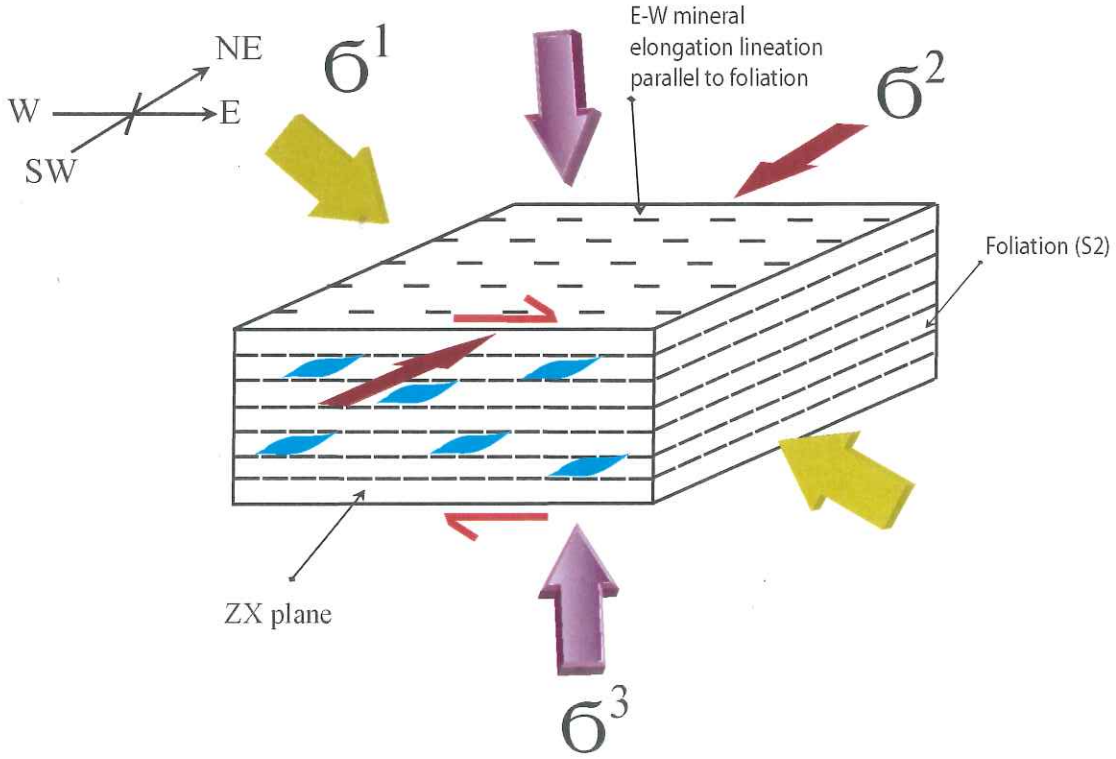

Appendix 1. Microprobe analyses used for *P-T estimates*

Sample	RVLC007							
	Core				Rim			
Mineral	garnet (c)	biotite	plag	sp	garnet (r)	biotite	plag	sp
SiO2	36.61	34.60	59.32	0.06	36.42	35.25	58.79	0.03
TiO2	0.04	3.58	0.04	0.95	0.00	3.83	0.02	0.20
Al2O3	20.66	15.31	25.22	1.84	20.63	14.39	25.15	0.54
Cr2O3	0.01	0.00	0.00	0.00	0.02	0.08	0.05	0.04
FeO	31.88	25.80	0.10	89.55	32.49	25.93	0.40	91.97
MnO	3.78	0.24	0.01	0.13	3.28	0.17	0.00	0.05
MgO	1.31	6.61	0.01	0.05	1.23	6.59	0.03	0.04
CaO	6.30	0.02	7.06	0.03	5.98	0.07	7.54	0.02
Na2O	0.01	0.10	7.50	0.02	0.04	0.09	6.85	0.03
K2O	0.01	9.06	0.16	0.00	0.00	8.89	0.30	0.00
Totals	100.88	95.33	99.45	92.63	100.34	95.31	99.01	92.92
Oxygens	12.00	11.00	8.00	4.00	12.00	11.00	8.00	4.00
Si	2.94	2.73	2.66	0.00	2.94	2.78	2.65	0.00
Ti	0.00	0.21	0.00	0.03	0.00	0.23	0.00	0.01
Al	1.96	1.43	1.33	0.08	1.97	1.34	1.34	0.02
Cr	0.00	0.00	0.00	0.00	0.00	0.01	0.00	0.00
Fe3	0.16	0.00	0.00	1.86	0.16	0.00	0.01	1.96
Fe2	1.98	1.71	0.00	1.02	2.04	1.71	0.00	1.00
Mn	0.26	0.02	0.00	0.00	0.23	0.01	0.00	0.00
Mg	0.16	0.78	0.00	0.00	0.15	0.78	0.00	0.00
Ca	0.54	0.00	0.34	0.00	0.52	0.01	0.36	0.00
Na	0.00	0.02	0.65	0.00	0.01	0.01	0.60	0.00
K	0.00	0.91	0.01	0.00	0.00	0.90	0.02	0.00
Sum	8.00	7.81	5.00	3.00	8.00	7.77	4.98	3.00

Sample	RVLC008									
	Core					Rim				
Mineral	garnet	plag	K Spar	ilhem	cpx	garnet	plag	K-spar	ilhem	cpx
SiO2	37.61	56.3	64.32	0.04	48.36	37.16	55.57	64.32	0.08	48.13
TiO2	0.01	0	0.03	49.66	0.26	0.1	0.02	0.03	49.34	0.29
Al2O3	20.13	27.36	18.08	0	2.03	19.29	27.71	18.08	0	2.1
Cr2O3	0	0	0.01	0.01	0	0	0	0.01	0	0.01
FeO	26.59	0.14	0.05	46.4	21.64	27.72	0.12	0.05	47.15	21.66
MnO	2.13	0	0	1.78	0.43	2.61	0	0	1.79	0.41
MgO	1.02	0	0	0.01	4.95	0.75	0	0	0	4.67
CaO	12.53	10.09	0.06	0.01	21.48	12.58	10.74	0.06	0.02	21.69
Na2O	0	5.85	0.96	0.02	0.33	0.03	5.5	0.96	0.03	0.39
K2O	0	0.15	15.08	0	0	0	0.14	15.08	0.02	0.01
Totals	100.02	99.89	98.59	97.93	99.48	100.24	99.8	98.59	98.43	99.36
Oxygens	12	8	8	3	6	12	8	8	3	6
Si	3	2.53	3	0	1.93	2.97	2.51	3	0	1.92
Ti	0	0	0	0.96	0.01	0.01	0	0	0.95	0.01
Al	1.89	1.45	1	0	0.1	1.82	1.47	1	0	0.1
Cr	0	0	0	0	0	0	0	0	0	0
Fe3	0.11	0.01	0	0.08	0.06	0.23	0.01	0	0.1	0.08
Fe2	1.66	0	0	0.92	0.66	1.62	0	0	0.91	0.65
Mn	0.14	0	0	0.04	0.01	0.18	0	0	0.04	0.01
Mg	0.12	0	0	0	0.29	0.09	0	0	0	0.28
Ca	1.07	0.49	0	0	0.92	1.08	0.52	0	0	0.93
Na	0	0.51	0.09	0	0.03	0.01	0.48	0.09	0	0.03
K	0	0.01	0.9	0	0	0	0.01	0.9	0	0
Sum	8	5	4.99	2	4.01	8	5	4.99	2	4.01

Sample	RVLC009									
	Core					Rim				
Mineral	garnet	hbd	plag	ilhem	cpx	garnet	hbd	cpx	plag	ilhem
SiO2	37.93	39.51	54.85	0.00	49.95	36.82	39.44	49.18	53.21	0.03
TiO2	0.06	2.27	0.02	44.23	0.24	0.04	1.75	0.25	0.00	45.07
Al2O3	20.94	11.65	27.69	0.00	1.74	20.40	11.65	2.15	29.48	0.00
Cr2O3	0.03	0.00	0.00	0.03	0.04	0.00	0.03	0.01	0.01	0.00
FeO	23.66	23.38	0.15	47.53	17.47	25.78	24.41	17.56	0.19	46.95
MnO	1.50	0.51	0.00	1.41	0.69	4.92	0.51	0.67	0.00	1.33
MgO	2.06	5.14	0.00	0.20	8.07	1.46	5.10	7.81	0.00	0.18
CaO	14.02	11.52	10.74	0.05	21.96	9.99	11.29	21.61	12.42	0.01
Na2O	0.03	1.33	5.37	0.00	0.29	0.00	1.06	0.35	4.38	0.05
K2O	0.00	1.76	0.27	0.01	0.01	0.02	1.69	0.01	0.21	0.00
Totals	100.23	97.07	99.09	93.46	100.46	99.43	96.93	99.60	99.90	93.62
Oxygens	12.00	23.00	8.00	3.00	6.00	12.00	23.00	6.00	8.00	3.00
Si	2.98	6.22	2.50	0.00	1.93	2.96	6.19	1.92	2.41	0.00
Ti	0.00	0.27	0.00	0.89	0.01	0.00	0.21	0.01	0.00	0.91
Al	1.94	2.16	1.49	0.00	0.08	1.93	2.16	0.10	1.58	0.00
Cr	0.00	0.00	0.00	0.00	0.00	0.00	0.00	0.00	0.00	0.00
Fe3	0.10	0.24	0.01	0.22	0.07	0.15	0.57	0.08	0.01	0.19
Fe2	1.45	2.84	0.00	0.85	0.50	1.59	2.64	0.49	0.00	0.87
Mn	0.10	0.07	0.00	0.03	0.02	0.34	0.07	0.02	0.00	0.03
Mg	0.24	1.21	0.00	0.01	0.47	0.17	1.19	0.45	0.00	0.01
Ca	1.18	1.94	0.52	0.00	0.91	0.86	1.90	0.90	0.60	0.00
Na	0.00	0.41	0.47	0.00	0.02	0.00	0.32	0.03	0.39	0.00
K	0.00	0.35	0.02	0.00	0.00	0.00	0.34	0.00	0.01	0.00
Sum	8.00	15.70	5.00	2.00	4.00	8.00	15.57	4.00	5.00	2.00

Sample	RVLC018															
	Core								Rim							
Mineral	garnet	biotite	hbd	plag	epidote	ilhem	K-spar	sp	garnet	biotite	hbd	plag	epidote	ilhem	K-spar	sp
SiO2	37.21	35.3	38.4	57.69	30.34	0	64.38	0.03	37.3	35.67	38.23	56.46	30.22	0	64.76	0.03
TiO2	0.08	2.78	1.45	0	29.62	43.3	0	0.19	0.06	3.53	1.73	0	29.05	43.3	0	0.19
Al2O3	20.36	14.05	11.73	27.62	3.76	0	20.52	0.44	20.52	13.46	11.68	27.47	4.19	0	18.3	0.44
Cr2O3	0.03	0	0.06	0.01	0	0.03	0	0.08	0.02	0	0.03	0	0.03	0.03	0	0.08
FeO	25.02	27.65	24.73	0.08	1.36	47.73	0.1	92.3	24.31	27.17	24.38	0.13	1.73	47.73	0.07	92.3
MnO	6.32	0.29	0.78	0.02	0.12	2.26	0.1	0.05	7.99	0.36	0.59	0.07	0.12	2.26	0.03	0.05
MgO	1.22	6.6	4.98	0.03	0	0.07	0	0.01	1	6.83	4.95	0	0	0.07	0.01	0.01
CaO	9.81	0	11.29	8.18	28.87	0	0.12	0.03	9.41	0.06	11	9.92	28.58	0	0.01	0.03
Na2O	0	0.07	1.35	6.99	0.03	0	1.36	0.01	0.03	0.18	1.49	6.24	0	0	1.18	0.01
K2O	0	8.89	1.93	0.18	0.01	0	11.44	0.01	0.02	8.49	1.92	0.08	0	0	12.04	0.01
Totals	100.05	95.63	96.7	100.8	94.11	93.39	98.02	93.15	100.66	95.75	96	100.37	93.92	93.39	96.4	93.15
Oxygens	12	11	23	8	12.5	3	8	4	12	11	23	8	12.5	3	8	4
Si	2.98	2.79	6.07	2.56	2.63	0	2.96	0	2.98	2.82	6.1	2.53	2.63	0	3.03	0
Ti	0.01	0.17	0.17	0	1.93	0.87	0	0.01	0	0.21	0.21	0	1.9	0.87	0	0.01
Al	1.92	1.31	2.19	1.45	0.38	0	1.11	0.02	1.93	1.25	2.2	1.45	0.43	0	1.01	0.02
Cr	0	0	0.01	0	0	0	0	0	0	0	0	0	0	0	0	0
Fe3	0.11	0.06	0.7	0	0	0.25	0	1.97	0.12	0	0.54	0.01	0	0.25	0	1.97
Fe2	1.57	1.77	2.57	0	0.1	0.82	0	1	1.5	1.79	2.72	0	0.13	0.82	0	1
Mn	0.43	0.02	0.11	0	0.01	0.05	0	0	0.54	0.02	0.08	0	0.01	0.05	0	0
Mg	0.15	0.78	1.17	0	0	0	0	0	0.12	0.8	1.18	0	0	0	0	0
Ca	0.84	0	1.91	0.39	2.68	0	0.01	0	0.8	0.01	1.88	0.48	2.66	0	0	0
Na	0	0.01	0.42	0.6	0.01	0	0.12	0	0	0.03	0.46	0.54	0	0	0.11	0
K	0	0.9	0.39	0.01	0	0	0.67		0	0.86	0.39	0.01	0	0	0.72	
Sum	8	7.81	15.71	5.02	7.75	2	4.88	3	7.99	7.79	15.75	5.02	7.76	2	4.88	3

Sample	RVLC027									
	Core					Rim				
Mineral	garnet	hbd	biotite	plag	ilhem	garnet	hbd	biotite	plag	ilhem
SiO2	37.77	41.90	35.75	56.02	0.00	37.85	41.07	35.81	54.24	0.00
TiO2	0.04	1.81	4.91	0.00	49.86	0.06	1.85	4.15	0.01	49.32
Al2O3	20.72	11.19	13.65	27.45	0.00	20.86	11.65	14.02	27.94	0.00
Cr2O3	0.00	0.01	0.01	0.00	0.05	0.07	0.04	0.01	0.00	0.04
FeO	28.10	20.77	22.13	0.18	46.89	28.66	20.47	22.64	0.13	47.48
MnO	3.25	0.37	0.23	0.00	0.45	2.72	0.39	0.21	0.00	0.28
MgO	2.47	7.64	9.35	0.01	0.04	2.92	7.49	9.74	0.00	0.04
CaO	7.48	11.28	0.00	9.87	0.04	7.58	11.00	0.00	11.30	0.00
Na2O	0.02	1.36	0.15	5.86	0.03	0.00	1.46	0.08	5.04	0.00
K2O	0.03	1.36	8.24	0.15	0.00	0.00	1.36	7.96	0.15	0.00
Totals	99.88	97.69	94.42	99.54	97.67	100.72	96.78	94.62	98.81	97.56
Oxygens	12.00	23.00	11.00	8.00	3.00	12.00	23.00	11.00	8.00	3.00
Si	3.01	6.39	2.79	2.53	0.00	2.99	6.32	2.77	2.48	0.00
Ti	0.00	0.21	0.29	0.00	0.97	0.00	0.21	0.24	0.00	0.96
Al	1.95	2.01	1.26	1.46	0.00	1.94	2.11	1.28	1.50	0.00
Cr	0.00	0.00	0.00	0.00	0.00	0.00	0.01	0.00	0.00	0.00
Fe3	0.02	0.33	0.00	0.01	0.06	0.07	0.35	0.09	0.01	0.08
Fe2	1.85	2.32	1.44	0.00	0.96	1.83	2.29	1.38	0.00	0.95
Mn	0.22	0.05	0.02	0.00	0.01	0.18	0.05	0.01	0.00	0.01
Mg	0.29	1.74	1.09	0.00	0.00	0.34	1.72	1.12	0.00	0.00
Ca	0.64	1.84	0.00	0.48	0.00	0.64	1.81	0.00	0.55	0.00
Na	0.00	0.40	0.02	0.51	0.00	0.00	0.44	0.01	0.45	0.00
K	0.00	0.27	0.82	0.01	0.00	0.00	0.27	0.79	0.01	0.00
Sum	8.00	15.56	7.72	5.00	2.00	8.00	15.58	7.70	5.00	2.00

Sample	RVLC045					
	Core			Rim		
Mineral	garnet	biotite	plag	garnet	biotite	plag
SiO2	37.61	35.42	59.95	36.99	35.26	59.78
TiO2	0.00	3.29	0.00	0.01	3.22	0.01
Al2O3	21.27	16.80	25.33	21.14	16.72	24.63
Cr2O3	0.06	0.04	0.00	0.04	0.04	0.00
FeO	30.82	20.32	0.00	34.29	19.91	0.06
MnO	1.69	0.02	0.00	2.60	0.05	0.00
MgO	6.19	10.39	0.00	3.14	10.68	0.00
CaO	2.27	0.00	6.73	1.58	0.10	6.84
Na2O	0.03	0.13	7.94	0.00	0.28	7.86
K2O	0.00	8.70	0.17	0.04	8.83	0.14
Totals	99.94	95.11	100.12	100.33	95.09	99.32
Oxygens	12.00	11.00	8.00	12.00	11.00	8.00
Si	2.97	2.71	2.67	2.98	2.70	2.68
Ti	0.00	0.19	0.00	0.00	0.19	0.00
Al	1.98	1.52	1.33	2.01	1.51	1.30
Cr	0.00	0.00	0.00	0.00	0.00	0.00
Fe3	0.08	0.02	0.00	0.03	0.00	0.00
Fe2	1.93	1.28	0.00	2.28	1.28	0.00
Mn	0.11	0.00	0.00	0.18	0.00	0.00
Mg	0.73	1.18	0.00	0.38	1.22	0.00
Ca	0.19	0.00	0.32	0.14	0.01	0.33
Na	0.00	0.02	0.69	0.00	0.04	0.68
K	0.00	0.85	0.01	0.01	0.86	0.01
Sum	8.00	7.77	5.01	8.00	7.81	5.01

Sample	RVLC051										
	Core						Rim				
Mineral	garnet	hbd	biotite	opx	plag	ilhem	garnet	hbd	plag	opx	ilhem
SiO2	38.71	40.93	36.03	50.16	55.41	0.02	38.33	41.17	53.85	50.29	0.02
TiO2	0.05	2.06	3.30	0.08	0.04	49.53	0.00	2.15	0.02	0.11	49.09
Al2O3	21.41	13.68	16.41	2.60	27.59	0.00	21.57	13.45	28.01	2.38	0.00
Cr2O3	0.03	0.02	0.05	0.01	0.00	0.03	0.00	0.00	0.00	0.00	0.02
FeO	27.42	17.03	16.57	27.47	0.16	47.62	28.12	17.29	0.09	27.35	47.63
MnO	1.68	0.25	0.06	0.51	0.00	0.36	1.55	0.30	0.00	0.57	0.45
MgO	6.90	10.30	14.09	18.62	0.00	0.94	7.10	10.41	0.00	19.21	0.90
CaO	4.38	10.03	0.02	0.41	10.09	0.02	4.24	10.09	11.12	0.40	0.00
Na2O	0.02	2.43	0.57	0.02	5.98	0.00	0.00	2.32	5.06	0.02	0.02
K2O	0.02	0.54	8.39	0.00	0.04	0.00	0.00	0.54	0.04	0.02	0.01
Totals	100.62	97.27	95.49	99.88	99.31	98.52	100.91	97.72	98.19	100.35	98.14
Oxygens	12.00	23.00	11.00	6.00	8.00	3.00	12.00	23.00	8.00	6.00	3.00
Si	3.00	6.10	2.68	1.91	2.51	0.00	2.96	6.10	2.47	1.90	0.00
Ti	0.00	0.23	0.19	0.00	0.00	0.95	0.00	0.24	0.00	0.00	0.94
Al	1.95	2.40	1.44	0.12	1.47	0.00	1.96	2.35	1.52	0.11	0.00
Cr	0.00	0.00	0.00	0.00	0.00	0.00	0.00	0.00	0.00	0.00	0.00
Fe3	0.06	0.59	0.15	0.06	0.01	0.11	0.13	0.66	0.00	0.08	0.12
Fe2	1.72	1.53	0.88	0.82	0.00	0.90	1.69	1.48	0.00	0.78	0.90
Mn	0.11	0.03	0.00	0.02	0.00	0.01	0.10	0.04	0.00	0.02	0.01
Mg	0.80	2.29	1.56	1.06	0.00	0.04	0.82	2.30	0.00	1.08	0.03
Ca	0.36	1.60	0.00	0.02	0.49	0.00	0.35	1.60	0.55	0.02	0.00
Na	0.00	0.70	0.08	0.00	0.53	0.00	0.00	0.67	0.45	0.00	0.00
K	0.00	0.10	0.80	0.00	0.00	0.00	0.00	0.10	0.00	0.00	0.00
Sum	8.00	15.58	7.78	4.00	5.01	2.00	8.00	15.54	4.99	4.00	2.00

Sample	RVLC052											
	Core						Rim					
Mineral	garnet	hbd	biotite	opx	plag	ilhem	garnet	hbd	biotite	opx	plag	ilhem
SiO2	38.54	40.51	35.91	50.55	56.13	0.00	38.31	41.08	36.09	49.99	54.22	0.02
TiO2	0.03	1.98	3.87	0.10	0.03	49.22	0.03	1.84	3.73	0.13	0.00	49.85
Al2O3	21.83	14.42	15.89	2.73	27.59	0.00	21.71	13.69	16.49	2.66	28.93	0.00
Cr2O3	0.03	0.05	0.00	0.03	0.03	0.05	0.00	0.02	0.00	0.02	0.00	0.00
FeO	27.64	17.09	16.57	27.64	0.07	47.56	28.15	17.15	16.91	27.88	0.28	46.23
MnO	1.36	0.20	0.06	0.47	0.03	0.49	1.47	0.22	0.09	0.54	0.04	0.46
MgO	6.44	10.42	12.96	18.68	0.00	0.99	6.58	10.29	13.27	18.60	0.00	1.46
CaO	5.37	10.02	0.03	0.38	9.96	0.00	4.93	10.23	0.01	0.39	11.44	0.00
Na2O	0.03	2.50	0.61	0.00	5.95	0.05	0.01	2.44	0.60	0.00	5.21	0.08
K2O	0.00	0.52	8.00	0.00	0.06	0.03	0.00	0.51	7.82	0.00	0.02	0.01
Totals	101.41	98.33	94.01	100.73	99.87	99.04	101.40	97.99	95.20	100.45	100.17	98.66
Oxygens	12.00	23.00	11.00	6.00	8.00	3.00	12.00	23.00	11.00	6.00	8.00	3.00
Si	2.97	6.00	2.73	1.91	2.53	0.00	2.95	6.11	2.70	1.90	2.45	0.00
Ti	0.00	0.22	0.22	0.00	0.00	0.94	0.00	0.21	0.21	0.00	0.00	0.95
Al	1.98	2.52	1.42	0.12	1.46	0.00	1.97	2.40	1.45	0.12	1.54	0.00
Cr	0.00	0.01	0.00	0.00	0.00	0.00	0.00	0.00	0.00	0.00	0.00	0.00
Fe3	0.09	0.68	0.00	0.04	0.00	0.12	0.12	0.58	0.10	0.07	0.01	0.10
Fe2	1.69	1.43	1.05	0.83	0.00	0.88	1.69	1.55	0.96	0.82	0.00	0.88
Mn	0.09	0.03	0.00	0.02	0.00	0.01	0.10	0.03	0.01	0.02	0.00	0.01
Mg	0.74	2.30	1.47	1.05	0.00	0.04	0.76	2.28	1.48	1.06	0.00	0.06
Ca	0.44	1.59	0.00	0.02	0.48	0.00	0.41	1.63	0.00	0.02	0.55	0.00
Na	0.00	0.72	0.09	0.00	0.52	0.00	0.00	0.70	0.09	0.00	0.46	0.00
K	0.00	0.10	0.78	0.00	0.00	0.00	0.00	0.10	0.75	0.00	0.00	0.00
Sum	8.00	15.59	7.77	4.00	5.00	2.00	8.00	15.59	7.73	4.00	5.01	2.00

Sample	RVLC059									
	Core					Rim				
Mineral	garnet	biotite	plag	K-spar	ilhem	garnet	biotite	plag	K-spar	ilhem
SiO2	36.63	33.92	59.90	65.21	0.01	36.85	33.75	63.41	65.26	0.01
TiO2	0.01	4.53	0.00	0.02	50.30	0.03	4.40	0.00	0.02	50.30
Al2O3	20.66	14.42	25.03	18.61	0.00	20.63	14.79	23.18	18.47	0.00
Cr2O3	0.00	0.00	0.02	0.01	0.04	0.01	0.04	0.00	0.07	0.04
FeO	36.65	28.64	0.03	0.01	46.40	36.48	29.52	0.00	0.00	46.40
MnO	1.68	0.12	0.04	0.00	1.89	1.71	0.06	0.00	0.00	1.89
MgO	0.86	4.49	0.00	0.01	0.01	0.72	4.45	0.00	0.00	0.01
CaO	4.05	0.04	7.36	0.07	0.00	3.85	0.11	4.48	0.09	0.00
Na2O	0.00	0.11	7.46	1.62	0.00	0.05	0.06	8.86	1.00	0.00
K2O	0.00	8.88	0.16	14.68	0.00	0.00	8.54	0.20	15.39	0.00
Totals	100.54	95.15	100.00	100.24	98.65	100.33	95.72	100.13	100.30	98.65
Oxygens	12.00	11.00	8.00	8.00	3.00	12.00	11.00	8.00	8.00	3.00
Si	2.97	2.73	2.67	2.99	0.00	3.00	2.70	2.80	3.00	0.00
Ti	0.00	0.27	0.00	0.00	0.97	0.00	0.27	0.00	0.00	0.97
Al	1.98	1.37	1.32	1.01	0.00	1.98	1.40	1.21	1.00	0.00
Cr	0.00	0.00	0.00	0.00	0.00	0.00	0.00	0.00	0.00	0.00
Fe3	0.09	0.00	0.00	0.00	0.07	0.04	0.00	0.00	0.00	0.07
Fe2	2.40	1.93	0.00	0.00	0.93	2.44	1.98	0.00	0.00	0.93
Mn	0.12	0.01	0.00	0.00	0.04	0.12	0.00	0.00	0.00	0.04
Mg	0.10	0.54	0.00	0.00	0.00	0.09	0.53	0.00	0.00	0.00
Ca	0.35	0.00	0.35	0.00	0.00	0.34	0.01	0.21	0.01	0.00
Na	0.00	0.02	0.65	0.14	0.00	0.01	0.01	0.76	0.09	0.00
K	0.00	0.91	0.01	0.86	0.00	0.00	0.87	0.01	0.90	0.00
Sum	8.00	7.78	5.00	5.01	2.00	8.00	7.77	4.98	5.00	2.00

Sample	RVLC077											
	Core						Rim					
Mineral	garnet	hbd	biotite	plag	sp	ilhem	garnet	hbd	biotite	plag	sp	ilhem
SiO2	37.24	39.89	35.08	59.27	0.07	0.01	37.11	39.71	35.01	58.02	0.13	0.01
TiO2	0.02	1.56	4.48	0.03	0.34	48.89	0.04	1.66	4.27	0.00	0.25	48.89
Al2O3	20.65	11.33	13.02	25.35	1.45	0.00	20.12	10.84	12.86	25.66	0.41	0.00
Cr2O3	0.01	0.02	0.01	0.01	0.02	0.01	0.04	0.02	0.00	0.01	0.03	0.01
FeO	33.40	25.71	25.21	0.09	89.98	46.47	31.17	25.22	25.98	0.18	88.92	46.47
MnO	1.59	0.43	0.16	0.00	0.04	1.02	3.23	0.43	0.15	0.04	0.04	1.02
MgO	2.04	4.76	7.15	0.00	0.05	0.12	1.53	4.73	7.37	0.00	0.00	0.12
CaO	5.92	10.55	0.02	7.56	0.03	0.03	6.85	10.64	0.02	8.35	0.00	0.03
Na2O	0.00	1.74	0.19	7.02	0.08	0.00	0.00	1.67	0.18	6.70	0.00	0.00
K2O	0.02	1.45	9.32	0.24	0.00	0.00	0.02	1.42	8.94	0.20	0.00	0.00
Totals	100.89	97.44	94.64	99.57	92.06	96.55	100.11	96.34	94.78	99.16	89.78	96.55
Oxygens	12.00	23.00	11.00	8.00	4.00	3.00	12.00	23.00	11.00	8.00	4.00	3.00
Si	2.97	6.26	2.80	2.66	0.00	0.00	2.99	6.31	2.79	2.62	0.01	0.00
Ti	0.00	0.18	0.27	0.00	0.01	0.96	0.00	0.20	0.26	0.00	0.01	0.96
Al	1.94	2.09	1.22	1.34	0.07	0.00	1.91	2.03	1.21	1.37	0.02	0.00
Cr	0.00	0.00	0.00	0.00	0.00	0.00	0.00	0.00	0.00	0.00	0.00	0.00
Fe3	0.12	0.50	0.00	0.00	1.91	0.08	0.11	0.42	0.00	0.01	1.95	0.08
Fe2	2.11	2.87	1.68	0.00	1.00	0.93	1.99	2.93	1.73	0.00	1.01	0.93
Mn	0.11	0.06	0.01	0.00	0.00	0.02	0.22	0.06	0.01	0.00	0.00	0.02
Mg	0.24	1.11	0.85	0.00	0.00	0.01	0.18	1.12	0.88	0.00	0.00	0.01
Ca	0.51	1.77	0.00	0.36	0.00	0.00	0.59	1.81	0.00	0.40	0.00	0.00
Na	0.00	0.53	0.03	0.61	0.01	0.00	0.00	0.51	0.03	0.59	0.00	0.00
K	0.00	0.29	0.95	0.01	0.00	0.00	0.00	0.29	0.91	0.01	0.00	0.00
Sum	8.00	15.67	7.81	4.99	3.00	2.00	8.00	15.67	7.82	4.99	3.00	2.00

Sample	RVLC080											
	Core						Rim					
Mineral	garnet	biotite	plag	K-spar	sp	ilhem	garnet	biotite	plag	K-spar	sp	ilhem
SiO2	36.96	37.23	62.38	65.54	0.05	0.00	36.43	35.95	62.12	65.51	0.05	0.00
TiO2	0.01	3.97	0.02	0.02	0.18	44.82	0.04	3.59	0.00	0.00	0.18	44.82
Al2O3	20.24	15.16	23.77	18.69	0.08	0.00	20.41	14.99	23.38	18.61	0.08	0.00
Cr2O3	0.00	0.04	0.04	0.00	0.00	0.00	0.01	0.00	0.04	0.02	0.00	0.00
FeO	36.11	15.60	0.01	0.03	92.08	43.34	36.16	18.19	0.18	0.00	92.08	43.34
MnO	1.64	0.10	0.00	0.04	0.00	2.19	1.78	0.12	0.00	0.00	0.00	2.19
MgO	1.28	14.07	0.00	0.00	0.03	0.03	1.37	12.36	0.02	0.01	0.03	0.03
CaO	4.02	0.01	5.03	0.15	0.00	0.01	2.93	0.05	4.22	0.06	0.00	0.01
Na2O	0.07	0.14	8.87	4.05	0.03	0.08	0.06	0.09	9.46	1.47	0.03	0.08
K2O	0.04	8.87	0.29	9.49	0.03	0.04	0.00	9.17	0.15	12.09	0.03	0.04
Totals	100.37	95.19	100.41	98.01	92.48	90.51	99.19	94.51	99.57	97.77	92.48	90.51
Oxygens	12.00	11.00	8.00	8.00	4.00	3.00	12.00	11.00	8.00	8.00	4.00	3.00
Si	2.99	2.78	2.76	3.01	0.00	0.00	2.99	2.75	2.77	3.03	0.00	0.00
Ti	0.00	0.22	0.00	0.00	0.01	0.94	0.00	0.21	0.00	0.00	0.01	0.94
Al	1.93	1.34	1.24	1.01	0.00	0.00	1.97	1.35	1.23	1.01	0.00	0.00
Cr	0.00	0.00	0.00	0.00	0.00	0.00	0.00	0.00	0.00	0.00	0.00	0.00
Fe3	0.10	0.00	0.00	0.00	1.99	0.14	0.06	0.01	0.01	0.00	1.99	0.14
Fe2	2.35	0.98	0.00	0.00	1.00	0.87	2.42	1.16	0.00	0.00	1.00	0.87
Mn	0.11	0.01	0.00	0.00	0.00	0.05	0.12	0.01	0.00	0.00	0.00	0.05
Mg	0.16	1.57	0.00	0.00	0.00	0.00	0.17	1.41	0.00	0.00	0.00	0.00
Ca	0.35	0.00	0.24	0.01	0.00	0.00	0.26	0.00	0.20	0.00	0.00	0.00
Na	0.01	0.02	0.76	0.36	0.00	0.01	0.01	0.01	0.82	0.13	0.00	0.01
K	0.00	0.85	0.02	0.56	0.00	0.00	0.00	0.90	0.01	0.71	0.00	0.00
Sum	8.00	7.76	5.01	4.95	3.00	2.00	8.00	7.81	5.03	4.89	3.00	2.00

Sample **RVLC084**

	Core					Rim				
Mineral	garnet	biotite	plag	ilhem	sp	garnet	biotite	plag	ilhem	sp
SiO2	37.31	36.59	61.31	0	0.1	37.59	37.23	61.31	0	0.1
TiO2	0	3.49	0	44.38	2.3	0.02	3.97	0	44.38	2.3
Al2O3	21.05	14.92	23.47	0	8.4	21.29	15.16	23.47	0	8.4
Cr2O3	0.03	0.04	0.02	0.04	0	0.01	0.04	0.02	0.04	0
FeO	28.708	17.997	0.087	46.534	80.68	29.414	15.602	0.087	46.534	80.68
MnO	6.21	0.26	0	3.57	0.42	6.34	0.1	0	3.57	0.42
MgO	5.04	12.35	0.01	0.09	0.31	4.65	14.07	0.01	0.09	0.31
CaO	1.52	0	5.73	0	0.01	1.61	0.01	5.73	0	0.01
Na2O	0.01	0.1	8.06	0	0	0	0.14	8.06	0	0
K2O	0	8.85	0.56	0	0.02	0.01	8.87	0.56	0	0.02
Totals	99.878	94.597	99.247	94.614	92.24	100.93	95.192	99.247	94.614	92.24
Oxyge	12	11	8	3	4	12	11	8	3	4
Si	2.968	2.789	2.746	0	0.004	2.967	2.782	2.746	0	0.004
Ti	0	0.2	0	0.884	0.065	0.001	0.223	0	0.884	0.065
Al	1.974	1.341	1.239	0	0.371	1.981	1.335	1.239	0	0.371
Cr	0.002	0.002	0.001	0.001	0	0.001	0.002	0.001	0.001	0
Fe3	0.09	0.003	0.003	0.231	1.493	0.082	0	0.003	0.231	1.493
Fe2	1.82	1.144	0	0.8	1.035	1.86	0.975	0	0.8	1.035
Mn	0.418	0.017	0	0.08	0.013	0.424	0.006	0	0.08	0.013
Mg	0.597	1.403	0	0.004	0.017	0.547	1.567	0	0.004	0.017
Ca	0.129	0	0.275	0	0	0.136	0.001	0.275	0	0
Na	0.001	0.014	0.7	0	0	0	0.02	0.7	0	0
K	0	0.862	0.032	0	0.001	0.001	0.847	0.032	0	0.001
Sum	8	7.776	4.998	2	2.999	8	7.759	4.998	2	2.999

Sample	RVLC092									
	Core					Rim				
Mineral	garnet	hbd	plag	sp	ilhem	garnet	hbd	plag	sp	ilhem
SiO2	36.53	37.87	60.09	0.09	0.08	36.64	37.49	59.86	0.09	0.08
TiO2	0.02	1.17	0.02	1.99	50.4	0.02	1.13	0	0.57	50.4
Al2O3	20.34	11.45	24.47	0.9	0	20.26	11.39	24.46	0.63	0
Cr2O3	0.04	0	0.01	0	0.06	0	0	0	0.01	0.06
FeO	31.9372	29.3153	0.0733	90.1063	44.6268	32.4756	29.1292	0.1178	91.6746	44.6268
MnO	3.73	0.49	0.02	0.07	1.79	3.7	0.5	0	0.06	1.79
MgO	1.29	3.11	0	0.02	0.01	1.32	3.13	0	0	0.01
CaO	6.29	10.13	6.53	0	0.02	6.23	10.18	6.81	0	0.02
Na2O	0.01	1.71	7.93	0	0	0.03	1.59	7.73	0	0
K2O	0	1.8	0.28	0	0	0.01	1.73	0.29	0.02	0
Totals	100.1872	97.0453	99.44	99.55	97.11	101.02	96.2692	99.28	99.75	97.11
Oxygens	12	23	8	4	3	12	23	8	4	3
Si	2.948	6.059	2.694	0.004	0.002	2.944	6.039	2.689	0.003	0.002
Ti	0.001	0.14	0.001	0.058	0.986	0.001	0.137	0	0.017	0.986
Al	1.936	2.16	1.293	0.041	0	1.919	2.162	1.295	0.029	0
Cr	0.003	0	0	0	0.001	0	0	0	0	0.001
Fe3	0.163	0.883	0.003	1.837	0.023	0.197	0.956	0.004	1.932	0.023
Fe2	1.993	3.04	0	1.057	0.947	1.985	2.968	0	1.016	0.947
Mn	0.255	0.067	0.001	0.002	0.04	0.252	0.068	0	0.002	0.04
Mg	0.155	0.742	0	0.001	0	0.158	0.751	0	0	0
Ca	0.544	1.737	0.314	0	0.001	0.536	1.757	0.328	0	0.001
Na	0.001	0.531	0.689	0	0	0.005	0.498	0.674	0	0
K	0	0.368	0.016	0	0	0.002	0.356	0.017	0.001	0
Sum	8	15.728	5.011	3	2	7.999	15.692	5.007	3	2

Appendix 2: THERMOCALC output file for average-P, average-T and average P-T calculations

THERMOCALC 3.21 running at
17.50 on Thu 23 Oct,2008 with thermodynamic dataset
produced at

an independent set of reactions has been calculated

Activities and their uncertainties

	py	gr	alm	spss	andr	an	ab
a	0.000267	0.0350	0.170	0.000107	0.00962	0.640	0.520
sd(a)/a	0.78782	0.40751	0.17905	0.81657	0.55789	0.05031	0.06912

	ilm	hem	pnt	di	hed	cats	tr
a	0.880	0.00150	0.0370	0.290	0.600	0.0260	0.000176
sd(a)/a	0.10000	6.66667	0.39138	0.15123	0.10000	0.42308	56.72150

	fact	ts	parg	sph	q	H2O
a	0.00720	8.00e-6	0.000435	1.00	1.00	0.500
sd(a)/a	0.59008	7.07107	0.95893	0	0	

Independent set of reactions
1) cats + q = an
2) 3di + 3cats = py + 2gr
3) 3hed + 3cats = 2gr + alm
4) 12di + 3ts = 2py + 4gr + 3tr
5) 3gr + 2ts + 5q = 7an + 6di + 2H2O
6) 3cats + 4fact = 3alm + 11hed + 4q + 4H2O
7) gr + 2alm + 3sph = 3an + 3ilm + 3hed
8) spss + 3cats + 3sph = gr + 3an + 3pnt
9) 3alm + 2andr + 3sph = 3an + 3ilm + 2hem + 6hed
10) 12an + 18di + 3parg = 5py + 10gr + 3ab + 3tr

Calculations for the independent set of reactions
at T = 750°C (for a(H2O) = 0.5)

	P(T)	sd(P)	a	sd(a)	b	c	ln_K	sd(ln_K)
1	6.2	2.68	-17.46	0.23	-0.01779	1.355	3.203	0.426
2	10.7	5.74	-52.26	0.91	0.08066	-2.617	-0.270	1.761
3	10.6	4.49	-106.07	2.13	0.10132	-2.972	4.005	1.548
4	15.6	258.49	-29.81	6.88	0.16244	-5.643	-5.733	171.506
5	3.9	10.85	161.50	4.42	-0.38802	11.156	22.978	14.228
6	13.0	4.56	40.54	3.38	-0.13294	-5.548	19.749	2.946
7	8.6	0.82	35.20	2.32	-0.13012	7.828	3.641	0.705
8	3.6	3.65	-62.87	6.22	-0.00127	4.879	5.510	1.961
9	15.8	12.60	31.14	4.33	-0.14374	9.057	-3.188	13.408
10	8.1	52.54	-10.89	5.40	0.65966	-27.573	-51.699	170.306

Average pressures (for a(H2O) = 0.5)

Single end-member diagnostic information

av, sd, fit are result of doubling the uncertainty on ln a :
a ln a suspect if any are v different from lsq values.
e* are ln a residuals normalised to ln a uncertainties :
Large absolute values, say >2.5, point to suspect info.
Hat are the diagonal elements of the hat matrix :
Large values, say >0.50, point to influential data.
For 95% confidence, fit (= sd(fit)) < 1.37;
However a larger value may be OK - look at the diagnostics!

	av	sd	fit
lsq	8.40	0.70	0.81

	P	sd	fit	e*	hat	a(obs)	a(calc)
py	8.37	0.71	0.80	-0.3	0.02	0.000267	0.000203
gr	8.51	0.76	0.80	0.4	0.17	0.0350	0.0410
alm	7.97	0.88	0.77	-0.5	0.26	0.170	0.154
spss	8.45	0.70	0.77	0.6	0.01	0.000107	0.000176
andr	8.40	0.70	0.81	-0.0	0.00	0.00962	0.00937
an	8.44	0.76	0.81	-0.1	0.06	0.640	0.637
ab	8.40	0.70	0.81	-0.1	0.00	0.520	0.517
ilm	8.18	0.80	0.79	0.5	0.18	0.880	0.922
hem	8.40	0.70	0.79	0.6	0.00	0.00150	0.0597
pnt	8.47	0.70	0.75	-0.9	0.01	0.0370	0.0262
di	8.48	0.71	0.77	-0.6	0.02	0.290	0.264

hed	8.43	0.72	0.81	-0.2	0.03	0.600	0.591
cats	8.50	0.72	0.77	0.8	0.05	0.0260	0.0367
tr	8.40	0.70	0.81	0.0	0.00	0.000176	0.000414
fact	8.26	0.73	0.78	0.7	0.09	0.00720	0.0109
ts	8.40	0.70	0.80	0.4	0.00	8.00e-6	0.000134
parg	8.47	0.70	0.70	1.3	0.01	0.000435	0.00147
sph	8.40	0.70	0.81	0	0	1.00	1.00
q	8.40	0.70	0.81	0	0	1.00	1.00
H2O	8.40	0.70	0.81	0	0	1.00	1.00

C	600	625	650	675	700	725	750	775	800	825	850	875	900
P	6.8	7.1	7.4	7.7	7.9	8.2	8.4	8.6	8.9	9.1	9.4	9.6	9.8
	0.86	0.78	0.72	0.67	0.67	0.68	0.70	0.72	0.73	0.75	0.77	0.78	0.80
gfit	1.4	1.3	1.1	1.0	0.9	0.9	0.8	0.8	0.8	0.7	0.7	0.8	0.8

****

****

independent set of reactions has been calculated

tivities and their uncertainties

	py	gr	alm	spss	andr	an	ab
	0.000267	0.0350	0.170	0.000107	0.00962	0.640	0.520
(a)/a	0.78782	0.40751	0.17905	0.81657	0.55789	0.05031	0.06912

	ilm	hem	pnt	di	hed	cats	tr
	0.880	0.00150	0.0370	0.290	0.600	0.0260	0.000176
(a)/a	0.10000	6.66667	0.39138	0.15123	0.10000	0.42308	56.72150

	fact	ts	parg	sph	q
	0.00720	8.00e-6	0.000435	1.00	1.00
(a)/a	0.59008	7.07107	0.95893	0	0

dependent set of reactions
cats + q = an
3di + 3cats = py + 2gr
3hed + 3cats = 2gr + alm
12di + 3ts = 2py + 4gr + 3tr
gr + 2alm + 3sph = 3an + 3ilm + 3hed
spss + 3cats + 3sph = gr + 3an + 3pnt
12an + 18di + 3parg = 5py + 10gr + 3ab + 3tr
5alm + 12an + 18di + 3parg = 10py + 10gr + 3ab + 3fact
2andr + 12an + 15hed + 3parg = 4py + 11gr + 3ab + 2hem + 3fact

lculations for the independent set of reactions
t T = 750°C

P(T)	sd(P)	a	sd(a)	b	c	ln_K	sd(ln_K)
6.2	2.68	-17.46	0.23	-0.01779	1.355	3.203	0.426
10.7	5.74	-52.26	0.91	0.08066	-2.617	-0.270	1.761
10.6	4.49	-106.07	2.13	0.10132	-2.972	4.005	1.548
15.6	258.49	-29.81	6.88	0.16244	-5.643	-5.733	171.506
8.6	0.82	35.20	2.32	-0.13012	7.828	3.641	0.705
3.6	3.65	-62.87	6.22	-0.00127	4.879	5.510	1.961
8.1	52.54	-10.89	5.40	0.65966	-27.573	-51.699	170.306
8.6	3.34	339.94	7.53	0.48765	-25.407	-72.852	9.935
6.3	4.84	13.06	7.45	0.59798	-26.310	-54.031	14.937

erage pressures

ngle end-member diagnostic information

, sd, fit are result of doubling the uncertainty on ln a :
ln a suspect if any are v different from lsq values.
are ln a residuals normalised to ln a uncertainties :
rge absolute values, say >2.5, point to suspect info.
t are the diagonal elements of the hat matrix :
rge values, say >0.47, point to influential data.
r 95% confidence, fit (= sd(fit)) < 1.39;
wever a larger value may be OK - look at the diagnostics!

	av	sd	fit
lsq	8.21	0.73	0.66

	P	sd	fit	e*	hat	a(obs)	a(calc)
py	8.19	0.74	0.66	-0.2	0.02	0.000267	0.000225
gr	8.31	0.79	0.65	0.3	0.17	0.0350	0.0402
alm	7.89	0.90	0.63	-0.4	0.23	0.170	0.158
spss	8.26	0.73	0.60	0.6	0.01	0.000107	0.000175
andr	8.21	0.73	0.66	-0.0	0.00	0.00962	0.00937
an	8.24	0.79	0.66	-0.1	0.06	0.640	0.638
ab	8.21	0.73	0.66	-0.0	0.00	0.520	0.519
ilm	7.85	0.85	0.60	0.6	0.21	0.880	0.939
hem	8.20	0.73	0.64	0.6	0.00	0.00150	0.0606
pnt	8.28	0.73	0.58	-0.9	0.01	0.0370	0.0264
di	8.24	0.75	0.66	-0.2	0.03	0.290	0.282
hed	8.11	0.77	0.65	0.3	0.07	0.600	0.617
cats	8.31	0.75	0.62	0.7	0.06	0.0260	0.0356
tr	8.21	0.73	0.66	0.0	0.00	0.000176	0.000209
fact	8.25	0.74	0.65	-0.3	0.01	0.00720	0.00602
ts	8.21	0.73	0.66	0.3	0.00	8.00e-6	5.55e-5
parg	8.27	0.74	0.64	0.5	0.03	0.000435	0.000672
sph	8.21	0.73	0.66	0	0	1.00	1.00
q	8.21	0.73	0.66	0	0	1.00	1.00

T°C	600	625	650	675	700	725	750	775	800	825	850	875	900
av P	6.6	6.9	7.2	7.4	7.7	7.9	8.2	8.5	8.7	9.0	9.2	9.5	9.8
sd	0.63	0.65	0.67	0.68	0.70	0.71	0.73	0.75	0.76	0.78	0.79	0.81	0.83
sigfit	0.9	0.9	0.8	0.7	0.7	0.7	0.7	0.7	0.7	0.7	0.7	0.8	0.8

****

an independent set of reactions has been calculated

Activities and their uncertainties

	py	gr	alm	spss	andr	an	ab
a	0.000267	0.0350	0.170	0.000107	0.00962	0.640	0.520
sd(a)/a	0.78782	0.40751	0.17905	0.81657	0.55789	0.05031	0.06912

	ilm	hem	pnt	di	hed	cats	tr
a	0.880	0.00150	0.0370	0.290	0.600	0.0260	0.000176
sd(a)/a	0.10000	6.66667	0.39138	0.15123	0.10000	0.42308	56.72150

	fact	ts	parg	sph	q	H2O
a	0.00720	8.00e-6	0.000435	1.00	1.00	0.500
sd(a)/a	0.59008	7.07107	0.95893	0	0	

Independent set of reactions
1) 3di + 3cats = py + 2gr
2) 3hed + 3cats = 2gr + alm
3) 12di + 3ts = 2py + 4gr + 3tr
4) gr + 2tr = py + 7di + 2q + 2H2O
5) 2gr + alm + 3q = 3an + 3hed
6) gr + 2alm + 3sph = 3an + 3ilm + 3hed
7) 27cats + 6fact = 11gr + 10alm + 6an + 6H2O
8) andr + tr = hem + 5di + q + H2O
9) 6pnt + 21cats + 6fact = 9gr + 10alm + 2spss + 6sph + 6H2O
10) 12an + 18di + 3parg = 5py + 10gr + 3ab + 3tr

Calculations for the independent set of reactions
at P = 7.5 kbar (for a(H2O) = 0.5)

	T(P)	sd(T)	a	sd(a)	b	c	ln_K	sd(ln_K)
1	643	156	-49.68	0.91	0.07760	-2.591	-0.270	1.761
2	680	110	-103.30	2.13	0.09800	-2.940	4.005	1.548
3	336	7455	-26.31	6.88	0.15743	-5.518	-5.733	171.506
4	875	4188	184.43	0.90	-0.18538	-0.800	3.746	113.451
5	712	42	53.93	2.11	-0.15560	7.105	5.605	0.899
6	667	41	34.28	2.32	-0.12942	7.858	3.641	0.705
7	620	405	-598.71	11.46	0.21954	-16.477	70.869	12.900
8	467	4738	57.41	0.75	-0.08249	0.013	0.596	57.120
9	656	346	-468.33	16.71	0.21851	-26.382	59.849	10.785
10	674	1763	-10.84	5.40	0.66100	-27.748	-51.699	170.306

Average temperatures (for a(H2O) = 0.5)

ngle end-member diagnostic information

, sd, fit are result of doubling the uncertainty on ln a :
ln a suspect if any are v different from lsq values.
are ln a residuals normalised to ln a uncertainties :
rge absolute values, say >2.5, point to suspect info.
t are the diagonal elements of the hat matrix :
rge values, say >0.50, point to influential data.
r 95% confidence, fit (= sd(fit)) < 1.37;
wever a larger value may be OK - look at the diagnostics!

	av	sd	fit
q	717	48	1.03

	T	sd	fit	e*	hat	a(obs)	a(calc)
py	709	48	1.00	-0.8	0.05	0.000267	0.000147
gr	711	56	1.03	0.2	0.30	0.0350	0.0383
alm	753	48	0.91	-1.1	0.14	0.170	0.140
spss	716	47	1.00	0.6	0.00	0.000107	0.000174
andr	717	48	1.03	-0.1	0.00	0.00962	0.00933
an	720	50	1.03	0.1	0.03	0.640	0.645
ab	717	48	1.03	-0.1	0.00	0.520	0.516
ilm	735	47	0.96	1.0	0.07	0.880	0.972
hem	718	48	1.02	0.6	0.00	0.00150	0.112
pnt	715	46	0.98	-0.9	0.00	0.0370	0.0264
di	714	48	1.01	-0.5	0.01	0.290	0.267
hed	713	53	1.03	-0.1	0.10	0.600	0.591
cats	720	48	1.02	0.5	0.03	0.0260	0.0324
tr	717	48	1.03	0.0	0.00	0.000176	0.000605
fact	720	45	0.96	1.2	0.00	0.00720	0.0144
ts	716	48	1.02	0.4	0.00	8.00e-6	0.000189
parg	691	45	0.90	1.5	0.13	0.000435	0.00184
sph	717	48	1.03	0	0	1.00	1.00
q	717	48	1.03	0	0	1.00	1.00
H2O	717	48	1.03	0	0	1.00	1.00

	5.0	5.5	6.0	6.5	7.0	7.5	8.0	8.5	9.0	9.5	10.0
T	581	607	634	662	689	717	746	773	801	830	859
	80	73	66	59	53	48	47	47	47	47	48
gfit	1.7	1.6	1.4	1.3	1.1	1.0	1.0	0.9	0.9	0.9	1.0

****

, sd, fit are result of doubling the uncertainty on ln a :
ln a suspect if any are v different from lsq values.
are ln a residuals normalised to ln a uncertainties :
rge absolute values, say >2.5, point to suspect info.
t are the diagonal elements of the hat matrix :
rge values, say >0.47, point to influential data.
r 95% confidence, fit (= sd(fit)) < 1.39;
wever a larger value may be OK - look at the diagnostics!

	av	sd	fit
q	699	48	0.80

	T	sd	fit	e*	hat	a(obs)	a(calc)
py	692	49	0.76	-0.7	0.05	0.000267	0.000159
gr	682	56	0.77	0.5	0.32	0.0350	0.0434
alm	721	56	0.75	-0.5	0.17	0.170	0.154
spss	698	48	0.75	0.6	0.00	0.000107	0.000176
andr	699	48	0.80	-0.1	0.00	0.00962	0.00936
an	699	50	0.80	0.0	0.03	0.640	0.640
ab	699	48	0.80	-0.0	0.00	0.520	0.518
ilm	716	50	0.69	1.0	0.07	0.880	0.969
hem	699	48	0.78	0.6	0.00	0.00150	0.0807
pnt	698	48	0.72	-0.9	0.00	0.0370	0.0263
di	699	48	0.80	-0.1	0.00	0.290	0.287
hed	707	51	0.78	0.3	0.08	0.600	0.619
cats	702	48	0.79	0.4	0.03	0.0260	0.0313
tr	699	48	0.80	0.0	0.00	0.000176	0.000282
fact	692	49	0.77	-0.4	0.03	0.00720	0.00557
ts	699	48	0.79	0.3	0.00	8.00e-6	7.43e-5
parg	688	50	0.75	0.7	0.08	0.000435	0.000823

sph	699	48	0.80	0	0	1.00	1.00
q	699	48	0.80	0	0	1.00	1.00

	5.0	5.5	6.0	6.5	7.0	7.5	8.0	8.5	9.0	9.5	10.0
v T	544	575	606	637	668	699	730	760	791	823	855
d	62	56	50	48	48	48	48	48	48	48	50
igfit	1.3	1.2	1.0	0.9	0.9	0.8	0.8	0.8	0.9	0.9	1.1

****

Appendix 3(i) Backscatter images of selected monazite grains. All ages are quoted as $^{206}Pb/^{238}U$ ages with 1□ error. Spot size is 15μm

a) RVLC003 - Skippy Rock

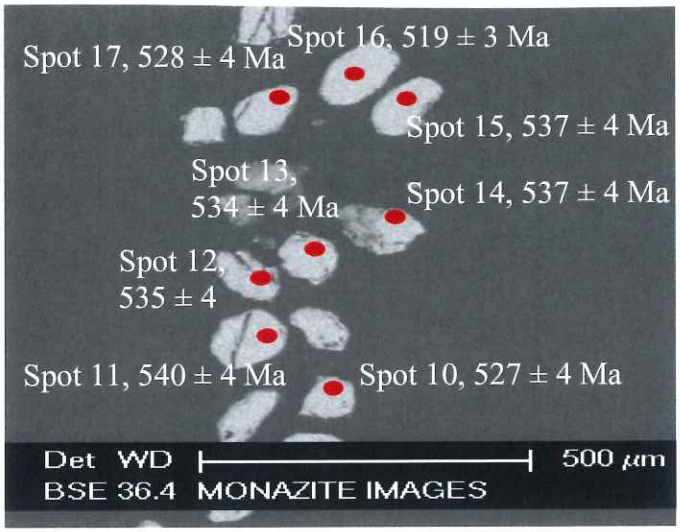

b) RVLC020 - Cosy Corner

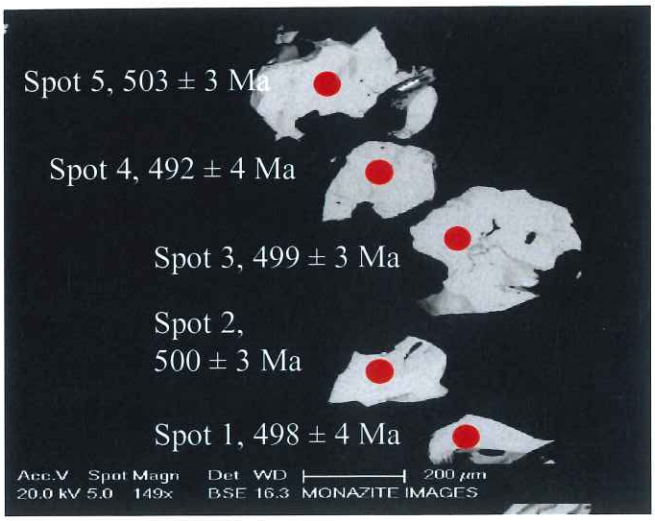

c) RVLC025 - Round Rocks

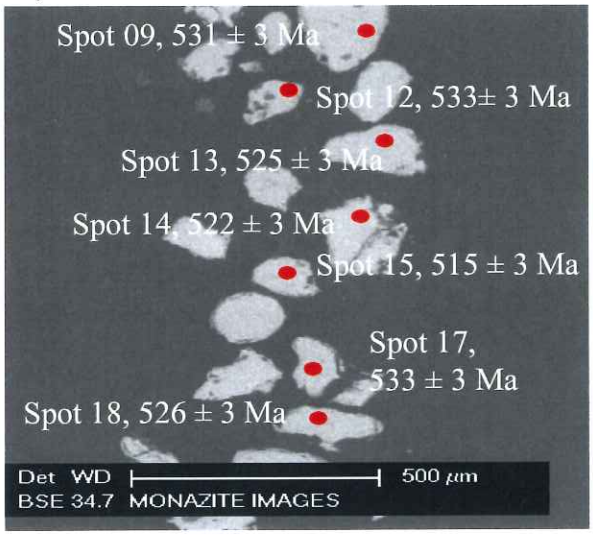

d) RVLC046 - Willyabrup Cliffs

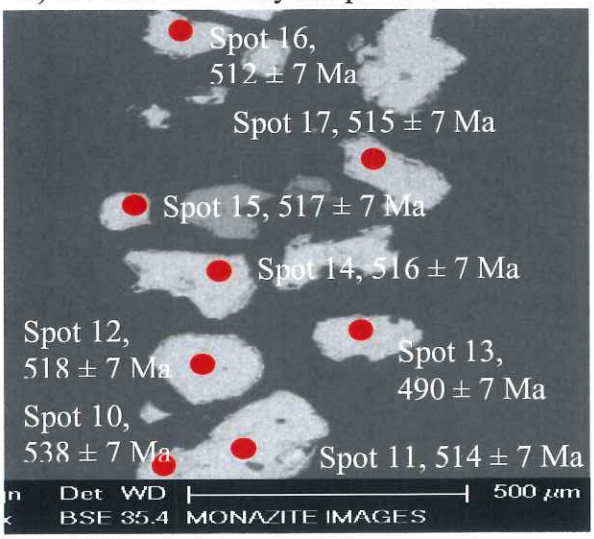

g) RVLC070 - Honeycombs

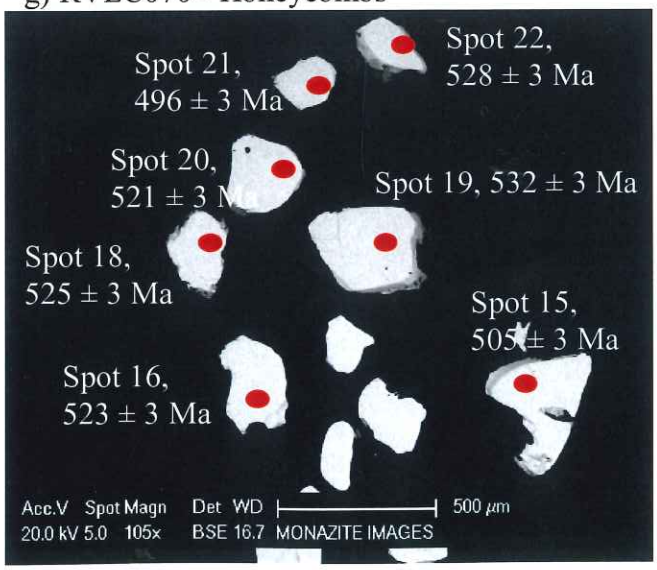

f) RVLC083 - Honeycombs

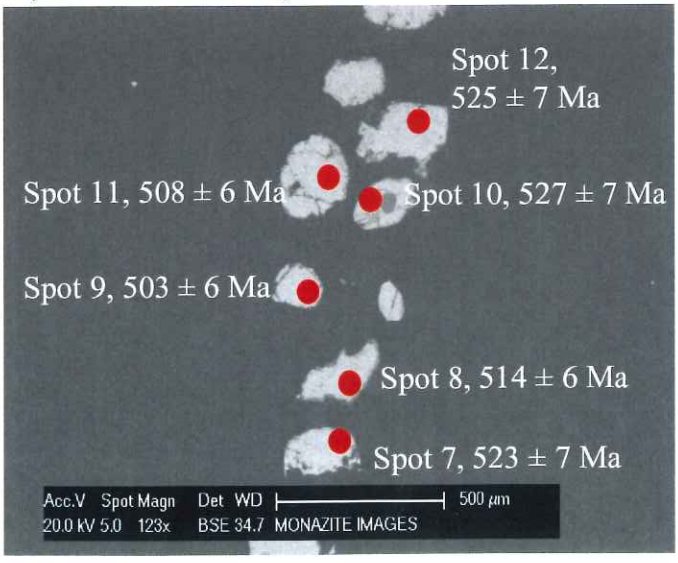

Appendix 3(ii). Cathodoluminescence images of selected zircon grains. All ages are quoted as $^{206}Pb/^{238}U$ ages with 1□ error. Spot size is 30μm

a) RVLC034 – Merchant Rocks

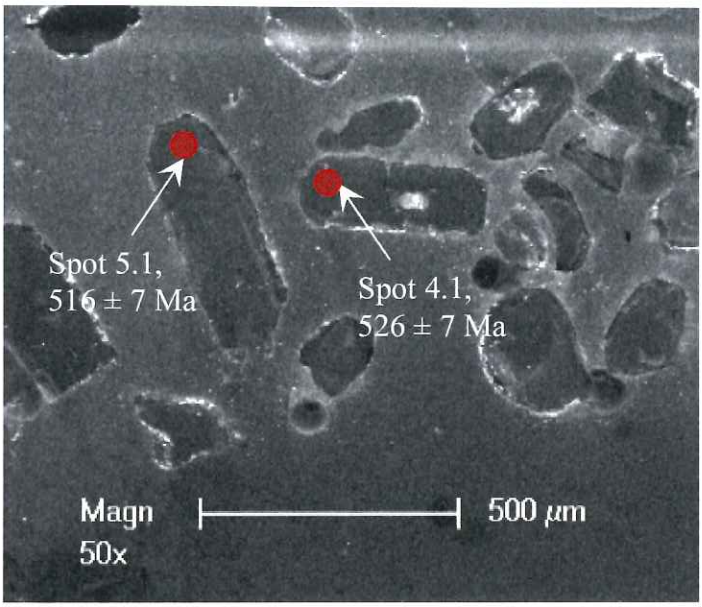

b) RVLC035 - Redgate Beach

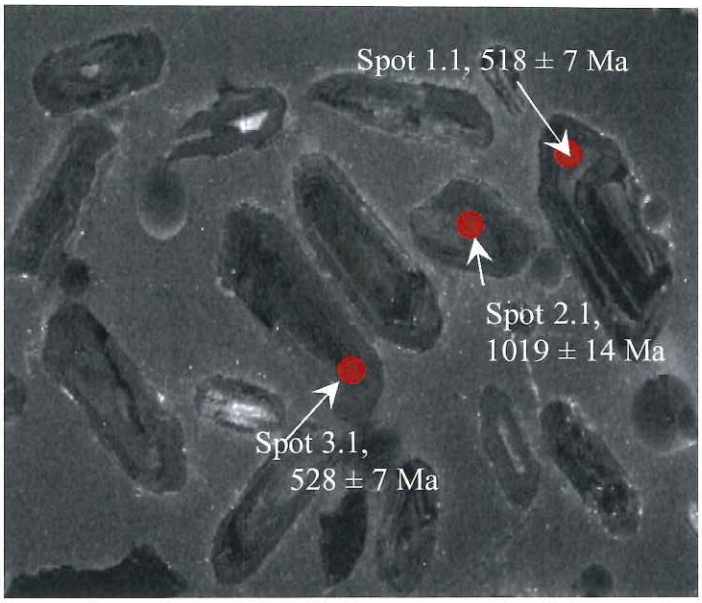

c) RVLC041 - Willyabrup Cliffs